FUNCTIONAL ELEMENTS IN THREE-DIMENSIONAL PHOTONIC BANDGAP MATERIALS

Zur Erlangung des akademischen Grades eines
DOKTORS DER NATURWISSENSCHAFTEN
der Fakultät für Physik des
Karlsruher Instituts für Technologie

genehmigte

DISSERTATION

von

Diplom-Physikerin Diplom-Kauffrau
Isabelle Philippa Staude
aus Frankfurt/Main

Tag der mündlichen Prüfung:	11. Februar 2011
Referent:	Prof. Dr. Martin Wegener
Korreferent:	Prof. Dr. Kurt Busch

Publications

Parts of this thesis have already been published.

In scientific journals:

- I. Staude, G. von Freymann, S. Essig, K. Busch, and M. Wegener, "*Waveguides in three-dimensional photonic-band-gap materials by direct laser writing and silicon double inversion*," Opt. Lett., **36**, 67, (2011).

- I. Staude, M. Thiel, S. Essig, C. Wolff, K. Busch, G. von Freymann, and M. Wegener, "*Fabrication and characterization of silicon woodpile photonic crystals with a complete bandgap at telecom wavelengths*," Opt. Lett. **35**, 1094, (2010).

- G. von Freymann, A. Ledermann, M. Thiel, I. Staude, S. Essig, K. Busch, and M. Wegener, "*Three-Dimensional Nanostructures for Photonics*," Adv. Funct. Mater. **20**, 1038, (2010).

At conferences and seminars (only own presentations):

- I. Staude, S. Essig, K. Busch, G. von Freymann, and M. Wegener, "*Silicon Woodpile Photonic Crystals with Designed Defects*," contributed talk, International Symposium on Photonic and Electromagnetic Crystal Structures (PECS-IX), Granada, Spain, September 2010.

- I. Staude, M. Thiel, S. Essig, C. Wolff, K. Busch, G. von Freymann, and M. Wegener, "*Woodpile Photonic Crystals with a Complete Bandgap Reaching Telecom Wavelengths*," contributed talk, Conference on Lasers and Electro-Optics (CLEO), San Jose, USA, May 2010.

- I. Staude, M. Hermatschweiler, G. von Freymann, and M. Wegener, "*Feature size reduction of silicon inverted direct laser written photonic crystal structures*," contributed talk, DPG-Frühjahrstagung, Dresden, Germany, March 2009.

- I. Staude, M. Thiel, M. Hermatschweiler, G. von Freymann, and M. Wegener "*3D Cavities in Silicon Woodpile Photonic Crystals*," poster, CFN Summerschool on Nano-Photonics, Bad Herrenalb, Germany, August 2008.

- I. Staude, M. Thiel, M. Hermatschweiler, G. von Freymann, and M. Wegener, "*Defect Structures in Woodpile Photonic Crystals fabricated via Direct Laser Writing and Silicon Inversion*," poster, WE-Hereaus-Seminar: Periodic Nanostructures for Photonics, Bad Honnef, Germany, February 2008.

Additional work on related topics has been published.

In scientific journals:

- M. S. Rill, C. Plet, M. Thiel, I. Staude, G. von Freymann, S. Linden, and M. Wegener, "*Photonic metamaterials by direct laser writing and silver chemical vapour deposition*," Nat. Mater. **7**, 543, (2008).

At conferences (only own presentations):

- M. Hermatschweiler, I. Staude, M. Thiel, M. Wegener, and G. von Freymann, "*Fabrication and Characterization of Silicon Inverse Spiral and Slanted Pore Structures*," contributed talk, DPG-Frühjahrstagung, Darmstadt, Germany, March 2008.

Contents

Chapter 1

Introduction

Reading up on early attempts to capture and manipulate light, one comes across the famous 16th century tale by J. F. von Schönberg, which tells about the unsuccessful efforts of the inhabitants of the fictitious town Schilda, the "Schildbürger", who tried to illuminate the dark rooms of the windowless town hall by shoveling sunlight into bags, jars, and baskets, and carrying it inside [1]. Their spectacular failure nicely illustrates the everyday experience, that trapping and controlling light is difficult, but it also highlights the fascination exerted by this idea already 400 years ago.

While the illumination problem has been solved otherwise in the meantime, the possibility to capture light and precisely control its flow offers unique opportunities for current and future technologies, in particular in the field of optical data communication and processing. This field is driven by the high bandwidth attainable for optical communication channels as well as by several essential advantages offered by photons as information carriers compared to electrons: While electrons exert repelling forces onto each other, no first order interaction effects exist between photons, such that crosstalk is vanishingly small. Furthermore, an additional degree of freedom, which can be utilized for data encoding, is provided by the wavelength of a photon. Finally, the propagation of photons in dielectric media is much faster than the movement of electrons in a wire. For these reasons, the photon has already replaced the electron as information carrier for high-bandwidth long-distance communication. This technical revolution has been made possible by optical fibers, and for pioneering work in this field C. Kao was awarded the Nobel prize in physics 2009.

Yet, since photons do not carry charge, they are much more difficult to control than electrons. A concept which overcomes this problem and offers the desired possibility to precisely control the flow of light has been proposed by S. John and E. Yablonovitch in 1987 [2, 3]. It is based on dielectric materials exhibiting a periodic modulation of their refractive index. Since photons are influenced by the periodically modulated refractive index in a similar way as electrons by the periodic potential of a lattice of ions, such materials can be interpreted as the photonic analogue of an electronic crystal and are therefore called *photonic crystals*.

Fundamental principles of solid state physics, like Bloch wave functions, reciprocal space, Brillouin zones, and band structures can directly be adapted for photonic crystals. In particular, analogously to electronic bandgaps in semiconductors, certain photonic crystal structures have the remarkable property that they support the formation of a *photonic* bandgap, given that the refractive index contrast is sufficiently high. A photonic bandgap is a wavelength region where the propagation of electromagnetic waves is prohibited. If a three-dimensional periodic modulation of the refractive index is present, wave propagation can, under certain conditions, be prohibited for all directions in space.

Based on the concept of a photonic bandgap, many potential applications, *e.g.*, for ultra-high speed data communication, have been proposed. The majority of these applications does not only rely on the existence of a photonic bandgap, but likewise on the systematic introduction of defect structures as functional elements. This can be seen in rough analogy to electronic semiconductor technology, where doping with impurity atoms plays a crucial role.

Until now, most studies on functional elements, both theoretical and experimental, focus on two-dimensional photonic crystals or photonic crystal slabs, because of their relatively simple fabrication in the optical regime by conventional lithography techniques. However, these structures have limited potential for applications because they suffer from an intrinsic weakness: out-of-plane losses. This thesis is therefore devoted to functional elements in three-dimensional photonic bandgap materials, which allow for the confinement of electromagnetic waves in all three spatial directions.

By locally breaking the symmetry of the photonic crystal lattice, states with frequencies in the photonic bandgap can be created. Light coupling to these states will be localized at the defect sites. For point defect cavities created by perturbing a single lattice site, long photon lifetimes in combination with small mode volumes can be obtained. This opens the door for a variety of intriguing devices like optical filters with a high selectivity [4], highly sensitive sensors [5], zero-threshold lasers [6], on-demand single-photon sources [7], and all-optical transistors [8].

However, light cannot only be trapped by defects, but it can also be manipulated in its propagation direction by breaking translational symmetry along an entire row or network of lattice sites. The resulting line or multi-branch defects can find applications as waveguides, beamsplitters, and couplers [9–11]. For three-dimensional photonic bandgap materials they have the potential to guide light along an arbitrary three-dimensional trajectory without any losses. Remarkably, radii of curvature on the order of the wavelength of the guided light can be realized, thereby making a high density of integration possible. The density of integration can further be increased by arranging the optical components like waveguides, cavities, and combinations thereof not only on the surface of wafers, but rather in all three spatial dimensions [12–16]. Moreover, while waveguides are certainly needed to effectively connect the other components on a photonic chip, they can themselves also be used to engineer propagation, dispersion, and polarization properties [17, 18], literally molding the flow of

light. Altogether, three-dimensional photonic bandgap materials are considered a key enabling technology for ultrasmall all-optical integrated circuitry.

This is, however, not the only field of application envisioned for defect architectures in three-dimensional photonic bandgap materials. Amazingly, the possibility to tailor the optical properties of a waveguide mode can, in particular, even be used to accelerate charged particles, thereby providing a potentially cheap and compact alternative to conventional particle accelerators [19].

In order to fabricate a material exhibiting a complete photonic bandgap in a specific region of the electromagnetic spectrum, a three-dimensional periodic structuring of the constituent dielectric material with lattice constants on the order of the corresponding wavelength is required. Aiming at operation wavelengths in the near-infrared spectral region, which is relevant for most potential applications, this is technologically very challenging and even more difficult, when functional defect elements have to be included. As a consequence, despite the tremendous potential offered by the concept of the photonic bandgap, experimental and technological progress has not been as fast as originally expected and hoped for, and actual realizations of defect structures in three-dimensional photonic bandgap materials, in particular waveguide architectures, are truly sparse [20, 21].

A promising approach to meet this fabrication challenge is provided by direct laser writing of polymer templates [22, 23] in combination with subsequent replication or inversion into silicon to enhance the refractive index contrast. Using this approach, high-quality three-dimensional photonic bandgap materials with operation wavelengths in the near-infrared spectral region have already been obtained [24, 25]. The huge advantage of this technology compared to most other fabrication approaches is its outstanding flexibility. For the precise and controlled introduction of designed functional elements into the host structure, this flexibility in combination with a high structural quality is expected to be a crucial success factor. Furthermore, this technology is intrinsically three-dimensional, making it relatively fast and inexpensive compared to sequential fabrication schemes based on two-dimensional lithography [26–30].

The objective of this thesis is to explore the potential offered by this approach to fabricate designed defect elements embedded into three-dimensional photonic bandgap materials, and to investigate the structural and optical properties of the obtained samples. Thereby, the ultimate goal is to experimentally realize structures providing a desired optical functionality, like guiding light, that can be evidenced by optical measurements.

Outline of this Thesis

Chapter 2 starts with an introduction to photonic crystals and their interaction with light. Following this, the properties and basic functionalities of defect elements in photonic crystals are discussed.
In Chapter 3, different photonic bandgap geometries are introduced and the woodpile structure, which serves as a host material for the introduction of functional defect structures in this thesis, is discussed in more detail. The chapter furthermore provides an overview of the current state of the art regarding design, fabrication, and characterization of three-dimensional photonic bandgap materials with embedded functional defects, aiming to provide the relevant context for the results presented later on in this thesis.
Chapter 4 is dedicated to the experimental and numerical methods employed to fabricate and optically characterize photonic bandgap materials both with and without embedded functional elements. In particular, the method of direct laser writing used to obtain three-dimensional photoresist templates is explained and it is shown how the obtained templates can be transferred into silicon structures. Furthermore, the Fourier-transform infrared microscope spectrometer used for optical characterization of the fabricated samples is briefly described. Finally, the plane-wave expansion method and the scattering-matrix formalism are discussed, which are applied to calculate the theoretically expected optical properties for comparison with experimental findings.
Since most potential applications for photonic bandgap materials are targeted on optical signal processing and communication technology, an important prerequisite for photonic bandgap based devices is their potential to operate at telecom wavelengths. In Chapter 5, the existing fabrication technology is therefore systematically improved, leading to an operation wavelength of the realized materials that reaches the $1.55\,\mu\mathrm{m}$ telecommunication wavelength.
Motivated by this, functional defect designs for a point defect cavity and a straight vertical waveguide are developed in Chapter 6. The optical properties of the designed elements are studied theoretically and it is demonstrated experimentally, that their precise and controlled introduction into silicon woodpile photonic crystals using direct laser writing and silicon double inversion is possible.
Chapter 7 focuses on the experimental investigation of light propagation in vertical waveguides. A waveguide-containing silicon woodpile structure is fabricated and corresponding reflectance and transmittance spectra are recorded. Furthermore, an experimental route to tune the spectral position of the waveguide is proposed.
Entering an unconventional field of photonic bandgap applications, Chapter 8 deals with a dedicated waveguide structure inside a three-dimensional photonic crystal, which is expected to allow for laser-driven particle acceleration. The functional principle of this device is explained and subsequently, first experimental steps towards a realization of operating devices are reported.
Finally, the results of this thesis are summarized in Chapter 9 and an outlook on future experiments and research possibilities is given.

Chapter 2

Fundamentals of Photonic Crystals

2.1 Photonic Crystals

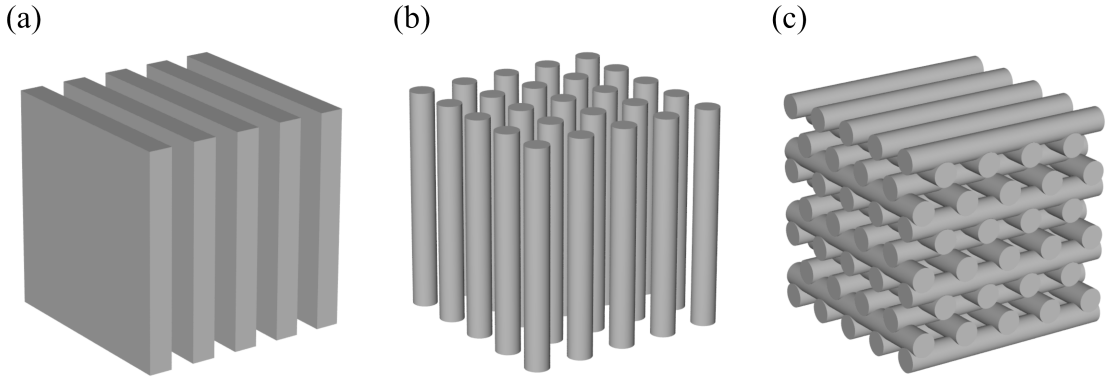

Figure 2.1: Schematical illustration of (a) a stack of dielectric plates, (b) an array of dielectric rods, and (c) a woodpile structure as examples for 1D, 2D, and 3D photonic crystals, respectively.

Photonic Crystals (PhCs) are materials defined by the periodic modulation of their dielectric function. Depending on the number of spatial directions in which this periodic modulation is present, one distinguishes one-, two-, and three-dimensional (1D, 2D, and 3D) PhCs. Figure 2.1 shows an exemplary structure for each of these possibilities. Analogously to an electronic crystal, where the periodic potential of the positive ions can lead to an *electronic* bandgap, the formation of a *photonic* bandgap (PBG) is possible in PhCs. In the first instance, a 1D periodic modulation of the dielectric function leads to frequency regions in the dispersion relation $\omega(\boldsymbol{k})$, with $\boldsymbol{k}$ pointing in modulation direction, where the propagation of electromagnetic waves is prohibited. These regions are called stop bands. If the periodic modulation of the dielectric is present in all three spatial directions, and if the stop bands relevant for different directions in space can be achieved to overlap, a *complete* PBG is formed. Inside a complete PBG no propagating electromagnetic modes exist for any choice of the wave vector $\boldsymbol{k}$. Throughout this thesis, the abbreviation PBG usually refers to such a complete photonic bandgap, and materials featuring a PBG are referred to as PBG-materials. An

exception is made if this abbreviation explicitly refers to 1D or 2D PhCs. In these cases it denotes a frequency region, where the stop bands for all respective directions of periodicity overlap.

The concept of the PhC was first introduced in 1987 by E. Yablonovitch [3] and S. John [2]. In his work, E. Yablonovitch discusses the possibility of a complete suppression of spontaneous emission in a PBG. S. John, on the other hand, focuses on the localization of photons at defect sites in ordered non-dissipative structures. Based on these two publications numerous promising applications for PhCs in general as well as for PBG-materials in particular have been proposed and discussed. However, fabrication of PBG-materials for the near-infrared (NIR) and visible (VIS) spectral regions still poses a major challenge, even more than twenty years after their corresponding prediction by E. Yablonovitch and S. John. The main reason for this lies in the small feature sizes which have to be realized to reach an operation wavelength of the PhC in the NIR or even in the VIS. Their order of magnitude can be estimated making use of the Bragg formula for constructive interference at a set of discrete parallel planes separated by a constant distance a. In perpendicular incidence the Bragg formula reads

$$2na = m\lambda,\ m \in \mathbb{Z}, \tag{2.1}$$

where n is the refractive index and λ the wavelength of the impinging electromagnetic radiation. From this condition, strong interference effects can be expected to occur when the lattice constant and the wavelength are chosen to be comparable in magnitude. In particular, in order to use a PhC for applications at telecommunication wavelengths, lattice constants of $1\ \mu\mathrm{m}$ and below are necessary. For applications in the visible even smaller features have to be realized. Consequently, fabrication of PhC with operation wavelengths in the VIS or NIR is challenging. This is especially true for 3D PhCs since in their case a 3D structuring of the constituent dielectric material is necessary. Progress in this field is reported in [31–34]. Most commonly PhCs consist of dielectric material, but metals have been discussed as constituent materials as well [35, 36]. This thesis, however, exclusively deals with dielectric PhC structures.

This chapter is organized as follows: First the fundamental eigenvalue equation describing ideal PhCs is derived starting from Maxwell's equations. Following this, various properties of the solutions of this fundamental equation are discussed. Finally, the last section of this chapter focuses on defect structures in PhCs and their basic functionalities.

2.2 Interaction of Light with Photonic Crystals

Propagation of light in PhCs is described by the macroscopic formulation of Maxwell's equations. In SI-units these read:

$$\nabla \cdot \boldsymbol{D} = \rho \tag{2.2}$$
$$\nabla \cdot \boldsymbol{B} = 0 \tag{2.3}$$
$$\nabla \times \boldsymbol{E} + \frac{\partial}{\partial t}\boldsymbol{B} = 0 \tag{2.4}$$
$$\nabla \times \boldsymbol{H} - \frac{\partial}{\partial t}\boldsymbol{D} = \boldsymbol{j}, \tag{2.5}$$

where $\boldsymbol{E}$ and $\boldsymbol{H}$ denote the macroscopic electric and magnetic fields, $\boldsymbol{B}$ is the magnetic induction field and $\boldsymbol{D}$ the dielectric displacement field. The symbols ρ and $\boldsymbol{j}$ denote free electric charge and current densities, respectively. Provided that neither free charges nor free currents exist, one can set $\boldsymbol{j} = 0$ and $\rho = 0$. The components D_i of the displacement field are related to the components E_i of the electric field *via*

$$D_i/\varepsilon_0 = \sum_j \varepsilon_{ij} E_j + \sum_{j,k} \chi_{ijk} E_j E_k + O(E^3), \tag{2.6}$$

where $\varepsilon_0 \approx 8.854 \times 10^{-12}\,\mathrm{F/m}$ is the vacuum permittivity [37]. Assuming that the field strengths are small enough to be in the linear regime, χ_{ijk} and all higher order terms can be neglected. Furthermore, if all involved materials are macroscopic and isotropic it is sufficient to replace the dielectric tensor by the scalar dielectric function ε. In addition, explicit material dispersion is ignored in the following. It can implicitly be accounted for by simply choosing the value of the dielectric constant appropriate to the considered frequency range. Finally, focusing on transparent materials, ε can be treated as purely real and positive. Altogether, one obtains

$$\boldsymbol{D}(\boldsymbol{r}) = \varepsilon_0\, \varepsilon(\boldsymbol{r})\, \boldsymbol{E}(\boldsymbol{r}). \tag{2.7}$$

In the above expression it has been included that the spatial dependence of the dielectric function is essential for photonic crystals and has to be taken into account. Analogously, the magnetic induction field $\boldsymbol{B}$ is related to the magnetic field $\boldsymbol{H}$ *via* a corresponding expression:

$$\boldsymbol{B}(\boldsymbol{r}) = \mu_0 \mu(\boldsymbol{r}) \boldsymbol{H}(\boldsymbol{r}), \tag{2.8}$$

where $\mu_0 = 4\pi \times 10^{-7}\,\mathrm{H/m}$ is the vacuum permeability and μ is the relative permeability. With all these assumptions in place, Maxwell's equations (2.2) – (2.5) can be written as

$$\nabla \cdot [\mu(\boldsymbol{r})\, \boldsymbol{H}(\boldsymbol{r}, t)] = 0 \tag{2.9}$$
$$\nabla \cdot [\varepsilon(\boldsymbol{r})\, \boldsymbol{E}(\boldsymbol{r}, t)] = 0 \tag{2.10}$$
$$\nabla \times \boldsymbol{E}(\boldsymbol{r}, t) = -\mu_0 \mu(\boldsymbol{r}) \frac{\partial}{\partial t} \boldsymbol{H}(\boldsymbol{r}, t) \tag{2.11}$$
$$\nabla \times \boldsymbol{H}(\boldsymbol{r}, t) = \varepsilon_0\, \varepsilon(\boldsymbol{r})\, \frac{\partial}{\partial t} \boldsymbol{E}(\boldsymbol{r}, t). \tag{2.12}$$

In the following, the discussion is restricted to fields with a harmonic time dependence. Such fields are referred to as harmonic modes. This is not a real limitation since, as known from Fourier analysis, *any* solution can be constructed with an appropriate combination of these harmonic modes. The fields can thus be written as a spatial pattern (or mode profile) times a complex exponential:

$$\boldsymbol{H}(\boldsymbol{r},t) = \boldsymbol{H}_\omega(\boldsymbol{r})\, e^{-i\omega t} \tag{2.13}$$
$$\boldsymbol{E}(\boldsymbol{r},t) = \boldsymbol{E}_\omega(\boldsymbol{r})\, e^{-i\omega t}. \tag{2.14}$$

Here, $\boldsymbol{H}_\omega(\boldsymbol{r})$ and $\boldsymbol{E}_\omega(\boldsymbol{r})$ are both complex fields. The physically relevant electromagnetic fields are given by their corresponding real parts. Inserting these expressions in the Maxwell equations leads to

$$\nabla \cdot [\mu(\boldsymbol{r})\, \boldsymbol{H}_\omega(\boldsymbol{r})] = 0 \tag{2.15}$$
$$\nabla \cdot [\varepsilon(\boldsymbol{r})\, \boldsymbol{E}_\omega(\boldsymbol{r})] = 0 \tag{2.16}$$
$$\nabla \times \boldsymbol{E}_\omega(\boldsymbol{r}) - i\,\omega\,\mu_0\,\mu(\boldsymbol{r})\,\boldsymbol{H}_\omega(\boldsymbol{r}) = 0 \tag{2.17}$$
$$\nabla \times \boldsymbol{H}_\omega(\boldsymbol{r}) + i\,\omega\,\varepsilon_0\,\varepsilon(\boldsymbol{r})\,\boldsymbol{E}_\omega(\boldsymbol{r}) = 0. \tag{2.18}$$

For simplicity, the subscript ω is skipped in the following. The constants ε_0 and μ_0 are connected to the vacuum speed of light c_0 *via* $c_0 = 1/\sqrt{\varepsilon_0\mu_0}$. Furthermore, the refractive index n can be expressed as $n = \sqrt{\varepsilon\mu}$.
The two divergence equations (2.15) and (2.16) simply state that there are no sources or sinks of displacement or magnetic induction fields in the medium and they enforce any electromagnetic wave solving the Maxwell equations to be transverse. The two curl equations (2.17) and (2.18) can be decoupled by dividing (2.18) by $\varepsilon(\boldsymbol{r})$, taking the curl and finally eliminating $\boldsymbol{E}(\boldsymbol{r})$ with (2.17). This leads to the wave equation

$$\nabla \times \left(\frac{1}{\varepsilon(\boldsymbol{r})}\nabla \times \boldsymbol{H}(\boldsymbol{r})\right) = \left(\frac{\omega}{c_0}\right)^2 \mu(\boldsymbol{r})\boldsymbol{H}(\boldsymbol{r}). \tag{2.19}$$

In combination with the divergence equation (2.15), $\boldsymbol{H}(\boldsymbol{r})$ is completely determined by this expression. With $\boldsymbol{H}(\boldsymbol{r})$ known, Eq. (2.18) can then be used to recover $\boldsymbol{E}(\boldsymbol{r})$:

$$\boldsymbol{E}(\boldsymbol{r}) = \left(\frac{i}{\varepsilon_0\varepsilon(\boldsymbol{r})\omega}\right) \nabla \times \boldsymbol{H}(\boldsymbol{r}). \tag{2.20}$$

In this way the transversality condition $\nabla \cdot [\varepsilon(\boldsymbol{r})\, \boldsymbol{E}(\boldsymbol{r})] = 0$ is fulfilled automatically since the divergence of a curl generally vanishes.

Equation (2.19) can now be re-formulated by identifying the left side of the equation as an operator acting on $\boldsymbol{H}(\boldsymbol{r})$:

$$\hat{\Theta}\boldsymbol{H}(\boldsymbol{r}) = \left(\frac{\omega}{c_0}\right)^2 \mu(\boldsymbol{r})\boldsymbol{H}(\boldsymbol{r}), \tag{2.21}$$

where

$$\hat{\Theta}\boldsymbol{H}(\boldsymbol{r}) = \nabla \times \left(\frac{1}{\varepsilon(\boldsymbol{r})} \nabla \times \boldsymbol{H}(\boldsymbol{r}) \right). \tag{2.22}$$

Finally, natural materials do not show any magnetic response at optical frequencies[1], *i.e.*, $\mu(\boldsymbol{r}) \cong 1$. The wave equation then reads

$$\hat{\Theta}\boldsymbol{H}(\boldsymbol{r}) = \left(\frac{\omega}{c_0} \right)^2 \boldsymbol{H}(\boldsymbol{r}), \tag{2.23}$$

which obviously is an eigenvalue problem. The eigenvalues are proportional to the squared frequencies of the modes, and the eigenvectors $\boldsymbol{H}(\boldsymbol{r})$ are the spatial patterns of these modes. The operator $\hat{\Theta}$ has several useful properties which in turn affect the properties of the solutions. First, $\hat{\Theta}$ is a linear operator. Therefore every linear combination of solutions with the same frequency ω is itself a solution of (2.23). Next, $\hat{\Theta}$ is Hermitian. The eigenvectors are thus orthogonal and have real eigenvalues. They can further be obtained by a variational principle and be cataloged by their symmetry properties. Finally, $\hat{\Theta}$ is positive semi-definite. Therefore the frequencies ω themselves are also real, because the eigenvalues have to be non-negative. The proof that $\hat{\Theta}$ and its eigenfunctions fulfill the above mentioned properties can, *e.g.*, be found in [37].
In order to obtain (2.19), $\boldsymbol{E}(\boldsymbol{r})$ has been eliminated resulting in a formulation of the problem in terms of $\boldsymbol{H}(\boldsymbol{r})$. If choosing instead to eliminate $\boldsymbol{H}(\boldsymbol{r})$ and formulate the problem in terms of $E(\boldsymbol{r})$, it takes the following form

$$\nabla \times \left(\frac{1}{\mu(\boldsymbol{r})} \nabla \times \boldsymbol{E}(\boldsymbol{r}) \right) = \left(\frac{\omega}{c_0} \right)^2 \varepsilon(\boldsymbol{r}) \boldsymbol{E}(\boldsymbol{r}), \tag{2.24}$$

which is completely analogous to (2.19). To fully determine $\boldsymbol{E}(\boldsymbol{r})$ (2.24) has to be taken in combination with the divergence equation (2.16). $\boldsymbol{H}(\boldsymbol{r})$ can then be calculated from $E(\boldsymbol{r})$ using (2.17):

$$\boldsymbol{H}(\boldsymbol{r}) = \left(\frac{-i}{\mu_0 \mu(\boldsymbol{r}) \omega} \right) \nabla \times \boldsymbol{E}(\boldsymbol{r}). \tag{2.25}$$

In contrast to the case of the magnetic response, however, natural materials do show an electric response at optical frequencies, *i.e.*, $\varepsilon(\boldsymbol{r}) \neq 1$. Nevertheless, (2.24) can again be brought into the form of an eigenvalue problem *via* division by $\varepsilon(\boldsymbol{r})$. However, the resulting operator is not Hermitian any more in this case [37]. Therefore, the formulation of the wave equation in terms of $\boldsymbol{H}(\boldsymbol{r})$ is the one more commonly used and also the one referred to in this thesis.
To conclude, a system consisting of linear and dispersionless dielectric media, which does not vary in time and does not contain free charges or currents, can be described as an eigenvalue problem. Even without actually solving the wave equation (2.23) of the system, the form of the operator $\hat{\Theta}$ already provides important information about the solutions. In the following subsection, additional properties of these solutions are identified by taking a closer look at the scaling properties of the wave equation.

[1] For a special class of artificial materials, so-called magnetic metamaterials, this approximation does not hold. They can even exhibit negative values for $\mu(\boldsymbol{r})$ [38].

2.2.1 Scaling Properties of the Wave Equation

A remarkable property of Maxwell's equations in dielectric media is that they are not bound to any fundamental length scale — the wave equation (2.23) is a valid description of the system as long as it is macroscopic. Consequently, if two dielectric structures are connected by a simple expansion or contraction of all distances, the solutions of the corresponding electromagnetic problems have to be connected by simple relationships as well.
An expanded or contracted version $\hat{\varepsilon}(\boldsymbol{r})$ of a dielectric configuration $\varepsilon(\boldsymbol{r})$ can be described by $\hat{\varepsilon}(\boldsymbol{r}) = \varepsilon(\boldsymbol{r}/s)$, where s is a scale parameter. Substituting $\boldsymbol{r} \to \hat{\boldsymbol{r}}/s$ and $\nabla \to s\hat{\nabla}$ in Eq. (2.23) yields

$$s\hat{\nabla} \times \left(\frac{1}{\varepsilon(\hat{\boldsymbol{r}}/s)} s\hat{\nabla} \times \boldsymbol{H}(\hat{\boldsymbol{r}}/s) \right) = \left(\frac{\omega}{c_0} \right)^2 \boldsymbol{H}(\hat{\boldsymbol{r}}/s). \tag{2.26}$$

Identifying $\varepsilon(\hat{\boldsymbol{r}}/s)$ with $\hat{\varepsilon}(\hat{\boldsymbol{r}})$ and dividing by s^2 leads to

$$\hat{\nabla} \times \left(\frac{1}{\hat{\varepsilon}(\hat{\boldsymbol{r}})} \hat{\nabla} \times \boldsymbol{H}(\hat{\boldsymbol{r}}/s) \right) = \left(\frac{\omega}{c_0 s} \right)^2 \boldsymbol{H}(\hat{\boldsymbol{r}}/s), \tag{2.27}$$

which is again the wave equation but now with mode profiles $\hat{\boldsymbol{H}}(\hat{\boldsymbol{r}}) = \boldsymbol{H}(\hat{\boldsymbol{r}}/s)$ and frequencies $\hat{\omega} = \omega/s$. As a consequence of this scaling behavior the operation wavelength of a PhC can in principle be shifted to any desired wavelength simply by appropriately scaling the entire structure. This is, however, only true if material dispersion is indeed negligible. As another consequence it proves useful to express frequency intervals, *e.g.*, the size of a PBG or the bandwidth of a guided mode, as relative quantities, *i.e.*, the width of the interval divided by its center frequency. While both the width of the interval as well as its center frequency are changed by scaling the structure, their ratio is kept constant — it is a characteristic property of the respective structure itself.
A similar behavior of the solutions is found if the dielectric function is subject to a scaling operation of the form $\hat{\varepsilon}(\boldsymbol{r}) = \varepsilon(\boldsymbol{r})/s^2$ with a constant factor s. Inserting this expression into (2.19) one obtains

$$\nabla \times \left(\frac{1}{\hat{\varepsilon}(\boldsymbol{r})} \nabla \times \boldsymbol{H}(\boldsymbol{r}) \right) = \left(\frac{s\omega}{c_0} \right)^2 \boldsymbol{H}(\boldsymbol{r}). \tag{2.28}$$

Obviously, the mode profiles remain unchanged by this scaling operation, while for the frequencies $\hat{\omega}$ of the scaled system the relation $\hat{\omega} = s\omega$ holds. In the practically important case that only two different dielectric constants have to be taken into account it is therefore useful to define the dielectric contrast as the ratio $\varepsilon_{\text{high}}/\varepsilon_{\text{low}}$ of the dielectric constant of the optically denser medium divided by the dielectric constant of the optically less dense medium. From Eq. (2.28) one can then conclude that, as long as $\varepsilon_{\text{high}}/\varepsilon_{\text{low}}$ is kept constant, an arbitrary scaling operation of the dielectric constants will simply lead to a corresponding scaling of the mode frequencies.
Up to now, all considerations have been valid for systems with any spatially varying dielectric function. In the next subsection, the special case of systems with *lattice periodic* modulations of the dielectric functions will be discussed.

2.2.2 Lattice Periodicity

Generally, the photonic modes supported by a dielectric system can be classified according to the symmetries of the system. For PhCs, the particular case of discrete translational symmetry is of outstanding importance, since they are actually defined by the periodic modulation of their dielectric function. Formally, this is expressed as

$$\varepsilon(\boldsymbol{r} + \boldsymbol{R}) = \varepsilon(\boldsymbol{r}) \tag{2.29}$$

with lattice vectors

$$\boldsymbol{R} = \sum_i p_i \boldsymbol{a}_i, \qquad p_i \in \mathbb{Z}, \tag{2.30}$$

where the $\boldsymbol{a}_i$ are the fundamental lattice vectors of the PhC. For 3D PhCs one has $i = 1, 2, 3$. The fundamental reciprocal lattice vectors $\boldsymbol{b}_j$ with $j = 1, 2, 3$ can then be defined by

$$\boldsymbol{a}_i \cdot \boldsymbol{b}_j = 2\pi\delta_{ij}, \tag{2.31}$$

where δ_{ij} is the Kronecker symbol. The reciprocal lattice vectors $\{\boldsymbol{G}\}$ are given by

$$\boldsymbol{G} = \sum_{i=1,2,3} l_i \boldsymbol{b}_i, \qquad l_i \in \mathbb{Z}. \tag{2.32}$$

Since $\varepsilon(\boldsymbol{r})$ is a periodic function of the space coordinate $\boldsymbol{r}$ the Bloch theorem (see, *e.g.*, [39]) can be applied to (2.23). Consequently, $\boldsymbol{H}(\boldsymbol{r})$ can be written as

$$\boldsymbol{H}(\boldsymbol{r}) = \boldsymbol{H}_{\boldsymbol{k}m}(\boldsymbol{r}) = \boldsymbol{u}_{\boldsymbol{k}m}(\boldsymbol{r})\, e^{i\boldsymbol{k}\cdot\boldsymbol{r}}, \tag{2.33}$$

where $\boldsymbol{u}_{\boldsymbol{k}m}(\boldsymbol{r})$ is a spatially periodic vectorial function

$$\boldsymbol{u}_{\boldsymbol{k}m}(\boldsymbol{r} + \boldsymbol{R}) = \boldsymbol{u}_{\boldsymbol{k}m}(\boldsymbol{r}). \tag{2.34}$$

In a periodic system, $\boldsymbol{k}$ is a conserved quantity modulo the addition of reciprocal lattice vectors and thus $\boldsymbol{H}(\boldsymbol{r})$ is completely determined by the wave vector $\boldsymbol{k}$ within the first Brillouin zone (1st BZ) in combination with the band index m. The same applies for the corresponding eigenvalues, that is, for the frequencies $\omega_m(\boldsymbol{k})$. Plotting the $\omega_m(\boldsymbol{k})$ as a function of the wave vector $\boldsymbol{k}$ in the irreducible Brillouin zone, *i.e.*, the smallest region within the 1st BZ, for which the $\omega_m(\boldsymbol{k})$ are not related by rotation, mirror-reflection, or inversion symmetry, yields the band structure (or, equivalently, the band diagram).

2.2.3 Photonic Bandgaps

In the last subsections, various fundamental properties of the solutions to the wave equation (2.23) have been discussed. However, an intuitive explanation for the formation of a PBG,

or, more generally, of a stop band, and its physical origin is still missing. This gap can be closed by considering the Rayleigh quotient

$$U_f(\boldsymbol{H}) \triangleq \frac{(\boldsymbol{H}, \hat{\Theta}\boldsymbol{H})}{(\boldsymbol{H}, \boldsymbol{H})}, \tag{2.35}$$

where

$$(\boldsymbol{F}, \boldsymbol{G}) \triangleq \int d^3\boldsymbol{r}\, \boldsymbol{F}^*(\boldsymbol{r}) \cdot \boldsymbol{G}(\boldsymbol{r}) \tag{2.36}$$

is the inner product of two vector fields $\boldsymbol{F}(\boldsymbol{r})$ and $\boldsymbol{G}(\boldsymbol{r})$. The asterisk denotes complex conjugation. According to the variational theorem for Hermitian operators, this Rayleigh quotient is minimized by the lowest-frequency mode, subject to transversality $\nabla \cdot \boldsymbol{H}(\boldsymbol{r}) = 0$ [37]. The minimum value of U_f is the smallest eigenvalue ω_0^2/c_0^2. The eigenmode with the next-lowest eigenvalue will minimize U_f within the subspace of functions orthogonal to lowest-frequency mode, and so on. U_f can be rewritten in terms of the electric field $\boldsymbol{E}$, yielding

$$U_f(\boldsymbol{H}) = \frac{\int d^3\boldsymbol{r}\, |\nabla \times \boldsymbol{E}(\boldsymbol{r})|^2}{\int d^3\boldsymbol{r}\, \varepsilon(\boldsymbol{r})\, |\boldsymbol{E}(\boldsymbol{r})|^2}. \tag{2.37}$$

The lowest-frequency eigenmode is now given by the field $\boldsymbol{E}$ that minimizes (2.37), subject to $\nabla \cdot [\varepsilon(\boldsymbol{r})\boldsymbol{E}(\boldsymbol{r})] = 0$. From this expression it can now be seen that U_f is minimized when the electric field $\boldsymbol{E}$ is concentrated in regions of high dielectric constant for a given amount of spatial oscillations. A mode which concentrates a high fraction of its electric field energy in the high-ε regions therefore has a lower frequency than a mode having a larger fraction of its energy concentrated in the low-ε regions. While all modes therefore tend to concentrate their energy in the high-ε regions, higher modes have the additional constraint to be orthogonal to the modes lying below.

A simple model system showing how this can lead to the formation of a PBG is a multilayer stack, or, in other words, a 1D PhC with lattice constant a, which consists of alternating layers of two materials with different dielectric constants. In the following the thickness of each layer is assumed to be $a/2$. Figure 2.2 shows the band diagrams of three different multilayer stacks. k is oriented in direction of the periodic index modulation. Instead of k, the dimensionless wave vector $ka/2\pi$ is plotted on the x-axis to account for the scalability of the system. The three cases differ by the values assumed for the dielectric contrast, which increases from left to right. In Fig. 2.2 (a) its value is 1, which corresponds to a homogeneous medium with refractive index n and arbitrarily assigned periodicity a. In this case the band structure can directly be obtained from the dispersion relation of the homogeneous medium $\omega = c_n k$, which is folded back at the edges of the 1st BZ. Here, $c_n = c_0/n$ denotes the speed of light in the medium. It is not surprising that a stop band, or (1D) PBG, cannot yet be observed in this case. This changes as soon as the dielectric contrast becomes slightly larger than 1. This case is plotted in Fig. 2.2 (b) for a dielectric contrast of 1.33. While the first and the second band are degenerate at the edge of the 1st BZ for the homogeneous medium, this degeneracy is now lifted by the finite dielectric contrast. As a consequence, between the first

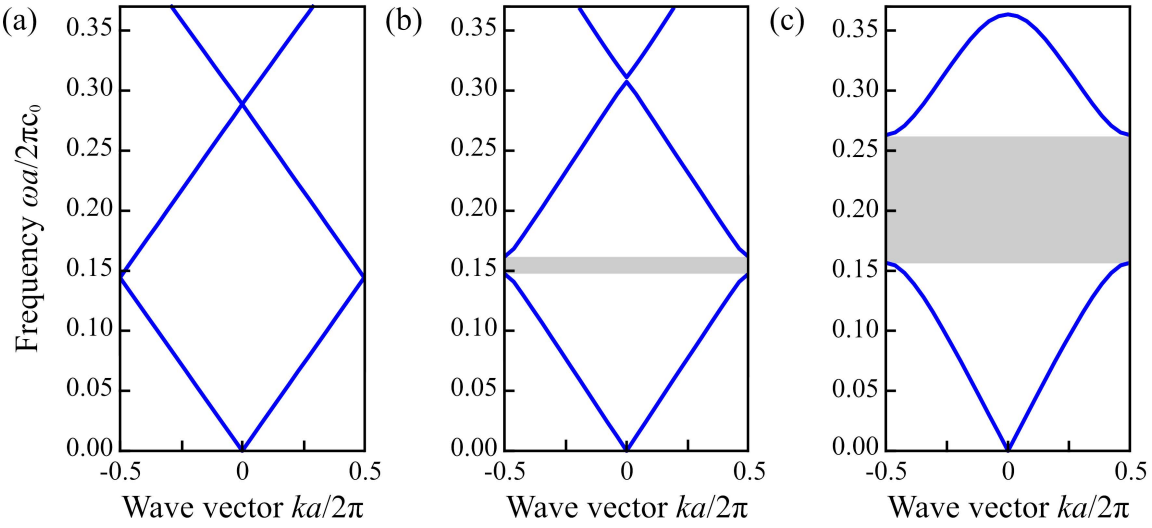

Figure 2.2: Band structure of a 1D PhC with a dielectric contrast of (a) 1 (b) 1.33, and (c) 12. The (1D) PBGs are marked in gray. Adapted from [37].

two bands a frequency region occurs where no propagating modes exist, that is, a PBG is formed. By further increasing the value of the dielectric contrast the width of the stop band also increases, as observable from Fig. 2.2 (c), where a dielectric contrast of 12 is chosen.

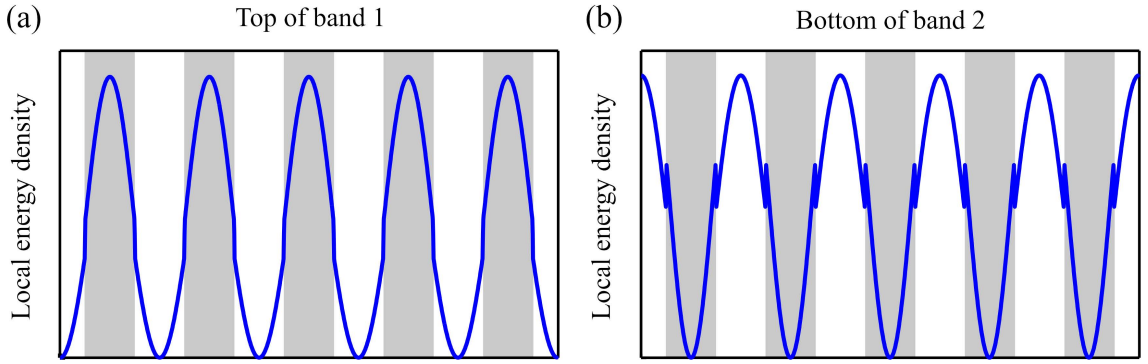

Figure 2.3: Time-averaged local energy density of the electric field (a) of the first and (b) of the second band at the edge of the 1st BZ. In the depiction of the multilayer stack, regions of high dielectric constant ($\varepsilon = 12$) are marked in gray, regions of low dielectric constant ($\varepsilon = 9$) in white. Adapted from [37].

The physical origin of the PBG becomes obvious when comparing the spatial distributions of the time-averaged electric-field energy density $\varepsilon \left|\boldsymbol{E}(\boldsymbol{r})\right|^2$ of the first two bands at the original degeneracy point. This is done in Fig. 2.3 for the dielectric contrast of 1.33, corresponding to the band structure depicted in Fig. 2.2 (b). Clearly the energy of the first band is concentrated in the regions of high refractive index while the second band has a higher amount of its energy in the regions of low refractive index in order to remain orthogonal to the first. Consequently, the denominator in (2.37) is smaller for the second band and thus the frequency

of the second band is higher compared to that of the first band and a gap is formed in the frequency spectrum. The modes above and below the PBG can be characterized by their amount of electric field energy concentrated inside regions of high $\varepsilon(\boldsymbol{r})$, which is higher for the mode below the gap. The latter one is therefore called the *dielectric band* while the mode above the gap is referred to as *air band*, expressing the fact that in many cases the low index material is air.
In higher dimensional PhCs the formation of PBGs is based on the same principle. However, not all of the results obtained for the multilayer stack can be generalized to more complex geometries. In particular, to obtain a PBG in 2D or 3D PhCs, the stop bands have to overlap for all respective directions of periodicity in the structure. To this end it is not sufficient to introduce an arbitrarily small dielectric contrast. Instead, PBG formation sensitively depends on the specific geometry and the value of the index contrast, which typically has to exceed a structure-specific minimum value. Especially in 3D, it is not a trivial task to identify geometries supporting a PBG. In Section 3.1 some well-known 3D PBG structures will be listed and the woodpile geometry will be described in more detail.

2.2.4 Optical Spectra of Photonic Crystals

A common way to optically characterize PhCs experimentally is by measurement of their transmittance and/or reflectance spectra. This paragraph deals with the question of how the band structure of a PhC is linked to these experimentally accessible properties. In order to understand the connection between the spectra of a given PhC and its band structure it is useful to consider the crystal's total density of states (DOS), given by [40]:

$$D(\omega) = \sum_m \int_{1.\mathrm{BZ}} d^3\boldsymbol{k}\ \ \delta\left(\omega - \omega_m(\boldsymbol{k})\right). \tag{2.38}$$

The eigenstates of the system are indexed by m, their corresponding frequencies are denoted with $\omega_m(\boldsymbol{k})$. For comparison, the density of states of the radiation field in the volume V of free space is given by

$$D(\omega) = \frac{\omega^2 V}{\pi^2 c^3}. \tag{2.39}$$

Using expression (2.38), the DOS inside a PhC can in principle be directly calculated from its band structure.
The DOS itself is further connected to the transmittance spectra of a finite PhC structure, since, in order to propagate through the PhC, electromagnetic waves have to couple to the crystal states. Inside a PBG, for example, where the DOS is zero, no modes can propagate through the crystal irrespective of their direction of incidence and consequently transmittance in the gap vanishes. Reflectance, on the other hand, becomes one, such that the PBG-material acts as a perfect mirror for frequencies in the gap. However, a weak point of this attempt to predict the optical spectra of a PhC from its band structure is that surface effects and finite thickness effects are not taken into account. Consequently, for any finite PhC, transmittance in the PBG is not strictly zero as suggested by this method, but merely strongly suppressed,

and reflectance is very close to one, but not exactly one. Outside the PBG, the actual dependencies are even more complicated since the DOS does not carry any information about how efficiently a wave impinging from free space couples to a given band. In the extreme case of complete symmetry mismatch between the impinging plane wave and a given band, this band will not show up in the transmittance spectrum although the DOS is non-zero. While group theoretical considerations can be useful for a detailed analysis of symmetries and coupling properties [41], in practice other approaches to calculate transmittance and reflectance spectra of PhC structures have proven more useful. One of these approaches is the scattering-matrix method, which has been applied for the calculation of the theoretical spectra shown in this thesis. This method will be discussed in detail in Subsection 4.4.2.

2.3 Defect Structures in Photonic Crystals

2.3.1 Breaking Translational Symmetry

PhCs are frequently described as the photonic analogue to electronic semiconductors. In this picture, a perfect PBG material corresponds to an undoped bulk semiconductor material. As obvious from the electronic case, this situation is far from fully exploiting the opportunities offered by the concept of the bandgap. As in semiconductor electronics, the majority of potential PhC applications is instead based on the controlled incorporation of defects as functional elements. Numerous examples for such applications have already been listed in the introduction (see Chapter 1). In the following, different possibilities of defect creation and their respective fundamental properties are discussed.

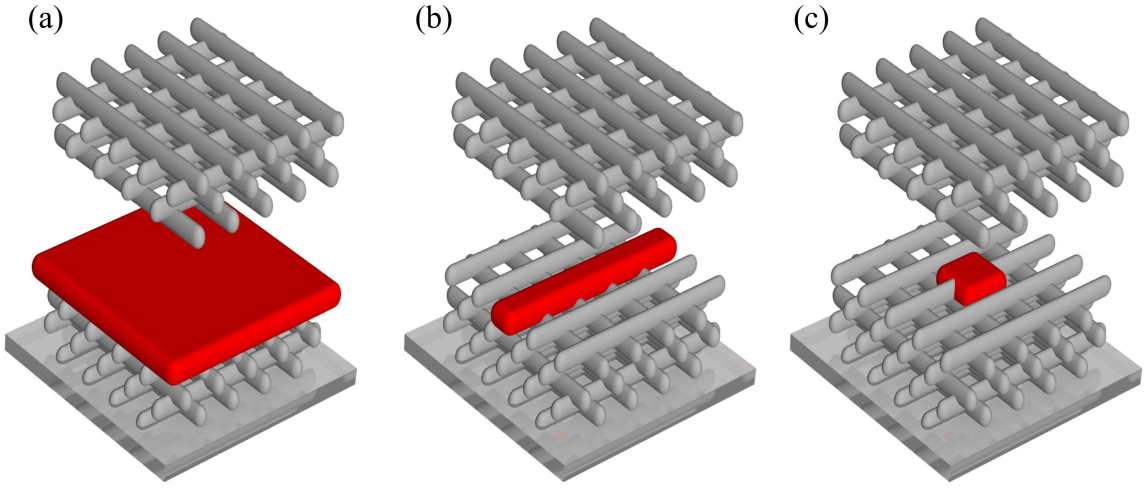

Figure 2.4: Example geometries for defects with different dimensionality: (a) planar defect, (b) linear defect, and (c) point defect.

A defect is introduced into a PhC by locally breaking the perfect symmetry of the PhC lattice. One way to classify such defects is by the number of directions in space in which the

periodicity of the perfect PhC lattice is broken. Examples for the three different possibilities offered by a 3D PhC are given in Fig. 2.4, where in all three cases the upper part of the lattice has been elevated in order to reveal the defect elements (marked in red) embedded inside the PhC structures. In these examples, the woodpile structure described in Section 3.1 is chosen as a host PBG-material for the defects. If translation symmetry is broken in only one direction, as illustrated in Fig. 2.4 (a), a planar defect or, in other words, a defect plane is created. If the break in symmetry is present in two directions simultaneously, as depicted in Fig. 2.4 (b), one obtains a linear defect or line defect. If finally symmetry is broken in all three spatial directions, as in Fig. 2.4 (c), a point defect is formed. The number of spatial directions in which the translational symmetry of the PhC is broken by the defect determines in how many dimensions light can be confined by the defect. The physical origin of this confinement is the topic of the next subsection.

2.3.2 Localization of Light at Defect Sites

The fact that light can be localized at defect sites inside a PBG material can intuitively be understood in a very simple model. As stated earlier, within the frequency range of the PBG the PBG-material acts as a perfect mirror for incident light impinging from all possible directions. Consequently, if there is a hole inside the PBG-material and if an electromagnetic wave is exited inside this hole with a frequency lying within the PBG, the wave has no possibility to propagate out of the hole and will be trapped inside.
This simple model gives rise to the question what exactly happens when the light trapped inside is impinging onto the walls of the hole. No propagating electromagnetic modes are allowed to have frequencies within the PBG, *i.e.*, no purely real wave vector exists for the mode trapped inside the hole. However, exponentially decaying evanescent modes of the form

$$\boldsymbol{H}(\boldsymbol{r}) = e^{i\boldsymbol{k}\cdot\boldsymbol{r}}\boldsymbol{u}(\boldsymbol{r})e^{-\boldsymbol{\kappa}\cdot\boldsymbol{r}} \tag{2.40}$$

are not at all forbidden by the existence of the PBG. This expression is analogous to (2.33), with the only difference that the wave vector $\boldsymbol{k} + i\boldsymbol{\kappa}$ is complex here. The imaginary part of the wave vector causes the mode to decay exponentially on a length scale of $1/\kappa$. Here, κ is the projection of $\boldsymbol{\kappa}$ onto the respective spatial direction. These evanescent modes are fully valid solutions of the eigenequation (2.19). A defect in the perfect lattice can under certain circumstances sustain such a mode. In this case it is possible to obtain an exponentially localized state inside the PBG.

In order to explain the origin of the complex wave vector it is useful to take another look at the band structure of a simple multilayer stack depicted in Fig. 2.2 (c). The second band is now expanded in leading order into a Taylor series in k about the zone edge $k = \pi/a$, yielding [37]:

$$\Delta\omega = \omega_2(k) - \omega_2\left(\frac{\pi}{a}\right) \approx \alpha\left(k - \frac{\pi}{a}\right)^2 = \alpha(\Delta k)^2. \tag{2.41}$$

This expression has been simplified using $\omega_m(\boldsymbol{k}) = \omega_m(-\boldsymbol{k})$, which holds for all PhCs, except magneto-optic materials [37]. In the case of $\Delta\omega < 0$ the frequencies lie in the (1D)

PBG and Δk has to be purely imaginary. This means $\Delta k = i\kappa$ and the fields are decaying exponentially. By approaching the center of the PBG the decay constant κ increases. Usually it is largest in the middle of the PBG. As a direct consequence, the strongest localization can usually be achieved for modes with frequencies lying at midgap.

Naturally, pure gap localization can only take place in those spatial directions where a PBG is present. Consequently, a 1D PhC can confine light to a plane, a 2D PhC to a single line, but only a 3D PhC can confine light in all spatial dimensions, *i.e.*, to a point [42].
However, there is one particular feature that distinguishes point defects in 3D PBG-materials from all other cases: In three dimensions the defect must exceed a critical size or strength in order to obtain localizing power. In contrast, in the one- and two-dimensional case typically even arbitrarily small defects can create localized modes. This is the electromagnetic analogue to a theorem from quantum mechanics which states that in one and two dimensions an arbitrarily weak attractive potential has bound states, while this is not the case in three dimensions [43, 44].
Of course, gap localization is not the only mechanism that serves to confine light. Conventional devices, like, *e.g.*, common optical fibers, usually rely on total internal reflection, called index guiding in this context. A remarkable property of gap localization compared to total internal reflection is that light can not only be confined to a dielectric, but it can as well be localized primarily in air. This is a crucial property for certain potential applications, as will be pointed out in the following subsection. Different combinations of gap localization and index guiding are also in use. 2D PhC slabs, for example, combine localization in a 2D band gap with total internal reflection in the third dimension. Based on this concept, even 3D localization can effectively be achieved. This and the fact that fabrication is relatively easy compared to 3D structures (see Section 3.3) have made 2D PhC slabs to an extensively studied PhC architecture. However, devices based on 2D PhC slabs inherently suffer from out-of-plane losses into the third dimension.

2.3.3 Dielectric Defects and Air Defects

In principle, there are two possibilities to introduce a defect of given dimensionality into the PhC. One is by locally increasing the dielectric constant, the other one is by locally reducing the dielectric constant. Speaking in terms of PhCs composed of only two different materials, one of which is air, this translates to locally adding or taking away high-index material. In the first case a *dielectric* or *donor-type* defect is created, in the second case one obtains an *air* or *acceptor-type* defect [45]. Figure 2.5 (a) and (b) illustrate these two possibilities for point defects introduced into a 3D woodpile PhC. Again the upper part of the host structure has been elevated in order to reveal the added dielectric or defective rods, respectively, (both marked in red) embedded inside.
The choice for one of the two possibilities has direct consequences for the DOS of the defect-containing PBG-material. When continuously increasing the size of a defect starting from zero, defect states are gradually pulled downwards into the PBG from the air band for a dielectric defect, while for an air defect the defect states originate from the dielectric band and

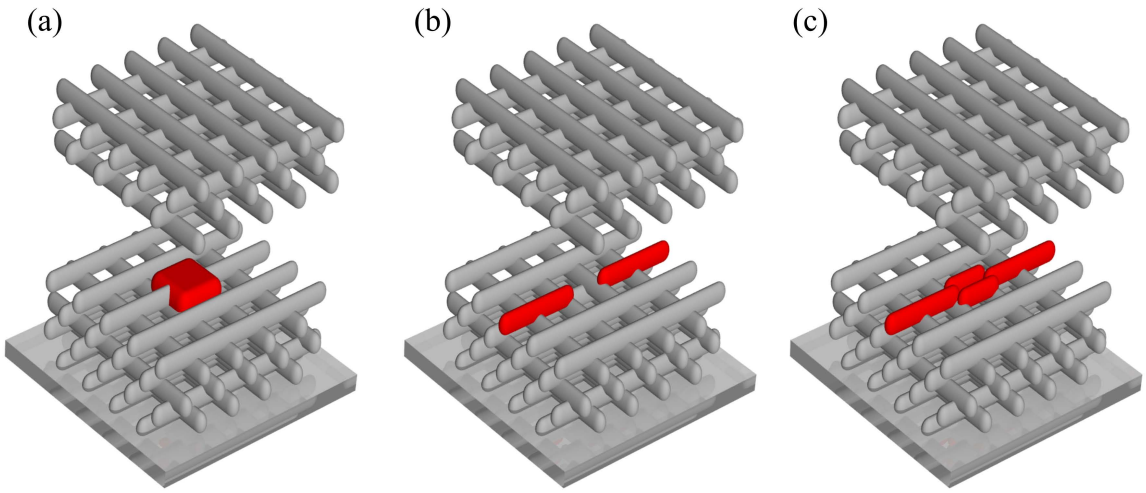

Figure 2.5: Examples for a 3D PhC containing (a) a dielectric defect, (b) an air defect, and (c) a compound defect.

are lifted upwards into the PBG. As a third, rather exotic way to introduce a defect, one could think of combining the two possibilities, *i.e.*, adding high-index material at a certain position and at the same time cutting high-index material away at another position in immediate vicinity to the added material. An example for this type of defect is illustrated in Fig. 2.5 (c). Defects based on this idea can be found under the name *compound* defects in the literature [46].
The choice for one type of defect depends on the kind of application one has in mind. Since for an air defect the energy can be concentrated predominantly in air, light-material interactions like loss or dispersion can be engineered to be small. In addition, empty physical space is created where the dielectric material is removed, which can be re-populated by, *e.g.*, gas atoms or charged particles (see Chapter 8), directed there to interact with the light field of the defect mode. Vice versa, dielectric defects can serve to enhance light-material interactions, like, *e.g.*, nonlinearities, when this is desired. Furthermore, they offer opportunities to place embedded emitters, as for example quantum wells or quantum dots, directly inside the defect material.

2.3.4 Basic Functionalities of Defect Structures

In the last subsection, different defect types and possibilities to introduce them into the PBG-material have been pointed out. This subsection now focuses on two fundamental functional elements which can be formed by PhC defect structures, namely point defect cavities and line defect waveguides.

Photonic Crystal Point Defect Cavities

If the perfect periodicity of the PBG-material is broken by perturbing a single lattice site, or more generally, by locally changing the crystal geometry in a way that symmetry is broken in all spatial directions of periodicity, a single localized mode or a set of closely spaced localized modes with frequencies in the gap are created. Due to the symmetry break the modes can no longer be classified by the wave vector $\boldsymbol{k}$, because it is not a conserved quantity any more. Therefore it is useful to consider the PhC's DOS rather than the band structure. In the PBG there are no modes, in other words, the DOS is zero. The defect cavity, however, introduces a single peak into the DOS for every supported mode, which can lie inside the PBG. Such a peak is described by a Dirac delta function. Recalling the connection between the DOS and the transmittance spectra of a PhC, a sharp peak is expected in the stop band as the signature of a cavity mode with resonance frequency in the PBG, as long as coupling to the incident wave is not forbidden by symmetry.

While these are general features of resonant cavities in PBG-materials, the exact way in which the perturbation is introduced offers the possibility to engineer the cavity's specific optical properties. The shape of the defect will, for example, have consequences on the appearance of its mode profiles. In particular, based on the symmetry of the defect, the modes can be classified using group theory, resulting in a set of allowed mode profiles [47]. Another design parameter is the size, or more generally, the strength of the defect. Its choice influences the number of localized modes in the PBG. As a trend, the number becomes higher as defect size is increased. It further determines the spectral position of the defect modes and can, *e.g.*, be adjusted to tune the frequency of a particular mode to the middle of the PBG for optimized localization [45]. On the other hand, cavity modes can be shifted out of the PBG by variation of the cavity size. This leads to the formation of leaky modes, also called resonances, because energy can now leak away into the continuum of states. For a finite crystal, every cavity mode, even if its frequency lies inside the PBG, is a leaky mode, because the mode has a nonzero leakage rate γ into the surrounding medium. Since defect modes decay exponentially away from the defect site, γ also decreases exponentially with the number of lattice constants surrounding the defect. Thus, in a 3D PBG-material, the loss rate can, in principle, be made arbitrarily small. A measure for the inverse loss rate commonly used for PhC cavities is the quality factor.
The mode associated with a lossy cavity can be described as a mode with complex frequency $\omega_c = \omega_0 - i\gamma/2$. The imaginary part of the complex frequency causes the fields of the mode to decay as $e^{-\gamma t/2}$ and its energy as $e^{-\gamma t}$. In principle, γ is already a measure for the loss rate, but since Maxwell's equations are scale-invariant it is useful to use the dimensionless quantity $1/Q$ with

$$Q = \frac{\omega_0}{\gamma} = \frac{\omega_0 U}{P}, \tag{2.42}$$

where P is the outgoing power and U the electromagnetic energy inside the cavity. Q counts the number of optical periods that elapse before the energy decays by $e^{-2\pi}$ and can therefore be understood as a dimensionless lifetime. As a consequence, the peak that has been

introduced into the crystal's DOS by the lossy cavity can no longer be described by a delta peak. Instead, the fractional bandwidth of the peak widens as Q decreases. More specifically, the Fourier transform of the time-varying field in the cavity has a squared amplitude that is a Lorentzian peak ($\propto\ 1/\left[(\omega-\omega_0)^2+(\omega_0/2Q)^2\right]$). The fractional width of this peak at half-maximum is $1/Q$. If a cavity has several different loss channels, it is useful to describe each channel with a separate Q. The total quality factor is then obtained by adding the corresponding decay rates, that is, for N channels $1/Q_{total}=\sum_{i=1}^{N}1/Q_i$.
For optical microsphere resonators experimental Q-factors of almost 10^{10} have been measured [48], while for 2D PhC point defect cavities experimental Q-factors around 45,000 can be obtained [49]. The so far highest experimental Q-factor for point defect cavities in 3D PBG-materials reaches a value exceeding $10,000$ [50]. An overview over experimentally obtainable quality factors for 3D PBG cavities is embedded in Section 3.4.
Another quantity which is frequently mentioned in the context of PhC cavities is the modal volume V_{mode}. Using PhC cavities very small values for V_{mode} can be realized compared to the values attainable with dielectric resonators based on index guiding. A small modal volume is desirable for most potential applications, because it allows for a high level of miniaturization and low power requirements of optical components. In addition, if an emitter placed inside a cavity and the cavity mode itself have the same frequency, the rate of spontaneous emission is enhanced proportional to Q/V_{mode} [51], thus making PhC cavities with high Q and small V_{mode} an ideal system to explore cavity quantum electrodynamics phenomena. Different definitions of the modal volume exist, depending on the physical process to be optimized. Independent of the precise definition, V_{mode} is typically given in scale-invariant units of $(\lambda/2n)^3$.

Photonic Crystal Waveguides

In contrast to point defects, that provide the functionality to *trap* light at a defect site inside the PhC, line defects can *guide* light from one location inside the PhC to another. A line defect is created by modifying not only one single unit cell but an entire sequence of unit cells. As for the point defect, the defect modes will be localized within the defect region. However, the difference is that, by introducing a line of defects, discrete translational symmetry is preserved along this line. As a consequence, the wave vector $k_{||}$ pointing in direction of this line is still a conserved quantity. Light is therefore allowed to propagate along the line defect, which thus acts as a waveguide. In this case the defect mode is no longer characterized by a fixed frequency, as for the point defect, but it shows a dispersive behavior with dispersion relation $\omega(k_{||})$.
As already found in the case of point defect cavities, the geometry of the defect can again be used to engineer the various optical properties of the waveguide. The cross section of the waveguide, for example, can be used to tune the position of the guided modes' midband frequencies within the band gap. Furthermore, a waveguide can be single-mode or multi-mode, depending on its specific design and size. As a rule of thumb: the larger the cross section of the waveguide, the more modes are shifted into the PBG. For applications involving information transmission applications, single-mode operation is usually desired in order to prevent

signals from propagating with different velocities. Another property of technical relevance is the bandwidth of a guided band. A waveguide with a broad bandwidth can guide light of different frequencies or, connected to this, short pulses, while a waveguide with a small bandwidth has a more selective functionality, which can be used, for example, for optical filters.

Another fundamental property of a waveguide mode is its group velocity $v_g = d\omega/dk_{||}$, that is, the velocity with which the mode propagates inside the defect channel. A small v_g corresponds to slow light, which can be used to enhance the effects of light-material-interactions, as for example optical nonlinearities, when this is desired [17]. One way to obtain slow light is by coupled-cavity waveguides [18]. Instead of altering *all* adjacent unit cells lying along the defect line, one creates a sequence of point defects which are separated by one or more unit cells. Doing this, periodicity is maintained and therefore it is still a waveguide, but group velocity decreases exponentially with defect separation [37].

Connected to the group velocity is the group velocity dispersion $\propto dv_g/d\omega$. It is a measure for how fast pulses propagating in the waveguide will spread because its different spectral components are traveling at different velocities [52]. For the transmission of signals a small group velocity dispersion is needed. On the other hand, the potential to engineer dispersion in a controlled way is of interest by itself.

Up to now only properties of *straight* waveguides have been discussed. However, a remarkable opportunity offered by PhC waveguides is that waveguide bends or splitters with radii of curvature smaller than a wavelength can be realized, for which 100% transmission is achieved [9–11]. For comparison, in conventional waveguides losses increase exponentially with decreasing bend radius of curvature [53].

Chapter 3

A Survey of Photonic Crystals with Defects

This chapter aims at giving an overview of the current state of the art regarding design, fabrication, and characterization of 3D PBG-materials with embedded functional defects in order to provide the relevant context for the results presented later on in this thesis. Before actually concentrating on defect structures different host PBG-materials are discussed and the woodpile geometry, which is the basis for all structures investigated in this thesis, is described in detail. Following this, a variety of point and line defect designs, which have been proposed in the literature for the woodpile structure, are presented. Next, different fabrication methods for the introduction of defects in 3D PBG-materials are briefly reviewed, and finally the few experimental realizations, whose optical functionality is actually documented by appropriate measurements, are discussed in more detail.

3.1 Photonic Bandgap Geometries

3.1.1 Overview

Three years after the prediction of 3D PBGs in periodic structures [2, 3] a specific 3D dielectric structure has first been correctly computed to have a PBG by K. M. Ho *et al.* [54]. This first PBG-material consists of overlapping spheres arranged in a diamond lattice. The PBG exists both for dielectric spheres in air and for air spheres in dielectric[1], and, in the latter case, a gap-midgap ratio of 29.6% can be reached for a dielectric contrast of 13. One year later the first experimental PBG structures have been realized by E. Yablonovitch *et al.* [55] with operation wavelengths in the microwave regime. They have been fabricated by drilling holes along the three lattice vectors of the face-centered cubic (fcc) lattice. For a dielectric contrast of 13 and holes with a radius of $r = 0.234\,a$ a gap-midgap ratio of 19% is achieved in this structure, which has been named *Yablonovite*. Subsequently, numerous systems exhibiting large PBGs have been proposed, among them woodpile and inverse woodpile PhCs

[1] This structure must not be confused with an artificial opal, where the spheres are arranged in a fcc lattice and which does not support a PBG for dielectric spheres in air.

[56, 57], slanted pore and slanted rod PhCs[2] [58, 59], inverse opals [60, 61], stacks of 2D PhCs [62], holographic geometries [63], square spirals [64], and circular spiral structures [65]. Interestingly, not only conventional 3D PhCs but also amorphous structures with a

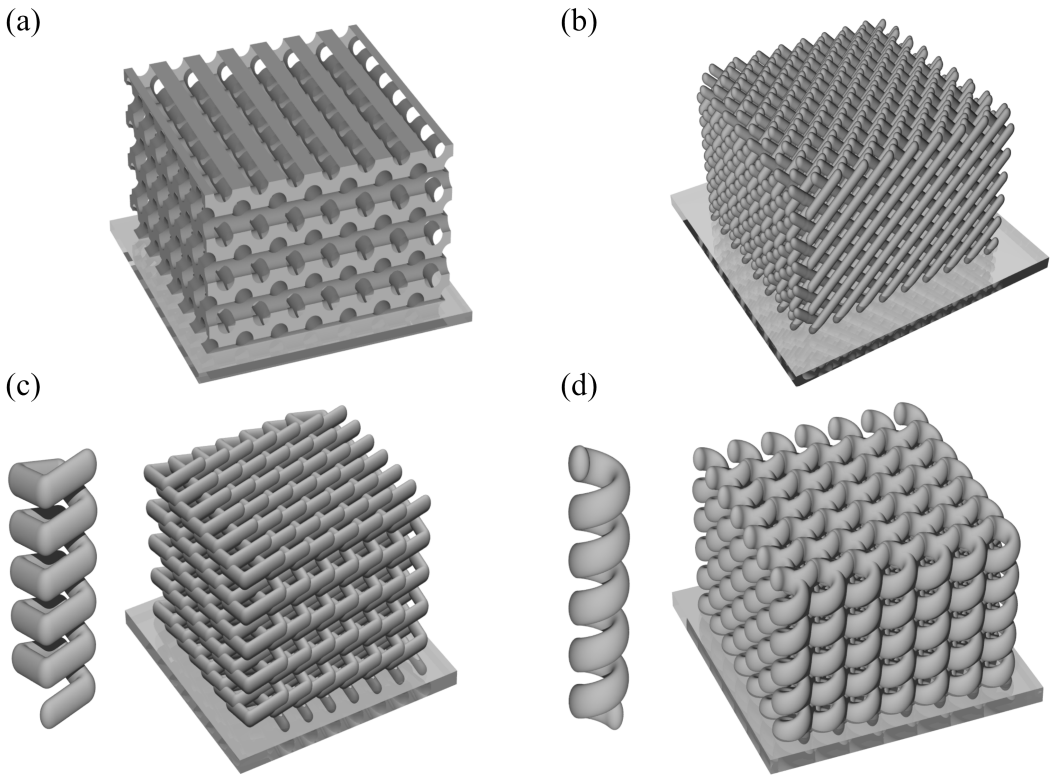

Figure 3.1: 3D renderings of exemplary PBG geometries: (a) an inverse woodpile structure, (b) a slanted rod PhC, (c) a square spiral PhC, and (d) a circular spiral structure. In (c) and (d) the insets show the respective basic building blocks.

complete lack of translational symmetry can exhibit a large PBG, as reported in [66] for an amorphous diamond PhC. An overview over some of the most important PBG-material geometries and their respective properties is, *e.g.*, provided in [37]. By use of the fabrication methods described in Chapter 4, a whole palette of the above mentioned PBG-materials becomes experimentally accessible, both in their direct and in their inverse forms, among them woodpiles, slanted pore PhCs, square spirals, and circular spiral structures. Each of these geometry types comprises an entire family of PBG-materials, whose members follow a similar construction scheme but differ in their structural parameters or in the specific arrangement of their constituent building blocks. An example for each of these geometry types is illustrated in Fig. 3.1. Large PBGs are supported not only by the depicted structures, but, for suitable structural parameters, also by their respective inverse counterparts.

[2]Woodpile PhCs are actually a subclass of slanted rod PhCs.

3.1.2 The Woodpile Structure

From all the experimentally accessible geometries listed in the previous subsection, the direct woodpile structure is chosen as host PBG-material for the introduction of functional defect structures in this thesis. Even if it is not the structure with the largest attainable PBG, it offers several advantages making it the ideal structure for this purpose: First, it is a direct structure. This is a plus factor since the fabrication of direct structures is technologically less demanding and therefore more reliable than the fabrication of inverse structures (see Subsection 4.2.4). Second, numerous theoretical defect design proposals for the woodpile structure already exist in the literature (see Section 3.2), while this is not the case for the other geometries accessible by the fabrication approach used in this thesis. Although these design proposals can usually not directly be adopted for reasons of experimental realizability, they demonstrate the ability of the woodpile structure to act as a host material for various functional defect structures and provide a valuable starting point for the development of customized defect designs compatible with fabrication. Last but not least, consisting of stacked rods, the woodpile structure is a very intuitive geometry and amenable to 2D graphical representation. These points also apply to the introduction of defects therein: Rods, that are discontinued, locally broadened, or distorted, can easily be imagined and graphically displayed.

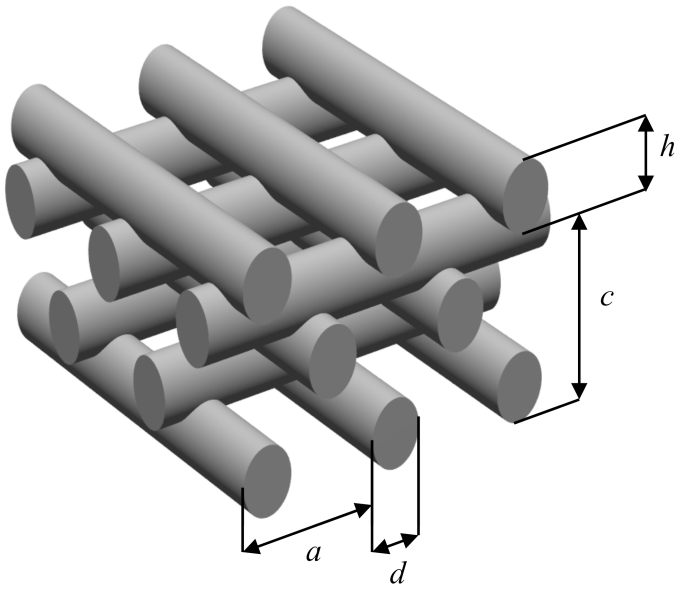

Figure 3.2: Schematical depiction of a portion of a woodpile structure with stacking sequence $ABCDA\cdots$ and $c/a = \sqrt{2}$.

A woodpile structure consists of stacked layers of parallel rods with alternating orthogonal orientations. The center-to-center distance of neighboring rods is denoted by a. Different stacking sequences can be considered. While the most simple one, $ABAB\cdots$, does not support a significant PBG [57], this changes for the sequence $ABCDABCD\cdots$, where C

and D are layers with the same orientation as A and B, respectively, but offset by half a horizontal rod spacing $(a/2)$ as illustrated in Fig 3.2 [56]. The lattice constant in stacking direction is denoted by c. For $c/a = \sqrt{2}$ the lattice has face-centerd cubic (fcc) symmetry, for $c/a = 1$ the lattice has body-centered cubic (bcc) symmetry [57, 67], and for all other values the lattice symmetry is centered-tetragonal (ct). In all cases the basis consists of two perpendicular rods. In Fig. 3.3 woodpiles with different values of the ratio c/a are depicted

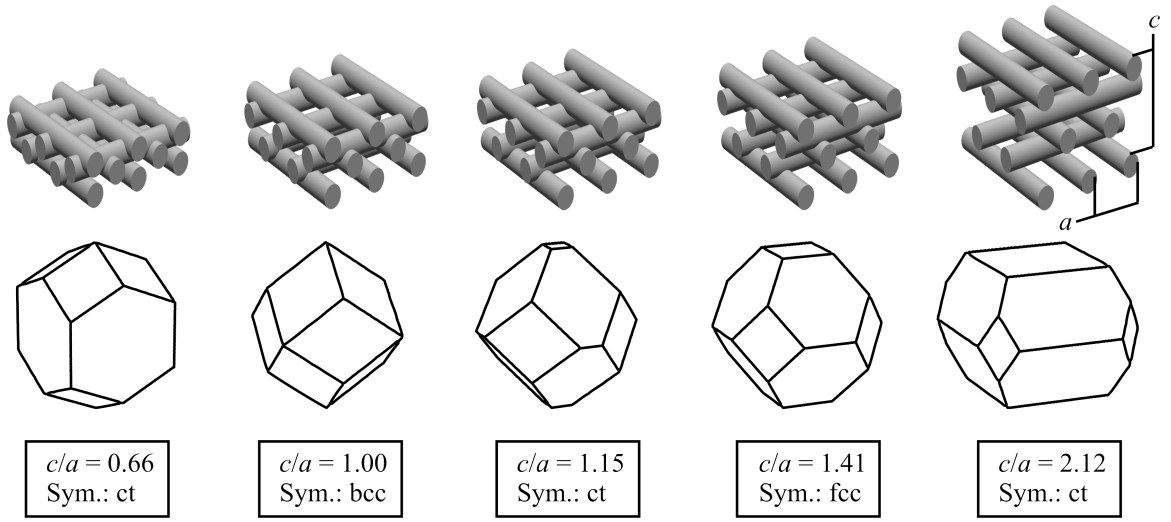

Figure 3.3: Woodpile structures with different values of their ratio c/a, corresponding Brillouin zones, and resulting lattice symmetries.

together with their corresponding Brillouin zones. If c/a is further increased starting from the maximum value shown, the Brillouin zone keeps its structure but it becomes more and more oblate. Similarly, when c/a is further decreased from the depicted minimum value, the Brillouin zone gets increasingly prolate. Most publications on woodpile structures focus on the fcc case, for which the formation of a PBG is possible if the refractive index contrast exceeds a value of 1.9. Particularly, for $\varepsilon = 12.96$ and a filling fraction of 30%, the maximum PBG with gap-midgap ratio of up to 18% is formed in the structure [56]. For comparison, the inverse fcc woodpile structure, for which the dielectric rods in air are replaced by air pores in dielectric, can exhibit a PBG with a gap-midgap ratio as large as 28% for $\varepsilon = 12.96$. Despite the prevalence of the fcc case, the woodpile structure supports a significant PBG also for other values of c/a, as long as the ratio is not increased far above 1.5 or decreased far below 0.8 [56]. The reason for this can be attributed to the shape of the Brillouin zone. As long as the Brillouin zone resembles a sphere, the spatial period is nearly independent of the spatial direction, which is a key property for the formation of a PBG [37], because in this case the stop band for the different directions are more likely to overlap. If, on the other hand, the Brillouin zone becomes significantly oblate or prolate, the stop bands for different directions appear at different spectral positions and a PBG cannot be obtained any more. Figure 3.4 shows exemplary band structures of woodpile structures for the fcc and the bcc case with large PBGs (14.4% and 17.4%, respectively) between the second and the third band in both

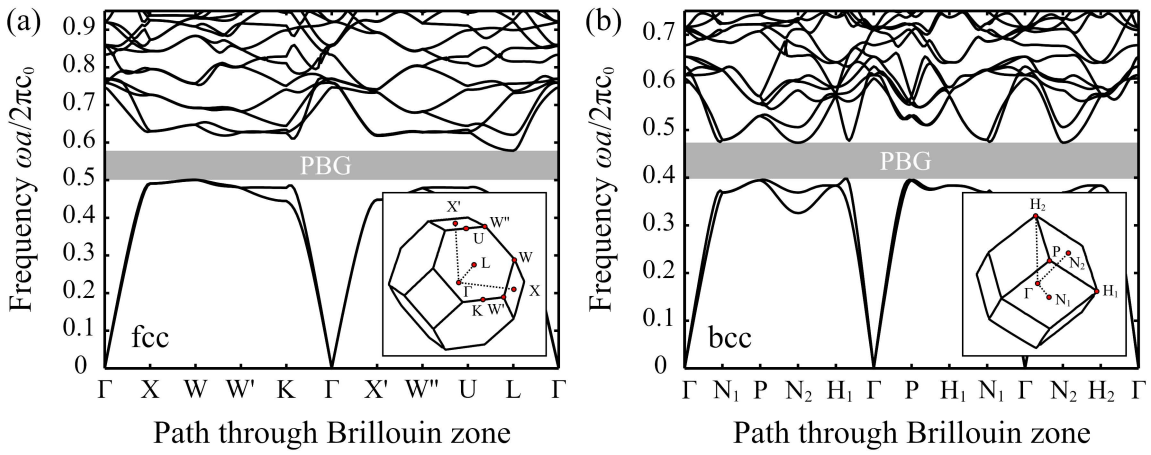

Figure 3.4: Exemplary band structures of (a) a fcc and (b) a bcc woodpile structure. The insets show the respective first Brillouin zones and their characteristic points.

variants. In these calculations, elliptical rod cross sections have been chosen, since this is the relevant case compatible with the experimental fabrication method described in Chapter 4. Changes of the shape of the rod cross section are not critical for the performance of the woodpile structure. In fact, sizable PBGs have equally been demonstrated for rectangular, circular, and elliptical cross sections [56]. In order to form a connected structure, the height h of a rod in stacking direction has to exceed $c/4$. A parameter which is frequently used to describe the cross section of a rod for a given shape is its aspect ratio $\chi = h/d$. The structural parameters used for the band-structure calculations depicted in Fig. 3.4 are $d = 0.25\,a$, $\varepsilon = 11.76$, $\chi = 2$ (fcc), and $\chi = \sqrt{2}$ (bcc). In Chapter 6, fcc and bcc woodpile structures with these parameters and $a = 1\ \mu\mathrm{m}$ will be employed as host model systems for functional defect design.

3.2 Defect Design Proposals for the Woodpile Structure

Over the last years, numerous designs for functional defect elements have been suggested for the woodpile structure as host PBG-material. Aiming at an experimental realization of such elements at optical frequencies, those suggestions providing blueprints for the two most fundamental functional defect structures, namely point defect cavities and straight line-defect waveguides, are of major interest. Focusing on these two elements, this section briefly reviews different defect designs that have been proposed in the literature.

3.2.1 Point Defect Cavities

Point defect cavities in woodpile structures have, for example, been analyzed in [68–72]. An overview over proposed geometries is provided in Fig 3.5. All depicted geometries support

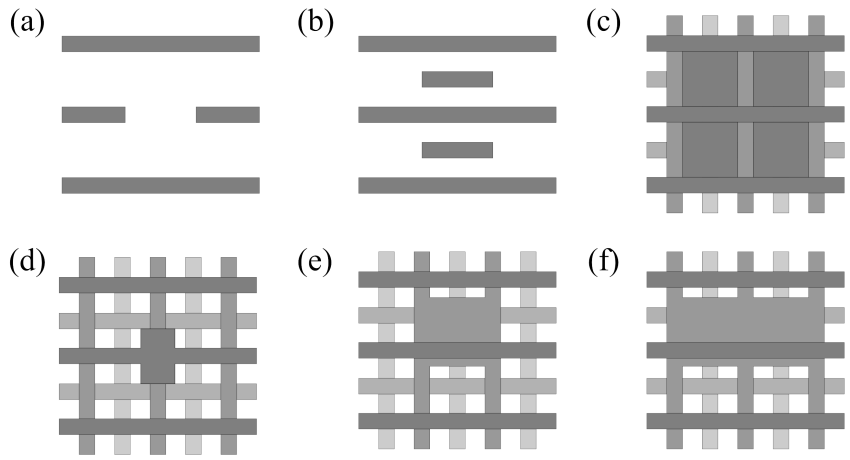

Figure 3.5: Point defect cavity design proposals: (a) Acceptor-type cavity proposed in [68, 70], and (b)–(f) donor-type cavities studied in (b) [68], (c) [69], (d) [71], and (e)–(f) [72].

cavity modes, as evidenced in the respective references by theoretical calculations and/or experimental measurements at GHz or mid-infrared frequencies.

In [68] cavities formed by removing or adding pieces of rods (see Fig 3.5 (a) and (b)) are investigated both theoretically by transfer matrix calculations and experimentally at GHz frequencies. The alignment of the removed or added parts with respect to the adjacent layers is not discussed. For the cavity design shown in Fig 3.5 (a), shifting of the defect mode frequency has been demonstrated by varying the length of the removed segment. For a cavity design similar to that displayed in Fig 3.5 (b), but formed by adding only one additional piece of a rod, no defect-mode transmission along the stacking direction could be observed.
A large dielectric point defect is introduced in [69] by inserting four parallelepipeds in neighboring lattice interstitial sites, as schematically depicted in Fig 3.5 (c). Transmission through the defect mode is measured at GHz frequencies. Furthermore, the transmission level is modulated by illumination of the defect with an external laser.
Arrays of air defect cavities formed by removing sections of length L of several rods, as already shown in Fig 3.5 (a), are investigated experimentally at mid-infrared frequencies in [70].
In [71] the theoretical properties of a donor-type single-defect small-volume cavity are analyzed by use of plane-wave expansion (PWE) and finite-difference time-domain (FDTD) methods. A schematic of the basic cavity design is shown in Fig 3.5 (d). The influence of size, shape and position of the defect cavity on the resonant frequencies of the defect modes, their frequency separations, and their Q-factors is investigated.
This analysis is extended to larger multimode point-defects in [72] using group theory in frequency and time domains. The mode frequency and Q-factor dependence on the cavity size is discussed for two different donor-type cavity designs, which are schematically depicted in Fig 3.5 (e) and (f). Both in [72] and in [71] it is found that the Q-factor dependence on cavity

size, shape and position is rather small, and it is confirmed that Q increases exponentially with the number of stacked stripes.

3.2.2 Line Defect Waveguides

Different designs for straight waveguides in woodpile PhCs are, for example, investigated in [12, 13, 73]. These studies are based on theoretical band structure calculations using the plane-wave expansion method in combination with a supercell technique. A variety of proposed in-plane and out-of-plane geometries is displayed in Fig. 3.6. For all depicted waveguide designs, one or more guided modes are found in the PBG.

The most intuitive acceptor-type in-plane waveguide is formed by removing one rod from one layer as shown in Fig. 3.6 (a) [12, 13]. Less obviously, one can remove a certain part from every single rod as illustrated in Fig. 3.6 (b) [12, 13]. Choosing the position of the re-

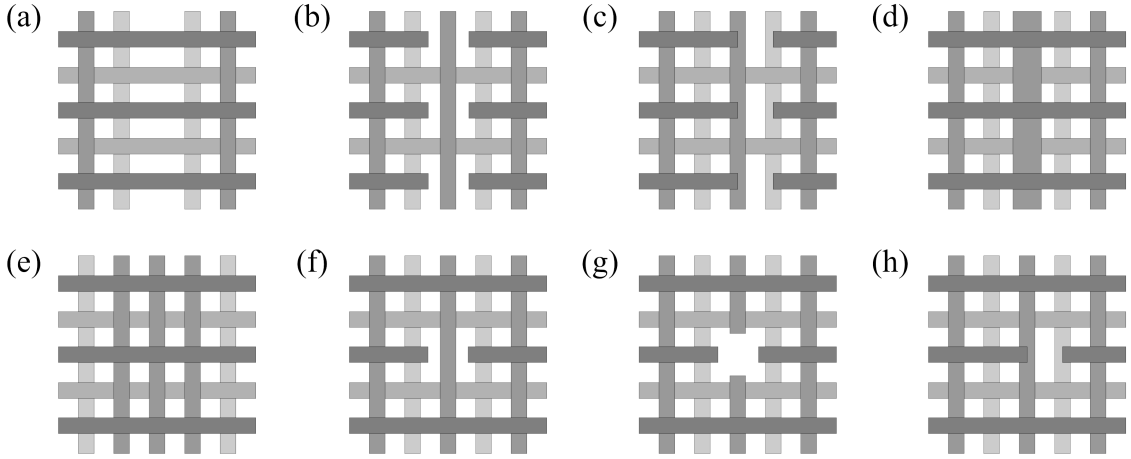

Figure 3.6: Line defect waveguide design proposals: (a)–(c) Acceptor-type in-plane waveguides, adapted from [12, 13]. (d) and (e) Donor-type in-plane waveguides proposed in [73]. (f)–(h) Acceptor-type out-of-plane waveguides, adapted from [13].

moved part with respect to the rods in the adjacent layers as shown in Fig. 3.6 (c) leads to single mode behavior [13].
Various donor-type in-plane waveguides are proposed in [73]. On the one hand, the width of a single rod can be increased as schematically depicted in Fig. 3.6 (d). On the other hand, one or more additional rods can be inserted at different positions of the surrounding PhC. An intuitive example for the introduction of an additional rod is depicted in Fig. 3.6 (e) [73]. More complicated arrangements of additionally inserted rods (not shown) can, *e.g.*, be optimized to obtain a large single-mode bandwidth [73].
Out-of-plane acceptor-type waveguides are investigated in [13], where several possibilities to remove parts of rods in adjacent stacking sequences are explored (see Fig. 3.6 (f), (g), and (h)). The design shown in (g) allows for polarization independent propagation, single-mode behavior is found for the case depicted in (h).

3.2.3 Compound Structures

The full potential of 3D PBG-materials is by far not exploited by donor and acceptor-type point defect cavities and straight waveguides. In fact, many of the advantages offered by the concept do not become evident until more complex structures are considered. Waveguide bends and networks based on the woodpile structure have, for example, been studied in [12, 15, 74], coupling of cavities and waveguides is investigated in [75]. Furthermore, over the last years, numerous sophisticated defect designs for special applications as well as structures with a wide range of different functionalities have been developed. Examples are air-slot cavities with ultrasmall mode volume [76], in-plane compound-defect waveguides optimized for a large single-mode bandwidth [46], channel drop filters [77], beam splitters [74, 78], and coupled-cavity waveguides [79]. Obviously, a wide range of functionalities is provided by defect architectures in woodpile structures. This provides a strong motivation for work aiming at corresponding experimental realizations of such elements at optical frequencies, starting from the most fundamental components as a prerequisite for more complex structures.

3.3 Fabrication Methods

This section provides an overview of different fabrication methods for 3D PhCs operating at optical frequencies, which have been proposed in the literature. The different methods are discussed with respect to their principle suitability to allow for the formation of a PBG and, particularly, for the controlled incorporation of designed defect structures into the bulk PhC material. Actual successful realizations of functional elements in 3D PBG-materials are described in Section 3.4, subsequent to this general survey. A detailed review on defects in 3D PhCs realized before 2006 is provided in [33], which also introduces the differentiation between extrinsic and intrinsic fabrication methods adapted in the following. Extrinsic methods have in common that additional processing steps are required in order to introduce the defect structures into the PhC compared to the fabrication of a PhC without any intentional defects. For intrinsic methods, on the other hand, the number of fabrication steps is identical for defect-free and defect-containing structures.

3.3.1 Intrinsic Methods

Conventional Lithography A very mature technique to process single 2D PhC layers is *conventional lithography*, *e.g.*, e-beam lithography. In order to obtain a 3D PBG-material, however, an additional method has to be applied to stack several of these layers on top of each other. One possibility to do this is by wafer fusion [26, 27], where the single layers are first processed on separate substrates and then bonded to form a 3D structure. Another possibility is to create a 3D PBG-material sequentially on a single substrate by repeated cycles of material deposition, lithography, etching and planarization [28, 29]. A third stacking technique is by micromaniplation (see correspondent paragraph). Methods based on conventional lithography are, independent of the applied stacking technique, very well suited for the

incorporation of defect structures. The defects just have to be taken into account in the design of the respective layers [21, 70, 80–85]. A drawback of this method is the difficulty to stack and precisely align many layers on top of each other, making it extremely time-consuming and leading to a practical limitation of the number of layers that can be fabricated.

Etching Techniques Different etching techniques can be employed to create 3D PhC structures. Using *anodic etching* periodic arrangements of pores can be fabricated in n-type silicon [86]. To this end a substrate, which has been pre-structured with pyramidally shaped holes, is etched with HF-solution while an electric potential is being applied. Due to an increased current density at the tips of the pyramids the etching process is selective and cylindrical pores are formed in the material. The diameter of these pores depends on the irradiation intensity, which is used to control the number of charge carries and thus the solubility of the silicon. Thus, by a variation of the irradiation intensity in time, 3D structures can be accessed, which can support a narrow PBG. In the same manner, planar defects can be created [87]. Line defects can be formed by an appropriate pre-structuring of the substrate [33]. However, the design freedom regarding the host structure as well as the defects is very limited. It is, in particular, not possible to perturb a single lattice site at an arbitrary position. Another etching technique, that has successfully been employed to create PBG-materials, is the *double-angled deep-etching* method [88] based on reactive ion etching (RIE), where the direction of the etching process is controlled by an engineered metal plate that influences the ion-sheath layer. Planar defects can be included extrinsically by wafer bonding [88].
A related RIE technique uses the *Bosch process* [89] to define high aspect-ratio rods in crystalline silicon [90], where a protective polymer layer is applied during RIE in order to avoid side-wall erosion. By etching from different directions, 3D PBG materials can be fabricated [91]. For both of these RIE based approaches, linear and planar defects might be accessible by use of an appropriate etch mask that selectively modifies certain pores compared to those constituting the lattice. This has, however, not been demonstrated yet. Complex arbitrary embedded defects cannot be fabricated using these approaches.

Glancing Angle Deposition *Glancing angle deposition* allows for the large-scale growth of periodically arranged spiral structures [92]. To this purpose a substrate pre-structured with a periodic array of pillars is brought into a collimated gas flow under a large incident angle. Due to self-shadowing the material is only deposited at the tips of the pillars and opposite to the gas flow. By appropriately rotating the sample spiral structures with polygonal footprints are formed. Such structures can possess large PBGs (see Subsection 3.1.1). Planar defects can be introduced by a modulation of the rotation speed [93], line defects are accessible by an according pre-structuring of the substrate [94]. Once again, however, introduction of a single point defect at a defined position is an unresolved problem.

Autocloning *Autocloning* is a technique, where alternating layers of two materials are deposited on a patterned substrate by sputtering and sputter-etching at the same time [95]. Conditions are chosen such that a periodic modulation is preserved. Defects can be intro-

duced by locally changing the periodicity of the substrate pattern or by changing the layer thickness. 3D PhCs [95], heterostructures [96], and line defects [97] have been fabricated using this method. However, these PhCs do not exhibit a PBG and the controlled perturbation of a single lattice site is not possible by autocloning.

Micromanipulation Small building blocks like, *e.g.*, colloidal particles [98] or entire 2D PhC layers [30], can be assembled to 3D structures using *micromanipulation* [99]. This method provides a high level of flexibility regarding defect fabrication. Perturbations can be introduced either in the building blocks themselves [50, 100, 101] or during their assembly through an appropriate placement of selected building blocks [33]. However, this method is very slow, severely restricting the size of the 3D PhC structures that can be fabricated.

Direct Write Approaches In *direct write* approaches, a 3D computer-aided design is converted into a target material *via* a suitable process. For PhC structures with operating wavelengths in the optical regime *robotic ink writing* (RIW) [102] and *direct laser writing* (DLW) [23, 103] have successfully been employed. RIW uses an engineered polyelectrolyte ink, that is extruded through a small orifice. In this way, cylindrical filaments are obtained, which can be arranged to form, *e.g.*, a woodpile PhC using a proper computer control.
DLW — which is the technique employed in this thesis — is described in detail in Section 4.1.
For both direct write techniques the dielectric contrast of the written structures is usually not sufficiently high to achieve a 3D PBG, which is due to the typically relatively low refractive index values of the ink or the photoresist, respectively. The obtained structures can, however, be used as templates for inversion processes into high index PBG-materials [24, 25, 102]. For templates fabricated by DLW, two such processes for inversion into silicon are described in Section 4.2. Defects compatible with the respective process can be introduced into these structures at arbitrary positions by an appropriate modification of the computer design [33]. Comparing the two direct write techniques, DLW offers a larger degree of design freedom than RIW, since writing through or inside already exposed parts of a structure is possible, while for RIW writing of additional features is limited to physically accessible parts of the structure.

3.3.2 Extrinsic Methods

Holographic Lithography The concept of *holographic lithography* for the fabrication of 3D PhCs consists of recording the hologram created by interference of multiple beams of light into a photoresist [63]. A related approach is to use a phase mask or similar diffractive optical element to achieve the hologram [104, 105]. Since the refractice index of the photoresist is too small to allow for bandgap formation, replication of the resulting photoresist template with high-index materials is essential. Defect structures can be added to the 3D periodic structure before development of the resist using DLW and an alignment procedure [106, 107]. An intrinsic method to add defect structures is by combining the diffracting

optical element responsible for the formation of the 3D interference pattern with an amplitude mask [105]. In the latter case, however, the design freedom is extremely limited and fabrication of embedded features seems impossible.

LIGA *LIGA*, which stands for the German acronym *Lithographie, Galvanik und Abformung*, employs synchrotron-based deep X-rays to expose a photoresist through an absorber mask [108]. Using multiple exposures under different incident angles, 3D templates can be obtained, which can then, in the next step, be infiltrated with a high-index material. Defects can be introduced into these structures *via* multiple exposures and multilayer resist approaches [109]. However, uniformity issues and the fact that synchrotron radiation is required limit the general applicability of this approach [33].

Colloidal Self-Assembly A widespread approach for the fabrication of 3D PhCs is *colloidal self-assembly*. Typical samples consist of monodisperse silica or polystyrene microspheres with diameters ranging from $200\,\mathrm{nm}$ to $2\,\mu\mathrm{m}$, arranged in a fcc lattice [110]. An advantage of this method is that thick structures covering large areas can be obtained. However, unintentional defects like cracks are an issue. Inversion of such structures into a high-index material [111] leads to inverse opal structures supporting a PBG (see Subsection 3.1.1) between the eighth and the ninth band. An obvious technique to introduce defect structures into colloidal PhCs is by substitutional doping of the colloidal suspension. In this way a 3D PhC with randomly placed intrinsic impurities results [112].
Extrinsic methods, which allow for a controlled placement of defects in colloidal PhCs, employ multiple fabrication steps. Most of them are based on the following principle: First, a colloidal 3D PhC is grown. Next, a layer of material is deposited onto its surface, which may or may not be processed in an additional step (e.g., by electron-beam or nano-imprint lithography). Finally, a second 3D PhC is grown on top of this layer [113, 114]. Another method combines colloidal self-assembly with DLW. In this case the 3D PhC is infiltrated with a photoresist and defect structures are written into the resist [115]. The resulting composite structure can then be inverted into a high-index material, leading to an inverse opal with embedded air defects [20].

In this thesis, the approach based on DLW and silicon inversion has been chosen for fabricating functional elements in PBG-materials. This approach stands out by its ability to create high-quality PBG structures, and, at the same time, allow for the precise and controlled introduction of designed defect structures at arbitrary positions. Furthermore, this approach is comparably fast and inexpensive, and the fabrication of many layers (> 20) can routinely be accomplished. The experimental details of DLW and inversion are discussed in Chapter 4.

3.4 Functional Experimental Realizations: State of the Art

In the following different examples of defect fabrication using the above discussed methods are briefly reviewed. Following a general overview, special attention is paid to experimental realizations of point defect cavities and straight line defect waveguides embedded into PBG-materials, which include an optical characterization of the fabricated samples.
Planar defects have been realized by numerous methods and have also been optically characterized many times. Some examples are: [116, 117] (DLW), [93] (GLAD), [30] (micromanipulation), [113] (colloidal self-assembly), and [87] (anodic etching).
In contrast, most publications on line or point defects merely provide a fabrication proof-of-principle. Examples are [117] (DLW), [109] (LIGA), [115] (Colloidal self-assembly with DLW), [33] (RIW), and [106, 107] (holographic lithography with DLW).
Another group of publications on point or line defects shows measured spectra and can identify defect signatures therein, however, the PhCs that serve as host structures for the point or line defects do not support a PBG. Examples are [114] (colloidal self-assembly with extrinsic line defect), and [112] (colloidal self-assembly with intrinsic point defects).
A category of their own are the defect cavities presented in [84], that are defined at the surface of an eight layer PBG GaAs woodpile structure with PBG in the telecom wavelength regime. These structures are fabricated by conventional lithography and wafer bonding. Radiation spectra from surface-defect modes reveal sharp peaks in the PBG, from which high Q-factors up to approx. $9,000$ are estimated. However, these cavities are not embedded inside the 3D PBG material, such that they are not capable of fully exploiting the potential offered by the concept of PBG-materials, regarding, *e.g.*, 3D integration of functional elements.

3.4.1 Point Defect Cavities in Photonic Bandgap Materials

Point defect cavities embedded into 3D PBG materials for NIR frequencies have been optically characterized in Refs. [50, 80, 81, 83, 85, 100, 101].
Most of these experimental realizations rely on embedding active materials like quantum wells or quantum dots into the cavities in order to obtain detectable signals from the cavity modes.
In [80] conventional lithography and wafer fusion are applied to fabricate nine layers of woodpile 3D PBG-material made of GaAs with embedded donor-type point defect cavities of different sizes, where the smallest cavity is based on the design shown in Fig. 3.5 (d). Within the defect layer, the structures contain InGaAsP-quantum-well layers emitting at $1.55\,\mu\mathrm{m}$. The emission frequency coincides with the position of the PBG. Photoluminescence (PL) spectra are measured for the different cavities. From the defect signatures Q-factors of approx. 100 are derived. In addition, micro-PL mapping is performed, showing that emission in resonance with the defect mode is observed only from the defect region. In [83] basically the same system is investigated, only that the number of layers is increased to 17. This leads to improved Q-factors around 350.
[100] also relies on light emitters placed inside point defect cavities based on the design shown in Fig. 3.5 (d). In this case, InAsSb quantum dots (QDs) emitting in the $1.5 - \mu\mathrm{m}$

range are coupled to 3D PhC nanocavities. Woodpiles with 17 layers made of GaAs are used as a host PBG-material. The structures are fabricated by a combination of micromanipulation with conventional lithography. In this way, rather small ($< 10\,\mu\mathrm{m}$ structured diameter) but high-quality structures are obtained. PL spectra are collected for different numbers of layers placed around the defect. Clear peaks corresponding to the modes supported by the cavity can be observed. From these peaks a maximum experimental Q-factor of $2,300$ is calculated. In [101] these structures are optimized by changing the size of the defect cavity and increasing the number of stacked layers to 25, leading to a Q-factor of more than $8,600$. By further optimizing the size of the defect cavity, the so far highest Q-factor for point defect cavities in 3D PBG-materials has been realized, reaching a value of over $10,000$ [50].

For point defect cavities that do not include emitters, the measured Q-values are much smaller. In [81] the host 3D PBG-material for the inclusion of defect structures is formed by alternately stacking two types of 2D silicon PhC slabs by sequential conventional lithography. Seven functional layers are fabricated in total and dielectric point defects are introduced in one layer of the structure. In order to enhance the defect signature, many nominally identical point defects are distributed in a non-periodical manner over the defect layer. Transmittance and reflectance spectra are measured with a Fourier-transform infrared microscope-spectrometer, revealing defect signatures around telecommunication wavelengths. The experimental Q-value is calculated to be 18.
In [85] arrays of large cavities inside silicon woodpile structures operating at near-visible frequencies are presented. The structures are again fabricated by sequential conventional lithography. The cavities are formed by adding many closely spaced pieces of rods similar to the design shown in Fig. 3.5 (b). The obtained Q-factor of about 30 is not only limited by the design and structural imperfections, but is additionally influenced by absorption of the silicon at these wavelengths.

Generally, the comparably low Q-factors observed for embedded passive 3D PBG point defect cavities are a conceptual problem. The reason for this is that, in order to obtain a measurable defect signature, the defect density has to be made very high and/or the number of lattice constants surrounding the cavity has to be made very small. Both possibilities have negative impact on the Q-value of the cavities. Furthermore, if the defect density is chosen too high, coupling effects may become dominant, such that actually extended states instead of localized point defect cavity states are investigated.
Cavity structures in PBG materials designed and fabricated in the course of this thesis are presented in Chapter 6. As the PBG-materials fabricated and investigated in this thesis are based on silicon as a high-index material, that is, a passive medium, the above mentioned issues have to be kept in mind. Compared to point defect cavities, more pronounced defect signatures are expected for PBG-based waveguides in passive materials, without the need to artificially and drastically deteriorate their optical properties. Regarding an experimental optical characterization, the focus of this thesis has therefore been laid on waveguide structures, which are the topic of the following subsection.

3.4.2 Line Defect Waveguides in Photonic Bandgap Materials

Only extremely few publications report on the optical characterization of line defect waveguides in 3D PBG materials for optical wavelengths [20, 21, 82]. In [20] colloidal self-assembly is used in combination with DLW followed by silicon inversion to fabricate air-defect channels with two 90 degree bends in inverse opals. Spectra are not shown but transmission through the channels is imaged using light with wavelengths in the PBG. In [82] nine layers of silicon woodpile PhC with a PBG in the $1.55\ \mu\mathrm{m}$ wavelength region containing dielectric-defect waveguides are fabricated by conventional lithography in combination with wafer fusion. An optical characterization is performed by shining a laser at the edge of the waveguide and at the same time observing the near-field image produced by the sample directly with an infrared camera from above the waveguide. In this way light could be observed propagating into the 3D PhC. Once again, however, spectra are not shown, and light, which has propagated *through* the waveguide, is not detected. Finally, the same fabrication method is applied in [21] to create vertical and L-shaped acceptor-type defect waveguides embedded into silicon woodpiles with up to nine layers and a PBG in the telecom regime. Transmission spectra, which allow for the identification of the guided mode, are recorded using a tunable laser and an InGaAs photodiode. However, no calibrated data are presented for the transmittance, such that the performance of these waveguides remains unclear.
Line defect waveguides in 3D PBG silicon woodpile structures designed and fabricated in the course of this thesis are presented in Chapter 6. In the same chapter, the potential of DLW and silicon inversion to integrate many different defect elements in one single woodpile structure is experimentally demonstrated. Light propagation through vertical waveguide structures is investigated in Chapter 7. Compared to the structures discussed in [21] the number of woodpile lattice constants is more than doubled and calibrated reflectance and transmittance spectra are recorded. Furthermore, an experimental route to tune the waveguide mode to a desired spectral position is explored.

Chapter 4

Methods

This chapter is dedicated to the experimental and numerical methods employed in this thesis. The first part deals with the fabrication of 3D PBG-materials, starting with direct laser writing (DLW). DLW can be seen as the 3D analogue of conventional 2D laser or electron beam lithography and is used here to fabricate 3D polymer templates, which can subsequently be transferred into high index-contrast materials. For this transfer, which is the topic of the second part of this chapter, deposition techniques compatible with 3D fabrication are needed. Such techniques are atomic layer deposition (ALD) and chemical vapor deposition (CVD), which play a similar role in the 3D case as evaporation or sputter techniques do for 2D fabrication. Here, the specific processes used in this thesis, silica ALD and silicon CVD, are described and it is shown how they can be combined to obtain 3D PhCs with large PBGs. The third part of this chapter describes the optical characterization of the fabricated samples with a Fourier-transform infrared microscope-spectrometer. Finally, in the last part of this chapter, the calculation techniques used to compute band structures and theoretical reflectance and transmittance spectra of 3D PhCs are described, namely the plane-wave expansion method and the scattering-matrix technique.

4.1 Direct Laser Writing

4.1.1 Functional Principle

Direct laser writing (DLW), which has been presented for the first time by S. Maruo *et al* [22] in 1997, is an inherently 3D lithography technique that allows for the fabrication of almost arbitrary 3D submicron structures. The potential of this technique regarding the fabrication of 3D PhCs and other photonic structures has soon been recognized, resulting in the experimental realization of, *e.g.*, woodpile PhCs [23, 103], chiral PhCs [118], 3D quasicrystals [119], 3D metamaterials [120, 121], and invisibility carpet cloaks [122] based on this technique. A recent review on 3D photonic nanostructures fabricated by DLW is provided by [123].

The basic idea of DLW is that the solubility of a photoresist for an appropriate developer is changed locally through a physical process or chemical reaction upon illumination with a

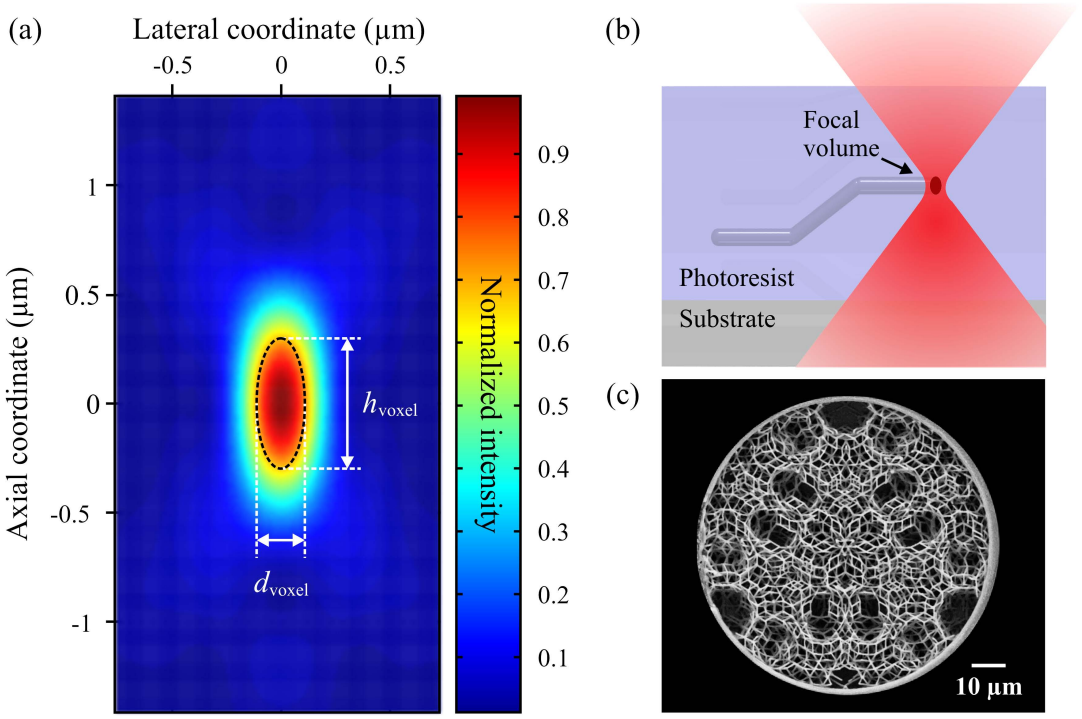

Figure 4.1: (a) Iso-intensity map of the focal region plotted over axial and lateral coordinates. If the black dashed line corresponds to the polymerization threshold, one obtains an ellipsoidal voxel as a basic building block for DLW structures. Calculation: J. Fischer. (b) A laser beam is tightly focused into a photoresist, polymerizing it in the focal volume. Scanning the sample relative to the focal spot provides the desired 3D writing capability. (c) Example for a sophisticated 3D structure fabricated by DLW, a rhombicuboctahedral photonic quasicrystal (taken from [124] with permission from A. Ledermann).

laser beam. DLW, as it is used in this thesis, is based on a nonlinear optical process, namely multi-photon absorption. In this process, two (or more) photons are absorbed simultaneously, thereby exciting a photoinitiator molecule in the photoresist from an initial to an energetically higher electronic state. The energy difference between the two electronic states is equal to the sum of the energies of the photons. In the case of degenerate two-photon absorption, *i.e.*, when two photons with the same wavelength are absorbed at the same time, the strength of absorption is proportional to the square of the light intensity at this wavelength. It is furthermore proportional to the imaginary part of the third order dielectric susceptibility [125], which is several orders of magnitude smaller than its linear counterpart. Therefore, to run the two-photon absorption process at a reasonable reaction rate, very high light intensities are required, which can be provided by tightly focused laser beams. Pulsed laser sources are preferably utilized because they allow for high peak intensities at relatively low average energies, thus preserving the photoresist from thermal destruction.

In order to create a situation where the two-photon absorption process dominates over linear absorption, the photoresist and the laser wavelength λ have to be adjusted such that the resist is transparent at λ and absorbing at $\lambda/2$. If this is the case, and the intensity exceeds a cer-

tain threshold value needed to provoke the reaction responsible for the solubility change, the resist can be exposed *via* two-photon absorption. The intensity can now be chosen such that the exposure threshold intensity is only reached locally in the very focal volume of the laser beam. This volume element, the so-called "voxel", is the basic building block of all structures fabricated by DLW. Its ellipsoidal shape is defined by the geometry of the iso-intensity surfaces in the focal region. Such an iso-intensity map calculated by vectorial Debye-theory is depicted in Fig. 4.1 (a) for parameters $NA = 1.4$, circular polarization, $800\,\mathrm{nm}$ wavelength, and a refractive index of the photoresist of 1.52. If the black dashed line in Fig. 4.1 (a) is the exposure threshold, the resulting voxel is rotationally symmetric with respect to the optical axis and has an aspect ratio $\chi_{\mathrm{voxel}} = h_{\mathrm{voxel}}/d_{\mathrm{voxel}}$ of approximately 2.7, where d_{voxel} is the lateral width of the voxel and h_{voxel} is its dimension in direction of the optical axis. If the sample is now scanned with respect to the position of the laser focus, an arbitrary 3D trajectory can be written into the resist as illustrated in Fig. 4.1 (b), which is then transformed into a real 3D photoresist structure by development. Using standard DLW, feature sizes around $200\,\mathrm{nm}$ and structures with lattice constants around $1\,\mu\mathrm{m}$ are routinely obtained. Owing to the high flexibility of the method, even very sophisticated 3D structures are accessible, as for example the rhombicuboctahedral quasicrystal [124, 126] depicted in Fig. 4.1 (c).
In principle, DLW can also be accomplished by single photon absorption [127, 128]. Again the intensity is chosen such that a given exposure threshold, now based on a linear physical or chemical process, is reached only within the focal volume of the writing laser, thus providing a 3D resolution. However, the advantage of a non-linear process becomes obvious when writing complex 3D structures instead of isolated features, where, for a linear process, the effective resolution of the writing result is severely limited by the proximity effect. This effect describes the accumulation of exposure dose in time at positions, where the initial intensity has not been sufficiently high to expose the resist, thereby leading to an unwanted exposure of the resist between neighboring features. In the non-linear case, on the other hand, owing to the quadratic dependence of the two-photon absorption strength on the intensity, the proximity effect is significantly reduced, resulting in the capability to write even complex 3D architectures with closely spaced features.

4.1.2 Photoresists

For the fabrication of high-quality polymer templates for 3D PBG-materials by DLW, the choice of the employed photoresist is a crucial success factor. This choice depends both on the geometry and on the requested feature sizes of the structure to be realized. In this thesis, two different commercially available photoresists have been used for this purpose, the widely-used DLW resist SU-8 and the novel resist IP-L. Their specific properties and application areas are discussed in the following.

SU-8

The photoresist NANO™ SU-8 (MicroChem Corp.) is a negative-tone photoresist that relies on cationic polymerization [129, 130]. Unexposed SU-8 has on average eight epoxy groups

per monomer, enabling high cross-linking and thus a high chemical and mechanical stability of polymerized SU-8. Triarylsulfonium hexafluoroantimonate salts are used as cationic photoacid generator. Upon illumination the salts are decomposed and a strong acid is formed, which in turn acts as a catalyst for a spatially defined chain-growth polymerization. Since the polymerization reaction is very slow at room temperature, a thermal post-exposure treatment is usually necessary for SU-8. The advantage of this rather complicated exposure mechanism is that the refractive-index change between exposed and unexposed regions is at first very small, on the order of $\Delta n \approx 5 \cdot 10^{-4}$ [131]. This is favorable for DLW since the writing result is hardly influenced by scattering on already exposed regions.

SU-8 can be purchased in different concentrations of its solid constituents contained in a solvent. In this thesis, SU-8 25 is used corresponding to 63% of solid constituents by weight. For DLW the SU-8 is processed as follows: Films with a thickness of approx. $20\,\mu\mathrm{m}$ are obtained by spin-coating SU-8 25 first for $10\,\mathrm{s}$ at $600\,\mathrm{rpm}$ and subsequently for $30\,\mathrm{s}$ at $3,300\,\mathrm{rpm}$ on conventional $22\,\mathrm{mm} \times 22\,\mathrm{mm} \times 170\,\mu\mathrm{m}$ microscope cover slides. These films are then subjected to a pre-exposure bake for $1\,\mathrm{h}$ at $60°\mathrm{C}$ in a convection oven to evaporate the solvent. This procedure results in solid films of SU-8, which can then be exposed by DLW. After illumination, a post-exposure bake is performed where the temperature in the convection oven is ramped from $60°\mathrm{C}$ to $90°\mathrm{C}$ in $7\,\mathrm{min}$ to accelerate the polymerization reaction. The sample is then developped for $10\,\mathrm{min}$ using the developper mr-600 (MicroChem Corp.). Finally, the sample is rinsed with isopropanol and dried in a flow of nitrogen.

Since unexposed SU-8 is already a solid material, structures written into this resist do not need to be mechanically stable or connected during the writing process itself, only the completely written structures have to meet these criteria. This is, for example, essential for structures like the 3D quasicrystal depicted in Fig. 4.1 (c). Furthermore, owing to the possibility to temporarily define “flying features”, woodpile structures can be exposed “top down”, starting from its topmost layer and working towards the substrate, thus avoiding to focus the laser through already exposed regions.
However, bulk SU-8 has a granular character with grain sizes of approx. $20\,\mathrm{nm}$, giving rise to surface roughness of the nanostructures on the same scale [106]. Furthermore, polymer shrinkage effects, which occur after development, are an issue. The degree of shrinkage depends on many factors, like the employed writing laser and the feature sizes of the written structures.

IP-L

The photoresist IP-L (Nanoscribe GmbH) is a liquid negative-tone photoresist that relies on radical polymerization [132]. Upon laser excitation, radicals are formed which break the bonds of the monomers, thereby initiating a chain-growth reaction. In contrast to SU-8, this reaction takes place immediately and no thermal post-treatment has to be performed. Generally, no pre- or post-processing at all is required for IP-L. For the writing process, a drop of IP-L is cast on a standard $22\,\mathrm{mm} \times 22\,\mathrm{mm} \times 170\,\mu\mathrm{m}$ microscope cover slide, which is then

directly inserted into the DLW setup. After exposure, the sample is immersed for $10\,\mathrm{min}$ into isopropanol where the unpolymerized IP-L is dissolved. If necessary, the sample can be rinsed with acetone in addition to the development step in order to remove any remnants of unpolymerized resist. Finally the sample is dried in a flow of nitrogen.

IP-L allows for small feature sizes and shows very little proximity effect. Furthermore, the obtained structures have a very smooth surface. Altogether, these properties of IP-L have led to a breakthrough in the realization of structures with smaller feature sizes as reported in Chapter 5 of this thesis. However, since IP-L is a liquid resist, the written structures have to be mechanically stable and connected at every time of the writing process. Woodpile structures therefore have to be written "bottom-up", that is, starting from the substrate and literally stacking the layers on top of each other, thereby focusing the laser through the already written layers. Furthermore, since the refractive index change between exposed and unexposed IP-L is much larger ($\Delta n \approx 0.04$ [133]) than for SU-8, the writing result is affected by the presence of previously exposed parts of the structure. Therefore, in order to obtain a uniform rod thickness even for a large number of stacked layers, a gradient of the writing laser power has to be applied, such that the lower layers are written with less power than the upper layers. As for SU-8, polymer shrinkage effects do occur for IP-L, however, the degree of shrinkage has been observed to be typically lower under the same writing conditions.

4.1.3 Experimental Setups

The functional principle of DLW has already been described in Subsection 4.1.1. In order to provide the required functionalities mentioned there, several essential components have to be included in any efficient DLW system. These components are a suitable writing laser, a possibility to adjust the laser power, focusing optics to tightly focus the laser beam into the photoresist, a 3D scanning stage to move the resist with respect to the focal point and, finally, a technique to find the position of the interface between the resist and the glass substrate. In the course of this thesis, two different setups implementing these basic requirements in slightly different ways have been used for DLW of PhC polymer templates.

Setup 1

The first setup is a home-built setup based on an earlier version by M. Deubel [106], which has been newly assembled and modified for automated operation in the course of this thesis. It is schematically depicted in Fig. 4.2. The laser source is a regeneratively amplified Ti:Sapphire laser system (Spectra Physics Hurricane), which produces pulses with approx. $120\,\mathrm{fs}$ pulse length at a central wavelength of $800\,\mathrm{nm}$. The laser output is linearly polarized and has a maximum power of approximately $1\,\mathrm{W}$. Out-coupling from the laser resonator is controlled by the so-called synchronous delay generator **SDG**, which allows tuning of the repetition rate from $1\,\mathrm{kHz}$ to single shot operation using Pockels cells. After leaving the laser resonator, the beam first impinges onto beam splitter **BS1**, where 99% of its intensity are transmitted and only 1% is reflected. The transmitted part is attenuated and

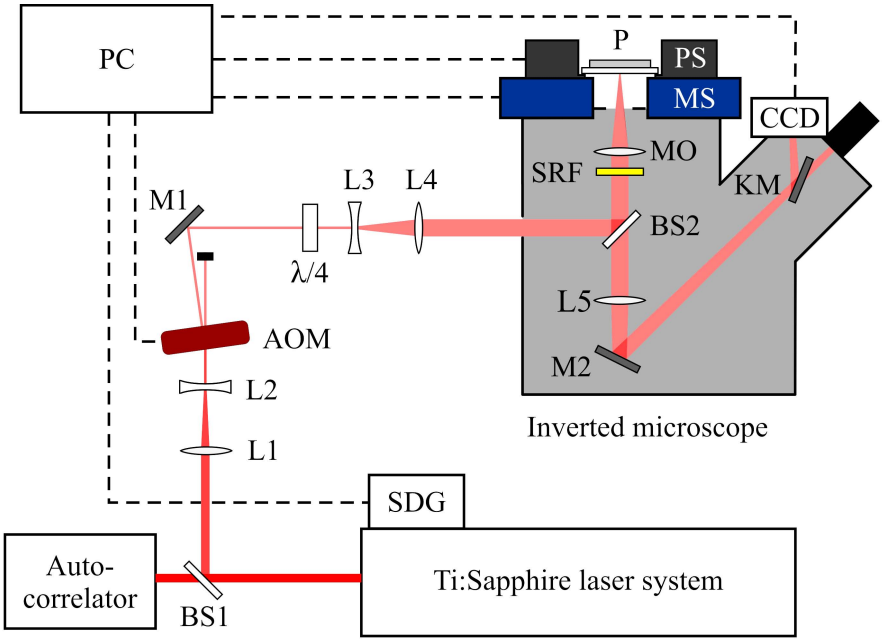

Figure 4.2: Schematical depiction of the home-built Setup 1 used for DLW.

directed into an autocorrelator, in order to optimize the autocorrelation of the pulses by use of the external puls compressor of the laser system (not shown). The reflected part is directed into the actual DLW setup, where first its beam diameter is reduced from approx. $6\,\mathrm{mm}$ to approx. $1\,\mathrm{mm}$ by a combination of two lenses **L1** and **L2**. This is necessary in order to couple the beam into the entrance aperture of an acousto-optical modulator **AOM** (Pegasus Optik GmbH) which is used to adjust the laser power in the DLW process. The beam then passes a $\lambda/4$-waveplate, which transforms the linearly polarized laser output into circularly polarized light, for which the obtained voxel element is rotationally symmetric with respect to the optical axis, while for linear polarized light, it is slightly elongated in one lateral direction [106]. Afterwards, the beam is expanded again to a diameter of approx. $12\,\mathrm{mm}$ by use of the two lenses **L3** and **L4** and coupled into an inverted microscope (Leica DR-IRM). Inside the microscope it impinges onto another beam splitter **BS2**. The reflected part passes through a shaded ring filter **SRF**, which reduces the aspect ratio of the voxel element in SU-8 from 2.7 to approximately 2.0 [124]. The beam is then focused into the photoresist sample by the microscope objective **MO** (Leica HCX PL APO $100\times$/0.7 - 1.4 CS) which is used at its maximum numerical aperture ($NA = 1.4$). The photoresist samples are prepared as described in Subsection 4.1.2 and mounted onto a 3D piezo scanning stage **PS** (Physik Instrumente P-527.3 CL) with a scanning volume of $200\,\mu\mathrm{m} \times 200\,\mu\mathrm{m} \times 20\,\mu\mathrm{m}$. In order to enlarge the effective scanning volume of the piezo stage by using the actual scanning volume multiple times for DLW, the piezo scanning stage is in turn mounted on a 2D motorized scan-

ning stage **MS** (Märzhäuser, C9712-9012K, Vexta Stepping Motor, Wetzlar), which is used to shift the sample with respect to the focus position in steps of several hundreds of micrometers perpendicular to the optical axis. The electronic control units of the piezo scanning stage and the AOM are controlled by an analog 16 bit output board (National Instruments NI PCI-6229), the motorized stage by a PCI card. Both the output board and the PCI card are connected to a computer, thus allowing for a complete automation of the actual writing process *via* a dedicated LabVIEW program provided by Nanoscribe GmbH. Solely the position of the interface between the glass of the cover slide and the photoresist has to be determined and adjusted manually. To this purpose the alternative beam path at the beam splitter **BS2** is used. An image of the sample is produced by the tube lens **L5**. Depending on the position of the kinematic mirror **KM**, it can be observed either directly through the eyepiece of the microscope or with a CCD camera on a computer monitor. For observation, the sample is illuminated with a halogen lamp (not shown), whose short wavelength spectral emission is supressed by a filter to avoid an exposure of the resist. In order to find the glass-photoresist interface, the laser power is chosen sufficiently high to locally create a plasma in the resist, but not in the glass. By scanning over the interface and observing the onset of plasma creation with the CCD camera, the position of the interface can be determined.

Setup 2

The second DLW setup used for the fabrication of polymer templates is the commercially available instrument "Photonic Professional" from Nanoscribe GmbH.
Fig. 4.3 shows a sketch of its beam path (a) and a photograph of the system (b). In principle, this system is very similar to System 1 and its components are therefore not again described in detail here. However, there are some differences, the most important of which are pointed out in the following:

- This instrument uses a different laser source, namely a compact frequency doubled erbium-doped fiber laser with sub-$150\,\mathrm{fs}$ pulses at a repetition rate of $100\,\mathrm{MHz}$ and a central wavelength of $780\,\mathrm{nm}$. The maximum laser power is approx. $65\,\mathrm{mW}$.

- A shaded ring filter is not included in this setup, the resulting voxel therefore has an aspect ratio of about 2.7 for the photoresists employed.

- The scanning volume of the piezo stage is larger, namely
  $300\,\mu\mathrm{m} \times 300\,\mu\mathrm{m} \times 300\,\mu\mathrm{m}$. The effective writable volume is, however, reduced to $300\,\mu\mathrm{m} \times 300\,\mu\mathrm{m} \times 170\,\mu\mathrm{m}$ by the working distance of the microscope objective used for focusing the laser.

- The system comes with an automatic interface finder and a computer controlled microscope z-drive, thus leading to a completely automated writing process, including the adjustment of the glass-photoresist interface position. In combination with the motorized stage (not shown), large sample areas or multiple samples can be written without any manual interaction.

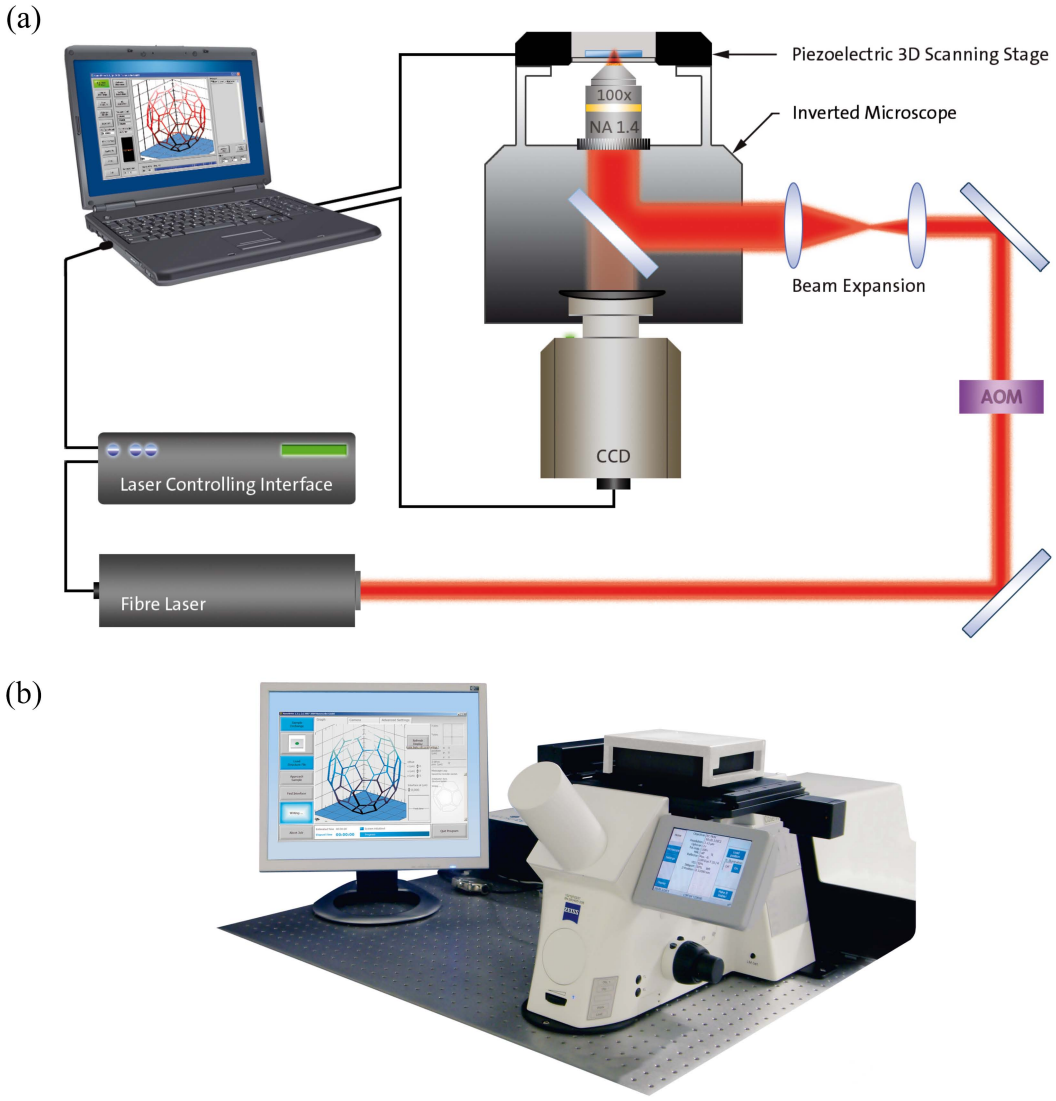

Figure 4.3: (a) Scheme of a DLW setup as implemented by the Nanoscribe Photonic Professional instrument. b) Photograph of the commercially available system. Both images: Courtesy of Nanoscribe GmbH.

For both setups the DLW is operated in "Fast Writing Mode", where the laser output is switched on continuously while the piezo stage is scanning interconnected parts of the photonic nanostructure. These interconnected parts are expressed as sequences of 3D coordinate points with corresponding laser power values and imported into the writing software as ASCII files. Typical writing speeds lie between $50\,\mu\mathrm{m/s}$ and $250\,\mu\mathrm{m/s}$.
In the course of this thesis, Setup 1 is used in combination with the photoresist SU-8 only [123, 126], while Setup 2 is used both with SU-8 as well as with IP-L [134, 135]. In the latter case, for the structures written into IP-L a higher structural quality is obtained.

4.2 Silicon Replication and Inversion

In Chapter 3 it is stated that PBG-materials require high index contrasts. However, polymerized SU-8 has a refractive index of only $n \approx 1.59$ at $\lambda = 1.5\,\mu\mathrm{m}$, polymerized IP-L even less with $n \approx 1.52$ [122] in a range from $\lambda = 1.4\,\mu\mathrm{m}$ to $\lambda = 2.7\,\mu\mathrm{m}$. Up to now, no 3D geometry is known for which an index contrast of 1.59 is sufficiently high to open up a 3D PBG. For the particular case of a woodpile structure with optimized parameters, an index contrast of at least 1.9 is needed for PBG formation [56]. Even if PBGs can therefore not be found in polymer woodpile structures obtained by DLW, these structures can still serve as *templates* for PBG-material fabrication. In order to increase their index contrast they can be transferred into silicon structures. Amorphous silicon has a high refractive index of 3.72 at $1.55\,\mu\mathrm{m}$, which allows for the formation of large PBGs in various 3D geometries (see Section 3.1). This value for the refractive index of amorphous silicon has been determined by F. Peiris (Kenyon College) using ellipsometry measurements on silicon films deposited on a glass substrate with the same system described in Subsection 4.2.2 which is used later on to fabricate PBG-materials. Detailed results of these measurements are included in Appendix A.

Two different techniques, which are described in this section, are available to accomplish the transfer from a polymer into a silicon structure, namely silicon double inversion (SDI) [24] and silicon single inversion (SSI) [25]. In the case of SDI, a silicon replica of the polymer structure is created while an SSI procedure results in an inverse silicon structure. Therefore, by use of these two techniques a large number of direct as well as inverse PBG-geometries becomes experimentally accessible (see Section 3.1). For example, a silicon woodpile structure can be obtained from a woodpile photoresist template by an SDI procedure [24], while an inverse silicon woodpile can be obtained from an identical template by SSI [25].
Both techniques employ an intermediate step, where amorphous silica is deposited inside the structure. The next subsection deals with this deposition process. Following this, the deposition process used for the silicon itself is explained. Finally, the SDI procedure is described in detail and a brief idea of SSI is given.

At this point it should be noted that replication and inversion techniques are not the only possible approach for the fabrication of PBG-materials using DLW. In [136] the fabrication of 3D PBG-materials with a gap-midgap ratio of 3.5% using chalcogenide glass as a photoresist has been demonstrated. For this material, the index of refraction lies between 2.45 and 2.53, which suffices for PBG formation in the woodpile structure. It can further be doped with erbium, thus allowing for the introduction of light emitting material into the written structures [137]. However, when focusing the writing laser into a medium with significantly higher refractive index, several undesired effects on shape and position of the voxel have to be considered, which can only partly be overcome by appropriate countermeasures [136].

4.2.1 Silica Atomic Layer Deposition

Motivation

Standard chemical vapor deposition (CVD) processes are continuous — vapors flow continually into the reaction chamber where they are thermally reacted to deposit a film onto a sample [138]. Typically, such processes require temperatures of several $100°C$ to provide the activation energy necessary for the reaction to take place. Consequently, samples to be coated or infiltrated using CVD have to possess a high thermal stability. This requirement is not fulfilled by polymer templates obtained by DLW.
An alternative to conventional CVD is provided by atomic layer deposition (ALD) processes. Such processes can be controlled to deposit one atomic layer at a time, thus achieving near perfect uniformity and accurate thickness control. However, a drawback of this high degree of control is the long time it takes to grow films that are thicker than several tens of nanometers. For the deposition of films with thicknesses of several hundred nanometers it is therefore useful to pass on atomic thickness control by depositing multiple layers at once, thereby gaining orders of magnitude in the growth rate. Such processes are often called *ALD-like* or *pulsed layer deposition* (PLD) processes. However, for conformity with most of PhC literature, in this thesis the abbreviation ALD is used in this context as well.

Functional Principle

For ALD processes, a defined sequence of pulses, called a cycle, of different precursor and purging gases is repeatedly introduced into the reaction chamber until the desired film thickness is achieved. A typical ALD process is illustrated in Fig. 4.4.

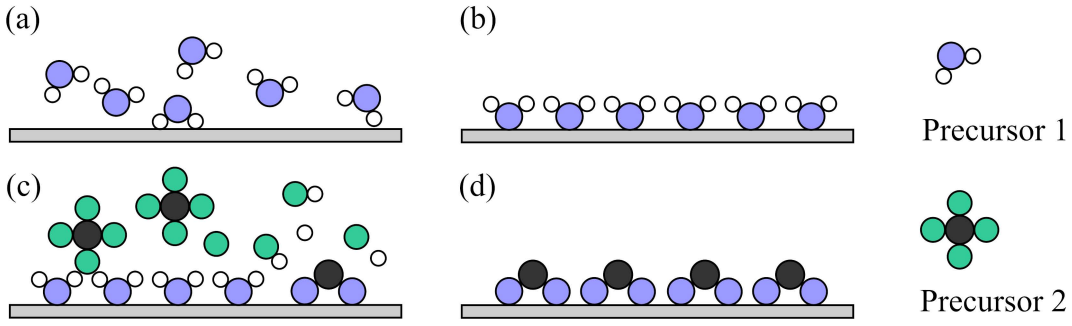

Figure 4.4: Illustration of the steps of an ALD process. Adapted from [138].

The following steps are performed [138]:

- Precursor 1 is introduced into the reaction chamber (a).
- A layer of precursor 1 molecules is formed on the surface of the sample by adsorption (b). Depending on the adsorption mechanism one distinguishes chemisorption and physisorption. If adsorption is self-terminated as soon as the sample is covered with

one monolayer of precursor molecules, atomic thickness control is achieved. Otherwise, higher growth rates can be obtained.

- The reaction chamber is purged with an inert gas in order to remove the precursor molecules that are not adsorbed to the surface (not shown).
- Precursor 2 is introduced into the reaction chamber (c).
- The precursor 2 molecules react chemically with the adsorbed precursor 1 molecules, thereby forming a layer of the material to be deposited at the sample surface (d). The process is self-terminated as soon as all molecules of precursor 1 are consumed by the reaction, leading to uniform thin-film deposition even inside complex 3D architectures.
- The reaction chamber is again purged to remove remnants of precursor 2 (not shown).
- This sequence is repeated until the desired film thickness is reached.

For deposition of amorphous silica (SiO_2), the first precursor is water (H_2O) and the second precursor is silicon tetrachloride ($SiCl_4$). As carrier gas and for purging, nitrogen (N_2) gas is used. The corresponding process can be performed at room temperature under normal pressure [139] and is therefore applicable for the infiltration of polymer templates obtained by DLW.
Under the described conditions, water molecules impinging on the sample surface form a multilayer of adsorbed H_2O, which exists in different phases [139]. Directly at the surface a monolayer of chemisorbed OH is formed. Further H_2O molecules are then physisorbed on top of this OH layer. This is, consequently, not a self-terminated reaction. High growth rates can thus be obtained with this process. If now the $SiCl_4$ is introduced into the chamber, the following chemical reaction takes place [140]: First, the $SiCl_4$ is completely hydrolyzed, *i.e.*, the Cl atoms are replaced by hydroxyl (OH) groups. The products of this reaction are acids. In the next step these acids polymerize to form siloxane chains and networks. Within these networks water molecules are incorporated, so that at first a silica gel is formed. This gel is spontaneously dehydrated when the water evaporates, leading to a shrinkage and finally to a layer of amorphous silica at the surface. This reaction can be summarized in a simplified manner by the following balance:

$$2\,H_2O + SiCl_4 \rightarrow SiO_2 + 4\,HCl. \tag{4.1}$$

The reaction continues as long as there are still water molecules present as reaction partners for the $SiCl_4$. Therefore, the thickness of the silica layer deposited in one cycle is determined by the amount of water adsorbed to the sample surface during the corresponding process step, and can be controlled by its duration.

Experimental Realization

Figure 4.5 shows a scheme of the ALD system (Setup: M. Hermatschweiler). The polymer template to be infiltrated is placed inside the reaction chamber **RC**. The reaction chamber

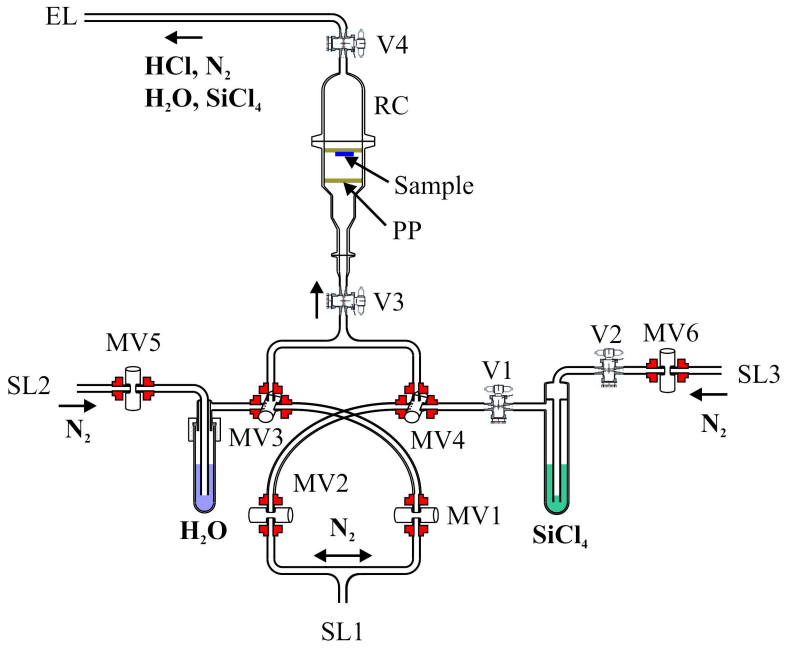

Figure 4.5: Schematic depiction of the silica ALD system (Setup: M. Hermatschweiler)

is then purged for $30\,\mathrm{min} - 45\,\mathrm{min}$ with a nitrogen flow of approx. $0.4\,\mathrm{l/min}$ through the supply line **SL1**. The porous plate **PP** diffuses the gas flow, leading to a uniform spatial distribution of the reactants. After purging, the nitrogen flow is directed through supply line **SL2** for a time t_1. On this path it passes a reservoir of distilled water before it reaches the reaction chamber. Water molecules are thus transported into the reaction chamber by the nitrogen flow, where they form an adsorbed layer on the surface of the sample. Afterwards the chamber is purged again for a time t_2 before the gas flow is directed through supply line **SL3** for a time t_3, where it passes a reservoir of $SiCl_4$ (Sigma-Aldrich 13736, >99%). The $SiCl_4$ molecules are carried to the reaction chamber by the nitrogen flow and react with the water film as described by the balance (4.1) forming SiO_2 and HCl. In order to remove unreacted $SiCl_4$ and the produced HCl from the outgoing nitrogen flow, the exhaust line **EL** is directed through two reservoirs of aqueous KOH (20% by weight) solution in row (not shown). At the end of each cycle the reaction chamber is again purged for a time t_4, before the entire sequence is repeated as many times as needed. Typical durations used for the infiltration processes performed in this thesis are $t_1 = 2\,\mathrm{min} - 5\,\mathrm{min}$, $t_2 = 5\,\mathrm{min}$, $t_3 = 1.5\,\mathrm{min}$, and $t_4 = 5\,\mathrm{min}$. By variation of t_1 the amount of silica deposited at a single cycle can be adjusted.

The deposition process is LabVIEW-automated by use of computer controlled magnetic valves **MV1**-**MV6**. The valves **V1**-**V4** have to be operated manually before the start of the first cycle and after the end of the last cycle.

4.2.2 Silicon Chemical Vapor Deposition

Functional Principle

In order to infiltrate thermally stable 3D structures with silicon, a continuous chemical vapor deposition (CVD) process is employed. The precursor gas used in this process is disilane (Si_2H_6). The sample is heated and at sufficiently high temperatures ($\approx 300°C$) the disilane molecules are decomposed, and silane (SiH_4) and silylene (SiH_2) are formed [141]:

$$Si_2H_6 \rightarrow SiH_4 + SiH_2. \tag{4.2}$$

Subsequently, the silylene is once again decomposed, forming amorphous silicon at the surface of the sample:

$$SiH_2 \rightarrow Si + H_2. \tag{4.3}$$

This reaction is predominantly responsible for silicon layer growth [141]. The temperature dependence of the reaction rate constant w can roughly be estimated by the Arrhenius equation [142]

$$w = Ae^{-\frac{E_A}{RT}}. \tag{4.4}$$

Here, T denotes absolute temperature, R the gas constant, E_A the activation energy of the considered process, and A is a process-dependent pre-exponential factor. If the temperature is increased, the reaction is accelerated, that is, the silicon growth rate also increases. For the infiltration of 3D nanostructures the temperature has to be chosen sufficiently low that the reactants have enough time to penetrate uniformly inside the structures before they react. This is essential in order to ensure that the reaction does not only take place at the outer surfaces of the structure but also uniformly at its inside. The chemical reaction described by Eq. (4.3) has an activation energy of $E_A = 33\,\mathrm{kCal/mol}$ and accordingly, deposition rates of more than $1\,\mathrm{nm/min}$ can already be obtained at $430°C$ [141]. Even though this temperature is comparably low for a CVD process, it is still too high for the infiltration of polymer templates obtained by DLW, which are already thermally destroyed at this temperature. SiO_2-inverse structures, however, can be infiltrated *via* silicon CVD and furthermore, it has been demonstrated that SiO_2 coated SU-8 templates can also withstand these temperatures [25].
Notably, the result of a deposition process does not only depend on the process parameters gas flow, temperature and pressure, but the substrate material plays a crucial role as well. While smooth films are obtained for growth on a silica surface, nano-rod formation is observed for deposition, *e.g.*, on samples covered with a gold film for SEM observation.

Experimental Realization

The system used for CVD of silicon films is schematically depicted in Fig. 4.6 (Setup: M. Hermatschweiler). The sample is built into the reaction chamber **RC** and the complete system is evacuated to a pressure of approx. 5 µbar. The pressure inside the chamber is measured by two capacitive membrane pressure pickups **P1** and **P2** (MKS Baratron 626A and

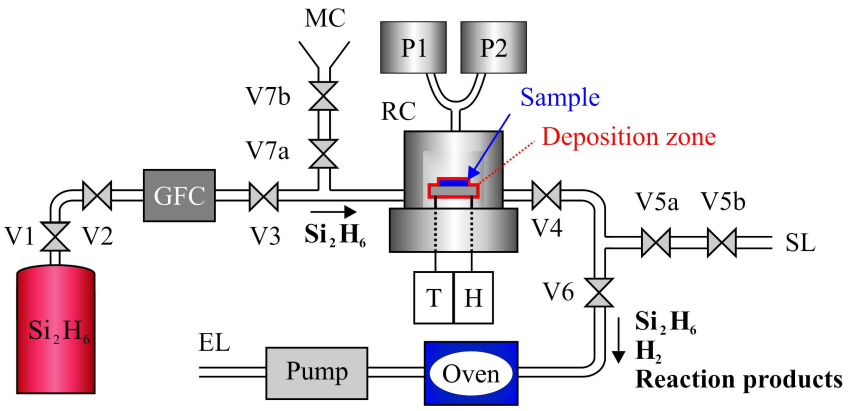

Figure 4.6: Schematic depiction of the silicon CVD system (Setup: M. Hermatschweiler)

627B). In parallel, the heater **H** is used to heat the sample to the desired temperature (nominally $475°C - 485°C$), which is controlled by the thermocouple **T**. As soon as the target conditions are reached, the actual CVD process can be started. For this purpose the disilane gas bottle (Linde Disilan 4.8) is opened *via* the valves **V1** and **V2**. Next, disilane is introduced into the chamber. To this end the gas flow control unit **GFC** (MKS 1179) is set to a gas flow of 1 sccm, thereby also opening the pneumatically operated valve **V3**, which is connected to the gas flow control unit. The valve **V4** serves to adjust the pressure inside the reaction chamber during the CVD process. For a disilane working pressure of $5\,\mathrm{mbar}$ high-quality silicon films and reasonable growth rates of several $\mathrm{nm/min}$ are obtained. After completion of the deposition process, the disilane flow is switched off and the valves **V1** and **V2** are closed again. The sample is cooled down to room temperature while the chamber is again evacuated. To dismount the sample, the chamber has then to be floated with nitrogen or air through the supply line **SL**. This is done by opening the valve **V5b**, while **V5a** is used to adjust the vent rate. To keep the oven evacuated, the valve **V6** is closed during venting. When ambient pressure is reached the chamber is ready to be opened and the silicon coated sample can be removed from the sample holder.

A particular challenge regarding silicon CVD from disilane is that disilane is spontaneously inflammable on air and that it forms spontaneously inflammable explosive mixtures with air. Therefore great care has to be taken in order to prevent the disilane from getting in contact with air, thus allowing for a safe operation of the CVD device. Several measures are taken for this purpose. First, it is essential that the gas flow must not be started before a base pressure below $10\,\mu\mathrm{bar}$ is reached. Second, the oven that precedes the vacuum pump is heated to a temperature of $750°C$. These high temperatures serve to thermally decompose disilane that passes the chamber without having reacted before feeding it into the exhaust line **EL**. Thereby other unwanted reaction products formed in the chamber are also disposed. Third, the valves **V7a** and **V7b** offer the possibility to exhaust and burn disilane from the chamber in a controlled fashion through the metal cone **MC** in the case of a system breakdown. Finally, a flush valve block (Spektron SBE/3-E61/62, not shown) enables a safe replacement of the disilane bottle.

4.2.3 Silicon Double Inversion

Silicon double inversion (SDI) of polymer templates obtained by DLW has been demonstrated for the first time by N. Tétreault *et al.* [24]. Similar approaches are reported in [102, 143]. Using SDI, polymer templates can be replicated into silicon structures to obtain PBG materials, owing to the increased refractive index contrast. Figure 4.7 illustrates the individual steps of this technique for the example of a woodpile structure. First, the polymer template shown in (a) is completely infiltrated with amorphous silica using ALD (see Subsection 4.2.1), which results in a polymer-silica composite structure (b). For the woodpile structures fabricated in this thesis, the minimum amount of silica that has to be deposited to achieve complete infiltration is determined by the bottlenecks appearing between neighboring rods in next but one layers. After the ALD process, the silica layer on top of the structure is removed by reactive ion etching (RIE) in order to uncover the photoresist template and allow for its removal. The RIE process employs a sulfur hexafluoride (SF_6) plasma ($40\,\mathrm{sccm}$ SF_6) at a pressure of $22\,\mathrm{mTorr}$ and $70\,\mathrm{W}$ forward power (Oxford Plasmalab 80 Plus RIE system), leading to etch rates of about $30\,\mathrm{nm/min}$. The photoresist is then removed by calcination at $420°\mathrm{C}$ in air for $12\,\mathrm{h}$ using a tube furnace (Carbolite MTF 12/38/400). This step results in a SiO_2-inverse structure (c). At this point, a structural shrinkage of 6–7% is observed [24], which is due to evaporation of H_2O molecules incorporated inside the SiO_2,

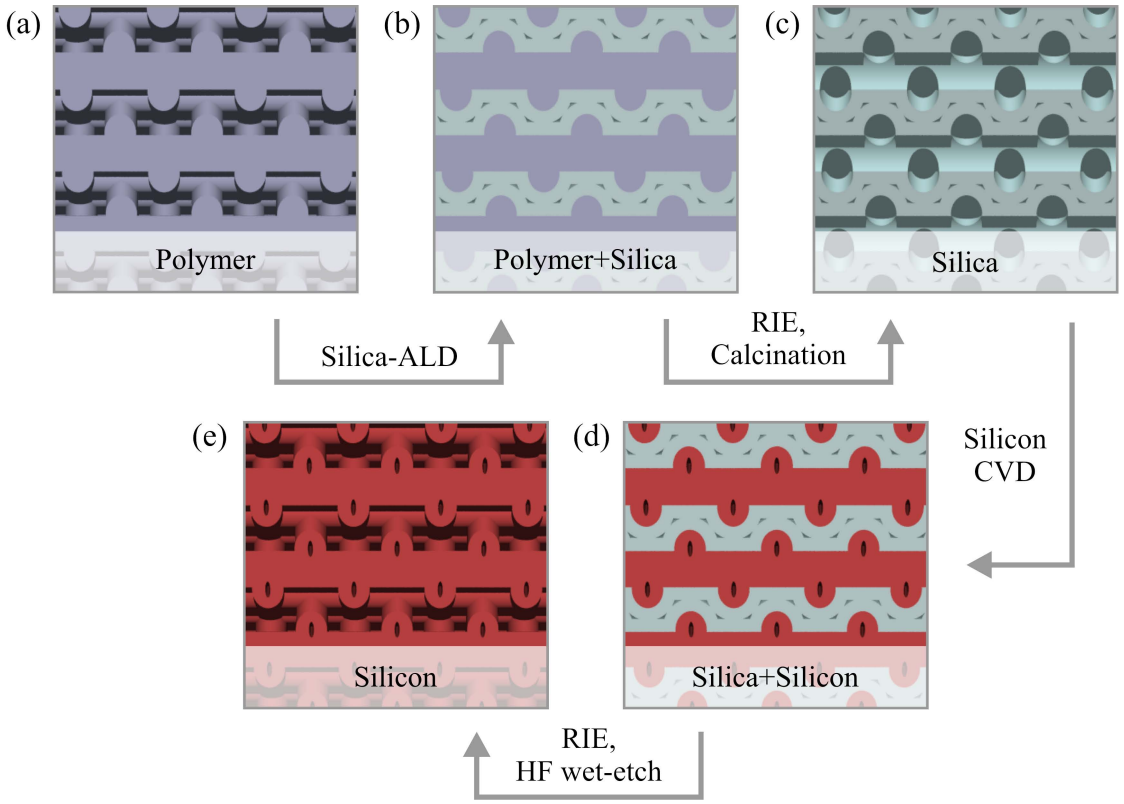

Figure 4.7: Process steps and their respective starting points and results (a)-(e) performed during a silicon double inversion procedure.

which did not react with $SiCl_4$ to form SiO_2 during the ALD process. The SiO_2-inverse structure is then infiltrated with Si *via* a CVD process (see Subsection 4.2.2). Doing this, a SiO_2-Si composite structure (d) is obtained. For the woodpile structure with lateral rod diameter d, the minimum Si-layer thickness that has to be deposited is $d/2$. Next,the silicon layer on top of the structure is removed by RIE. In this case, a SF_6-Ar-plasma ($10\,\mathrm{sccm}$ SF_6, $30\,\mathrm{sccm}$ Ar) at a pressure of $22\,\mathrm{mTorr}$ and $70\,\mathrm{W}$ forward power is applied, corresponding to an etch rate of about $130\,\mathrm{nm/min}$. Furthermore, the Si layer deposited on the back side of the substrate is removed with a fast RIE process using a SF_6-O_2-plasma ($40\,\mathrm{sccm}$ SF_6, $1.5\,\mathrm{sccm}$ O_2, $22\,\mathrm{mTorr}$, $100\,\mathrm{W}$ forward power). Finally, the SiO_2, which is uncovered by the RIE process, can be removed by a selective wet-etch using HF. To this purpose a few drops of 2 vol% aqueous HF are placed on the sample. After several minutes (the exact duration depends on the sample lattice constant and geometry) the sample is rinsed with destilled water. The whole procedure is repeated until no silica is left. The sample is then dried in a nitrogen flow. A change of the substrate before silica removal as described in [24] is not necessary if the wet-etch duration is adjusted carefully.
The result of the SDI procedure is a high-quality silicon replica of the photoresist template (e). Small deviations in geometry between template and replica are due to shrinkage of the silica inverse structures upon removal of the resist [24] and due to the appearance of bottlenecks, leading to incomplete silicon infiltration and thus to the formation of small pores inside the silicon rods as illustrated in Fig. 4.7 (d) and (e). Depending on the structure, the appearance of bottlenecks can be a property of the geometry itself or, as the case for the woodpile structure, be caused by small deviations from perfect uniformity of the rod thickness. Furthermore, deviations appear at the air-PhC interface on top of the structure, which can be rather rough due to repeated RIE and infiltration processes, and at the PhC-air interface at the bottom of the structure, where a thin Si-layer can form during the CVD process, if silica shrinkage causes the silica inverse structure to be slightly detached from the substrate.

4.2.4 Silicon Single Inversion

An approach which is closely related to SDI but allows to obtain an *inverse* silicon structure from a template, is silicon single inversion (SSI). Using SSI, inverse woodpiles at NIR frequencies, which exhibit even larger PBGs than their direct counterparts (compare Subsection 3.1.2), have been demonstrated by M. Hermatschweiler *et al.*[25] for the first time. The technique is illustrated in Fig 4.8. To perform a single inversion, the photoresist template (a) is first coated with silica by ALD (b). The coated sample is then infiltrated with silicon using CVD (c). During the CVD process the silica acts as a protective layer for the resist, such that the sample can preserve its form despite the high temperatures[1]. In addition, the thickness of the layer can be adjusted to tune the filling factor of the resulting silicon inverse PhC to a desired value. Next, the top silicon layer is removed by RIE, so as to allow for removal of the silica by selectively etching it with HF (d) and for removal of the resist by calcination (e). Again, infiltration bottlenecks are responsible for a complete infiltration of the inverse

[1]This technique is not only applied to create PBG materials but has also been adapted for the fabrication of 3D metamaterials by DLW and silver CVD [120].

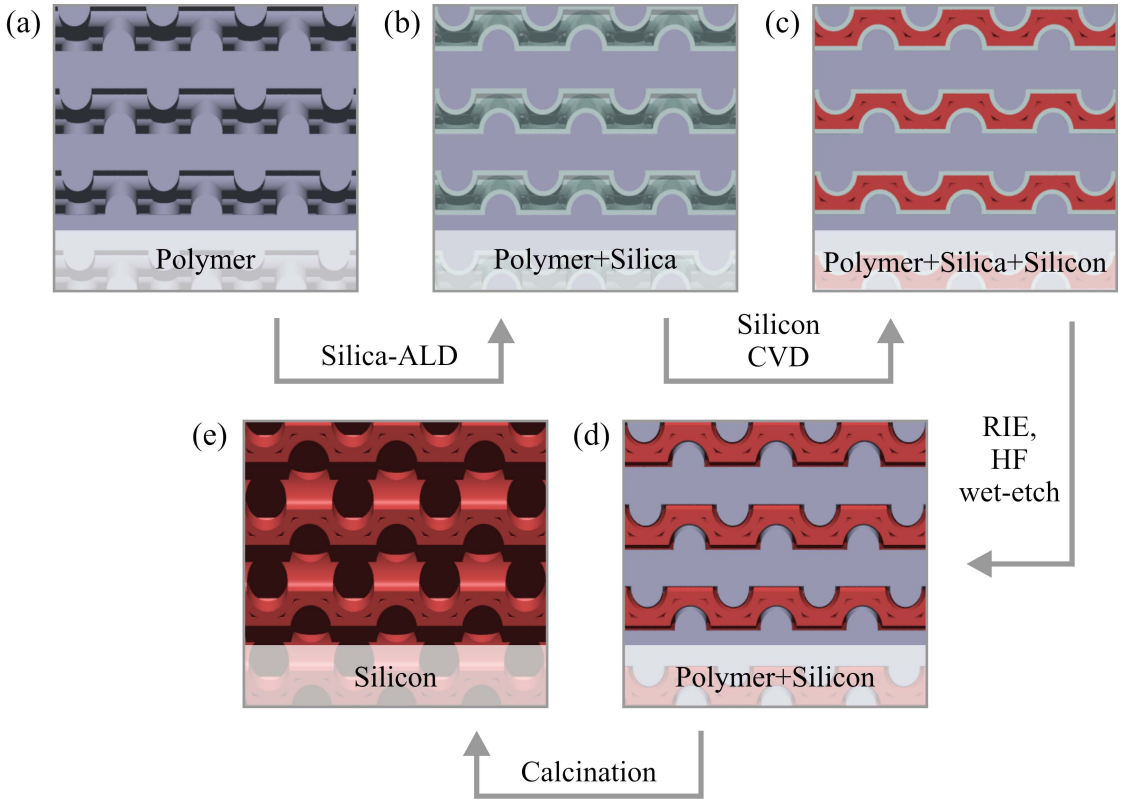

Figure 4.8: Process steps and their respective starting points and results (a)-(e) performed during a silicon single inversion procedure.

structure usually not being accomplished. For the woodpile structure, in particular, small voids are formed between adjacent rods as illustrated in Fig. 4.8 (d) and (e). Compared to SDI, SSI is technically more demanding for two reasons: First, a more precise thickness control is required during the silica ALD process. On the one hand, the deposited layer has to be thick enough to fulfill its function as a protective coating for the resist, on the other hand, it has to be sufficiently thin to leave enough space for silicon infiltration. Second, the silicon is nowhere directly connected with the original glass substrate, but silicon growth entirely takes place on silica deposited by ALD. Complete removal of the silica therefore always involves the detachment of the silicon structure from the substrate, which can result in loss of the sample during the HF wet-etch step.

4.3 Optical Characterization

Complete PBG-structures produced by DLW and silicon replication or inversion typically have broad and prominent stop bands located in the spectral region between $1\,\mu\mathrm{m}$ and $4\,\mu\mathrm{m}$, depending on their lattice constant and structural parameters. Therefore, in order to measure the spectra of these structures, a high bandwidth in the NIR has to be covered and consequently, reflective optics have to be employed so as to avoid chromatic aberrations and ab-

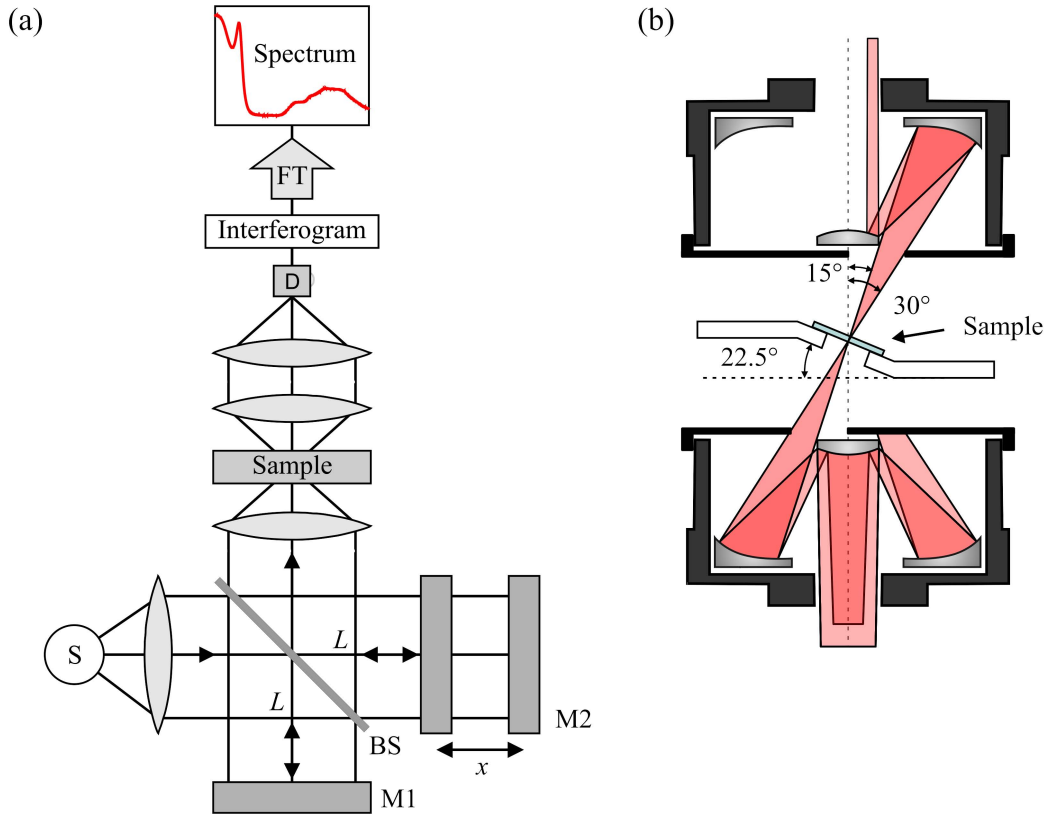

Figure 4.9: (a) Schematic of a typical FTIR spectrometer setup. (b) An aperture is introduced into the beam path of the Cassegrain objective in order to allow for perpendicular incidence measurements using the reflective optics of the commercial instrument.

sorption caused by conventional glass optics. Furthermore, the fabricated structures usually have relatively small footprints, only several tens of micrometers squared, so that focusing and imaging optics are required.
These requirements are fulfilled by a Fourier-transform infrared (FTIR) microscope-spectrometer with attached infrared microscope.

Functional Principle

Using an FTIR spectrometer, it is possible to measure the linear-optical reflectance and transmittance spectra of a sample for a whole range of wavelengths simultaneously. The core piece of this technique is a Michelson interferometer. A schematical depiction of a typical FTIR setup is provided by Fig. 4.9 (a) [144]. Broadband IR-radiation emitted from a thermal source **S** impinges onto a beam splitter **BS**. Here, 50% of the radiation intensity is reflected, the other 50% are transmitted. The reflected part of the radiation is again reflected at a mirror **M1** after having travelled a path length L. The transmitted part is reflected at a mirror **M2**. This mirror, however, is not fixed but can be moved back and forth periodically along the optical axis. The displacement with respect to pathlength L is denoted by x. Accordingly,

the optical path distance of the two beams upon recombination at the beam splitter is $2x$. The recombined beams leave the interferometer, pass (or are reflected by) the sample and are finally focused on a detector **D**, where the interferogram, that is, the radiation intensity $I(x)$ as a function of the mirror displacement x, is recorded. Fourier transforming the interferogram and dividing by an appropriate reference spectrum provides the spectrum of the sample.

Description of the Instrument

The instrument used in this thesis is a Bruker EQUINOX 55 FTIR with an attached HYPERION 2000 IR-microscope. It covers a spectral range from $20,000\,\mathrm{cm}^{-1}$ ($500\,\mathrm{nm}$) to $2,000\,\mathrm{cm}^{-1}$ ($5\,\mu\mathrm{m}$). The light source is a NIR tungsten-halogen lamp. In the spectral range from $2,000\,\mathrm{cm}^{-1}$ ($5\,\mu\mathrm{m}$) to $11,000\,\mathrm{cm}^{-1}$ ($909\,\mathrm{nm}$) a CaF_2 beam splitter and a liquid nitrogen cooled InSb detector are utilized, from $9,000\,\mathrm{cm}^{-1}$ ($1.11\,\mu\mathrm{m}$) to $20,000\,\mathrm{cm}^{-1}$ ($500\,\mathrm{nm}$) a quartz beam splitter and a silicon photodiode are employed. The maximum resolution of the instrument is $0.5\,\mathrm{cm}^{-1}$, corresponding to $0.12\,\mathrm{nm}$ at $1.55\,\mu\mathrm{m}$. Selective measurements of small (minimum sampling area diameter $8.3\,\mu\mathrm{m}$) sample areas can be accomplished by use of the provided apertures. Furthermore, polarizers can be inserted into the beam path, thus allowing for polarization resolved spectroscopy.
As mentioned before, the instrument relies on reflective optical components in order to avoid chromatic aberrations, which would otherwise be significant due to the large spectral bandwidth. The IR-microscope employs a $36\times$ Cassegrain objective with a numerical aperture of $NA = 0.5$. For measurements in reflectance mode, the light reflected by the sample is collected by the same objective that is used for focusing the light onto the sample. In transmittance mode, two identical Cassegrain objectives are used, one for focusing and one for collecting the light transmitted through the sample. Reference measurements are performed on a silver mirror in reflectance and through a bare glass cover slide in transmittance.
The suppression of background transmission that can be achieved by this instrument in transmittance mode is limited. This becomes particularly important for measurements on small-footprint samples, that strongly suppress the transmitted signal in a certain spectral range. The specific attainable values are explored in Appendix B for different measurement configurations.
By construction of the Cassegrain objectives, both the incident and the collected light span an angular range from 15 degrees to 30 degrees (half opening angle). Although these illumination and detection characteristics can offer advantages, *e.g.*, in order to probe many directions in reciprocal space of a PBG-material simultaneously, actual perpendicular-incidence measurements are not possible in this configuration. In this thesis, two workarounds have been developed for this problem.
One is to reduce the angular spread with an aperture and tilt the sample by means of an appropriate holder, as depicted in Fig. 4.9 (a). This method has successfully been applied in [121, 134, 145–147]. The obtained opening angle can be adjusted by the choice of the aperture size. However, the signal strength is reduced to a fraction of its initial value by this technique. In situations, where signal strength is critical, satisfactory results may not be obtained by this method.

A second possibility to measure perpendicular incidence has been created by the construction of a CaF objective for the IR-microscope. CaF is transparent up to approx. $12\,\mu\mathrm{m}$ wavelength and shows relatively little dispersion. A $f = 50\,\mathrm{mm}$ CaF Lens (CF-PX-12-50, ISP Optics Corp.) has been integrated into a $4\times$ objective (NT43-902, Edmund Optics GmbH), where the original lens has been removed. The range of application of this objective is limited to sample areas larger than $200\,\mu\mathrm{m}\times 200\mu\mathrm{m}$. It is used in combination with a home-made MATLAB program to determine the thickness of films deposited by ALD or CVD *via* measurement and parameter fit of their Fabry-Perot oscillations. The derived film thicknesses are in very good agreement with thicknesses measured with a commercial reflectometer (Nanocalc 2000, Mikropack GmbH).

4.4 Numerical Methods

In the previous section an experimental method for the optical characterization of the fabricated PhC structures has been described. Yet, in order to interpret and analyze the experimental results, it is necessary to compare them to theoretically expected optical characteristics. For this purpose, band structures and spectra have been computed using two different software packages. Band structure calculations have been performed with the freely available MIT Photonic-Bands (MPB) package [148]. The computational method implemented by the MPB-package is summarized in Subsection 4.4.1. Theoretical transmittance and reflectance spectra have been computed in cooperation with the group of K. Busch by S. Essig. In this case, an internally developed scattering-matrix code has been used. Subsection 4.4.2 provides a brief overview of the employed algorithm. A review of different numerical methods applicable for PhC defect structure calculations, can, for example, be found in [32].

4.4.1 Band Structure Calculations

To obtain the band structure of a given PhC one has to solve the wave equation (2.23), subject to transversality

$$(i\boldsymbol{k} + \nabla) \cdot \boldsymbol{u}_{\boldsymbol{k}} = 0, \tag{4.5}$$

for the frequencies of the periodic system as a function of $\boldsymbol{k}$. Inserting a Bloch state $\boldsymbol{H}_{\boldsymbol{k}}(\boldsymbol{r}) = e^{i\boldsymbol{k}\cdot\boldsymbol{r}}\boldsymbol{u}_{\boldsymbol{k}}(\boldsymbol{r})$ into (2.23) yields

$$\left[(i\boldsymbol{k} + \nabla) \times \frac{1}{\varepsilon(\boldsymbol{r})}(i\boldsymbol{k} + \nabla)\times\right] \boldsymbol{u}_{\boldsymbol{k}}(\boldsymbol{r}) = \frac{\omega(\boldsymbol{k})^2}{c^2}\boldsymbol{u}_{\boldsymbol{k}}(\boldsymbol{r}). \tag{4.6}$$

The most common algorithm to solve (4.6) is the plane-wave expansion method [54], which is briefly summarized in the following.

Plane-Wave Expansion

As a first step to solve (2.23) both the inverse dielectric function as well as the lattice periodic part of the Bloch modes $\boldsymbol{u_k}(\boldsymbol{r})$ are expressed as Fourier series, yielding

$$\frac{1}{\varepsilon(\boldsymbol{r})} = \sum_{\boldsymbol{G}} \varepsilon_{\boldsymbol{G}}^{-1}\, e^{i\boldsymbol{G}\cdot\boldsymbol{r}} \tag{4.7}$$

with series coefficients

$$\varepsilon_{\boldsymbol{G}}^{-1} = \frac{1}{V_0}\int_{V_0} d^3\boldsymbol{r}\, \frac{1}{\varepsilon(\boldsymbol{r})}\, e^{-i\boldsymbol{G}\cdot\boldsymbol{r}} \tag{4.8}$$

and

$$\boldsymbol{u_k}(\boldsymbol{r}) = \sum_{\boldsymbol{G}} \boldsymbol{c_G}(\boldsymbol{k})\, e^{i\boldsymbol{G}\cdot\boldsymbol{r}} \tag{4.9}$$

with coefficients

$$\boldsymbol{c_G}(\boldsymbol{k}) = \frac{1}{V_0}\int_{V_0} d^3\boldsymbol{r}\; \boldsymbol{u_k}(\boldsymbol{r})\, e^{-i\boldsymbol{G}\cdot\boldsymbol{r}}, \tag{4.10}$$

where V_0 is the unit-cell volume. In both cases, because of lattice periodicity, it is sufficient to sum over all reciprocal lattice vectors $\boldsymbol{G}$. Applying the transversality constraint to Eq. (4.9) leads to

$$(\boldsymbol{k}+\boldsymbol{G})\cdot\boldsymbol{c_G} = 0. \tag{4.11}$$

The transversality constraint is automatically fulfilled if the fields are chosen to be superpositions of transverse plane waves. Therefore, for each $\boldsymbol{G}$ two perpendicular unit vectors $\hat{\boldsymbol{e}}_{\boldsymbol{G}}^{(1)}$ and $\hat{\boldsymbol{e}}_{\boldsymbol{G}}^{(2)}$ orthogonal to $\boldsymbol{k}+\boldsymbol{G}$ are chosen and $\boldsymbol{c_G}$ is expressed as $\boldsymbol{c_G} = \mathrm{c}_{\boldsymbol{G}}^{(1)}\hat{\boldsymbol{e}}_{\boldsymbol{G}}^{(1)} + \mathrm{c}_{\boldsymbol{G}}^{(2)}\hat{\boldsymbol{e}}_{\boldsymbol{G}}^{(2)}$. Inserting (4.9) into eigenequation (4.6) and Fourier transforming both sides, one obtains

$$\sum_{\boldsymbol{G}} \left[-\varepsilon_{\boldsymbol{G}'-\boldsymbol{G}}^{-1}\cdot(\boldsymbol{k}+\boldsymbol{G}')\times(\boldsymbol{k}+\boldsymbol{G})\times\right]\boldsymbol{c_G} = \frac{\omega^2}{c_0^2}\boldsymbol{c_{G'}}. \tag{4.12}$$

This is again an eigenvalue problem. However, instead of a differential equation as (4.6), this is now an infinite set of linear equations for an infinite set of unknowns $\boldsymbol{c_G}$. After truncation this problem can readily be solved on a computer by standard algorithms. As a result one obtains the eigenvalues and the eigenvectors, that is, band structure and field distributions of the PhC.

The MPB-Package

In principle, the MPB-package, which has been employed for all band structure calculations performed in the course of this thesis, is based on a method very similar to the above described plane-wave expansion method. Some specialties of the implementation are briefly summarized in the following, further details can be found in [148].
A typical problem that arises for methods based on plane-wave expansion is that discontinuities of the dielectric function can lead to poor convergence [60]. This is due to the fact that it is difficult to reproduce these discontinuities by Fourier series. The implementation of the

MPB-package alleviates this problem by using a smoothed version of the dielectric function. Another problem in solving (4.12) directly is potentially given by the size of the problem. Given an $N \times N$ matrix, an exact solution of the system of equations (4.12) by standard matrix algorithms needs $O(N^2)$ memory and $O(N^3)$ computation time, which is too much to allow for converged solutions for larger systems with reasonable resources. The MPB-package reduces the computational effort using an iterative method to solve the problem for a small number of bands p simultaneously. In this way, only $O(Np)$ storage and a computation time of roughly $O(Np^2)$ are required, multiplied by the (typically small) number of iterations [148]. The method is based on the variational theorem for the Maxwell eigenproblem, which has been introduced in Subsection 2.2.3. Solution of the system of equation then breaks down to a minimization problem. The MPB-package performs this minimization *via* the preconditioned nonlinear conjugate-gradient method [149].

Calculations for Defect Structures

The above described method to calculate the band structure and the mode profiles of a PhC is based on the periodicity of the PhC. This periodicity is broken by the introduction of a defect. However, the method can still be applied using the supercell approximation [42, 45]. This means that the defect is surrounded by a large computational cell of undisturbed PhC structure, which is taken as the new unit cell of the structure and periodically continued. Strictly speaking, one does not calculate true defect modes in this way, but impurity bands for a periodic arrangement of defects. However, since the defect modes are exponentially localized at the defect site, the solution converges exponentially fast to the solution of an isolated defect with supercell size. One property making supercell calculations computationally expensive, apart from the large computational cell alone, is that the original bands are folded many times over in the supercell's 1st BZ, such that significantly more bands have to be computed. More precisely, in a $p \times q \times r$-supercell, for every single band in the original unit cell, $p \cdot q \cdot r$ bands have to be computed in the supercell. Since artificial periodicity is only introduced in those directions where the structure lacks natural periodicity, PhC waveguide modes can be computed more efficiently by this technique than PhC cavity modes.
For the woodpile structure, there are several possibilities regarding the choice of the unit cell, which is periodically continued to form a supercell of the size $p \times q \times r$. In this thesis, the primitive unit cell is not used, instead the unit cell is chosen to have dimensions $a \times a \times c$ with its edges oriented parallel to the two rod directions of the woodpile structure and in stacking direction, respectively. Thus, for a bcc woodpile structure, this unit cell has dimensions $a \times a \times a$ and coincides with the bcc conventional unit cell. The geometry of this unit cell is favorable for the introduction of vertical waveguides.

4.4.2 Scattering-Matrix Calculations

Knowledge of the band structure of a PhC is a valuable ingredient for understanding its optical properties. Nevertheless, when measuring the experimental spectra of finite photonic crystals, interfaces have to be taken into account. At interfaces, refraction and diffraction

takes place, and they give rise to surface waves. Furthermore, as pointed out in Subsection 2.2.4, the symmetry of a Bloch mode determines if an impinging plane wave can generally couple to this mode. Therefore, when aiming at a comparison of experimental spectra with theory, band-structure calculations have to be complemented by another computational method. In this thesis, the scattering-matrix formalism is chosen for this purpose. As already mentioned, these calculations have been performed in cooperation with the group of K. Busch by S. Essig.

Computational Principle

The scattering-matrix formalism allows for the calculation of theoretical reflectance and transmittance spectra of photonic structures, which are finite in one direction and periodic in the two perpendicular directions. Detailed descriptions of the algorithm are given in [150–152]. Here, an overview is provided.
A typical setting for optical transmittance and reflectance measurements as it is assumed for the scattering-matrix algorithm is schematically depicted in Fig. 4.10. Coming from a half

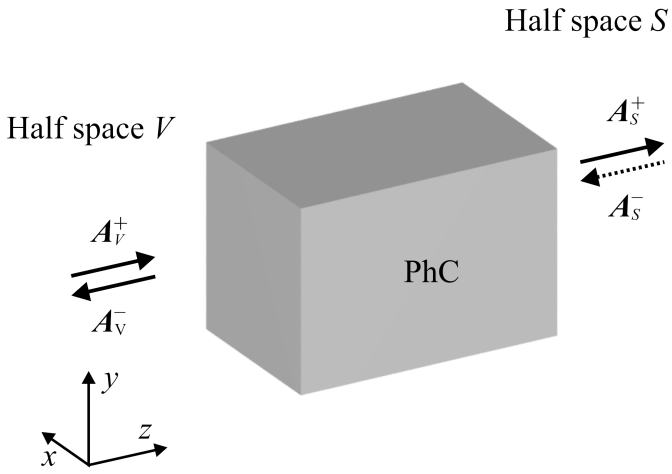

Figure 4.10: Illustration of an optical transmittance and reflectance measurement. The scattering-matrix connects the amplitudes of the incident electromagnetic waves on both sides of the sample with those of the outgoing waves.

space V, an electromagnetic wave with amplitude $\boldsymbol{A}_V^+$ and a wave vector $\boldsymbol{k}_{in}$, which has a non-zero component k_z, impinges onto a finite periodic structure. The wave is partially transmitted into a half space S and partially reflected back into half space V by the structure. The amplitudes of the reflected and transmitted waves are denoted by $\boldsymbol{A}_V^-$ and $\boldsymbol{A}_S^+$, respectively. In principle, the formalism allows for the existence of another wave with amplitude $\boldsymbol{A}_S^-$, coming from half space S and traveling in negative z-direction. However, since this wave is absent in most experiments, $\boldsymbol{A}_S^-$ is usually set to zero.

There are different possibilities to connect the incoming and outgoing waves on both sides of the sample *via* a matrix formalism, the most common of which is the transfer-matrix formalism [153]:

$$\begin{pmatrix} \boldsymbol{A}_S^+ \\ \boldsymbol{A}_S^- \end{pmatrix} = \mathbb{T}_{V,S} \begin{pmatrix} \boldsymbol{A}_V^+ \\ \boldsymbol{A}_V^- \end{pmatrix}. \tag{4.13}$$

Here, $\mathbb{T}_{V,S}$ is the transfer matrix connecting the wave amplitudes on one side of the sample with those on the other side of the sample. In principle, the problem can be solved by calculating $\mathbb{T}_{V,S}$. However, the transfer-matrix formalism suffers from numerical instabilities caused by the existence of growing evanescent waves that occur at the interfaces inside the PhC [154].
This problem is ruled out by the scattering-matrix formalism. The scattering matrix $\mathbb{S}_{V,S}$ is defined as the matrix that connects the amplitudes of the incident waves on both sides of the sample with those of the outgoing waves on both sides of the sample:

$$\begin{pmatrix} \boldsymbol{A}_S^+ \\ \boldsymbol{A}_V^- \end{pmatrix} = \mathbb{S}_{V,S} \begin{pmatrix} \boldsymbol{A}_V^+ \\ \boldsymbol{A}_S^- \end{pmatrix}. \tag{4.14}$$

Thus, if the amplitudes of the incident waves $\boldsymbol{A}_V^+$ and $\boldsymbol{A}_V^-$ are known, (4.14) can be used to calculate the reflected and transmitted waves $\boldsymbol{A}_V^-$ and $\boldsymbol{A}_S^+$. Yet, $\mathbb{S}_{V,S}$ has to be determined.

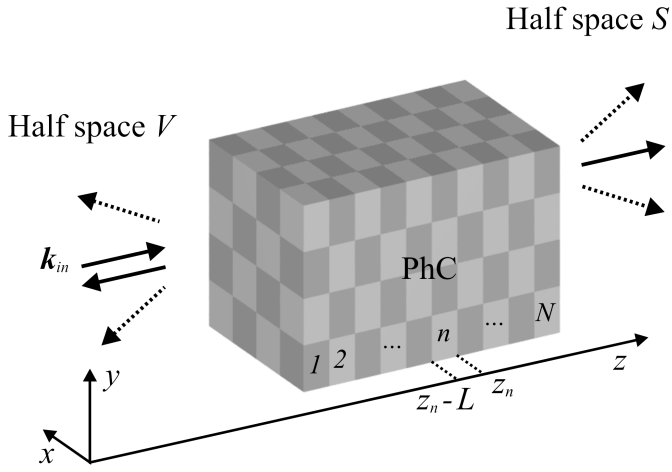

Figure 4.11: Decomposition of the sample in N layers of thickness L, that are periodic in the xy-plane and homogeneous in z-direction. The dashed arrows illustrate the different Bragg orders of the reflected and transmitted waves.

For this purpose, the structure is partitioned into a finite number N of layers with thickness L as illustrated in Fig. 4.11. The layers are homogeneous in z-direction and periodic in the xy-plane. Owing to in-plane periodicity, different Bragg orders can be observed, as illustrated by the dashed arrows in Fig. 4.11. The decomposition into layers now allows for the calculation of the 2D eigenmodes for each layer by plane-wave expansion (compare Subsection 4.4.1). The solutions are Bloch modes in the xy-plane and have an exponential dependence along

z. In the numerical calculation only a finite number of plane waves can be used for the expansion, which translates into a cutoff for the maximum Bragg order that is computed. Once the eigenmodes of the individual layers are known, the layers have to be connected again.
To this end, two transfer matrices are calculated for every layer n. $\mathbb{T}_{P_n}$ propagates the amplitudes from the front of layer n at $z_n - L$ to its back at z_n, $\mathbb{T}_{B_n}$ implements the continuity conditions for the boundary between layers n and $n+1$:

$$\begin{pmatrix} \boldsymbol{A}_n^+(z) \\ \boldsymbol{A}_n^-(z) \end{pmatrix} = \mathbb{T}_{P_n} \begin{pmatrix} \boldsymbol{A}_n^+(z-L) \\ \boldsymbol{A}_n^-(z-L) \end{pmatrix} \text{ and } \begin{pmatrix} \boldsymbol{A}_n^+(z) \\ \boldsymbol{A}_n^-(z) \end{pmatrix} = \mathbb{T}_{B_n} \begin{pmatrix} \boldsymbol{A}_{n+1}^+(z) \\ \boldsymbol{A}_{n+1}^-(z) \end{pmatrix}. \quad (4.15)$$

Here, the $\boldsymbol{A}_n^{\pm}$ denote the amplitudes for each layer. The superscript indicates the propagation direction while the subscript gives the number of the layer the waves are propagating in.
The scattering matrix $\mathbb{S}_{V,S}$ for the entire sample can now be derived by a recursive algorithm, where the scattering matrix $\mathbb{S}_{V,n}$ for a system of n layers is obtained from the scattering matrix $\mathbb{S}_{V,n-1}$ for the system of $n-1$ layers and the inverse transfer matrix of the additional layer. The algorithm starts from the trivial condition $\mathbb{S}_{V,V} = \mathbb{I}$, where $\mathbb{I}$ is the identity. A detailed description of this procedure is beyond the scope of this thesis and can be found in [150–152].

If the transmitted and reflected waves are known, transmittance T and reflectance R can be calculated *via* the z-components of the respective Poynting vectors, S_z^{in} for the incident, S_z^{trans} for the transmitted, and S_z^{refl} for the reflected wave [152]:

$$T = \frac{S_z^{\text{trans}}}{S_z^{\text{in}}}; \qquad R = \frac{-S_z^{\text{refl}}}{S_z^{\text{in}}} \quad (4.16)$$

Calculation of T and R then allows for direct comparison with experimental linear-optical intensity transmittance and reflectance spectra.

Calculations for Defect Structures

As already the case for band-structure calculations, scattering-matrix calculations are based on the periodicity of the photonic structure. Consequently, the supercell technique has to be applied again when this periodicity is broken by the presence of a defect, with corresponding consequences for the numerical effort. In contrast to band-structure calculations, however, in scattering matrix calculations periodicity is assumed in the xy-plane only, while the structure is modeled to be finite in z-direction. As a consequence, the same supercell dimensionality, namely two, is needed for a point defect as well as for a waveguide oriented in z-direction.
For scattering-matrix calculations performed in this thesis for woodpile structures containing point defects and waveguides in z-direction, the required 2D unit cell, which is periodically continued to form a supercell of size $p \times q$, is chosen to have dimensions $a \times a$ and to be oriented with its edges parallel to the two rod directions of the woodpile.

Calculations for Structures with High Index Contrast

3D PBG-materials are necessarily high-index materials, since a minimum dielectric contrast is required in order to allow for the formation of a PBG in three dimensions. Therefore, sharp discontinuities of the dielectric function can typically be found at the material-air interfaces inside a PBG-material. This is unfavorable for the scattering matrix algorithm, because it relies on Fourier expansion of products of a field and the dielectric function within each layer, and in the presence of sharp discontinuities the convergence of this step can be poor [155–157]. The explanation for this phenomenon as well as rules for improvement, regarding how the Fourier expansion should be carried out, have been provided in [158]. The implementation of these rules leads to a significantly reduced number of plane waves needed for the Fourier expansion and to drastically improved convergence of the scattering-matrix algorithm [159]. The scattering-matrix code used by S. Essig includes an implementation of these rules, thus making high-index material supercell calculations possible.

Chapter 5

A Complete Bandgap at Telecom Wavelengths

5.1 Blue-Shifting the Photonic Bandgap

Many possible devices based on PBG-materials are envisioned to find applications in the field of optical data communication (compare Chapter 1). It is therefore an important requirement that these devices can be realized to operate at wavelengths that are compatible with existing telecommunication technology. The relevant telecommunication wavelength bands are determined by the optical properties of single-mode silica fibers used for long-range optical data communication, which have their dispersion minimum at $1.3\,\mu\mathrm{m}$ and absorption minimum at $1.55\,\mu\mathrm{m}$ wavelength.
However, fabrication of PBG-materials operating at these wavelengths is challenging. Existing experimental realizations are based on methods which are either costly and time-consuming or do not allow for a precise, controlled, and flexible incorporation of defect structures, which is essential for most applications considered in the context of telecommunication technology (see discussion in Section 3.3).
It is therefore highly desirable to access this wavelength regime with 3D PBG-materials fabricated by DLW and SDI (see Chapter 4), which is an extremely flexible and comparably fast technique. Up to now, silicon woodpiles with a PBG of 8.6% gap-midgap ratio centered at $2.35\,\mu\mathrm{m}$ wavelength have been demonstrated along these lines by N. Tétreault *et al.* in [24]. These structures, which are based on SDI of an SU-8 template, have fcc lattice symmetry and a lateral rod distance of $a = 940\,\mathrm{nm}$.
From the scaling law of Maxwell's equations for the length scales (2.27) and the results reported in [24], one can easily estimate that, to obtain a PBG at $1.5\,\mu\mathrm{m}$ wavelength, woodpiles with lateral rod distances around $600\,\mathrm{nm}$ have to be realized. At first sight it looks simple to scale down the structures presented in Ref. [24] to roughly two third of their original size. The dimensions required for such structures are, however, not compatible with conventional SU-8 processing as it is described in Subsection 4.1.2. Four different ideas are therefore combined in the following in order to overcome this limitation and make the experimental

realization of PBG-materials with operation wavelengths in the telecommunication regime by DLW and SDI possible.

5.1.1 Symmetry Considerations

The spectral position of the PBG of a given woodpile structure depends on several parameters. The most obvious way to shift the PBG position of a given silicon woodpile to smaller wavelengths is to scale down the entire structure. This is, however, no longer possible if the resolution limit of DLW in a given resist is already reached, which is the case for rod distances a of approx. $700\,\mathrm{nm}$ for standard SU-8. Another way to achieve a blue-shift in wavelength is to reduce the filling fraction of the woodpile structure, which results in higher mode frequencies. For this purpose the rods composing the woodpile have to be made thinner. Yet, when already working at the resolution limit, this cannot be accomplished without negative impact on stability, quality, and reproducibility of the fabricated templates.
In this thesis, another option has hence been exercised, which is to change the symmetry of the underlying lattice of the woodpile structure in order to obtain a PBG blue shift. Figure 5.1 shows the computed positions of the PBG for several woodpile structures which have identical lateral rod distances a but differ in their ratios c/a of axial lattice constant and lateral rod distance. The positions of the band edges shown here have been calculated from $c/a = 1.0$ to $c/a = 1.4$ in steps of 0.1 and for $c/a = \sqrt{2}$. In between two adjacent points

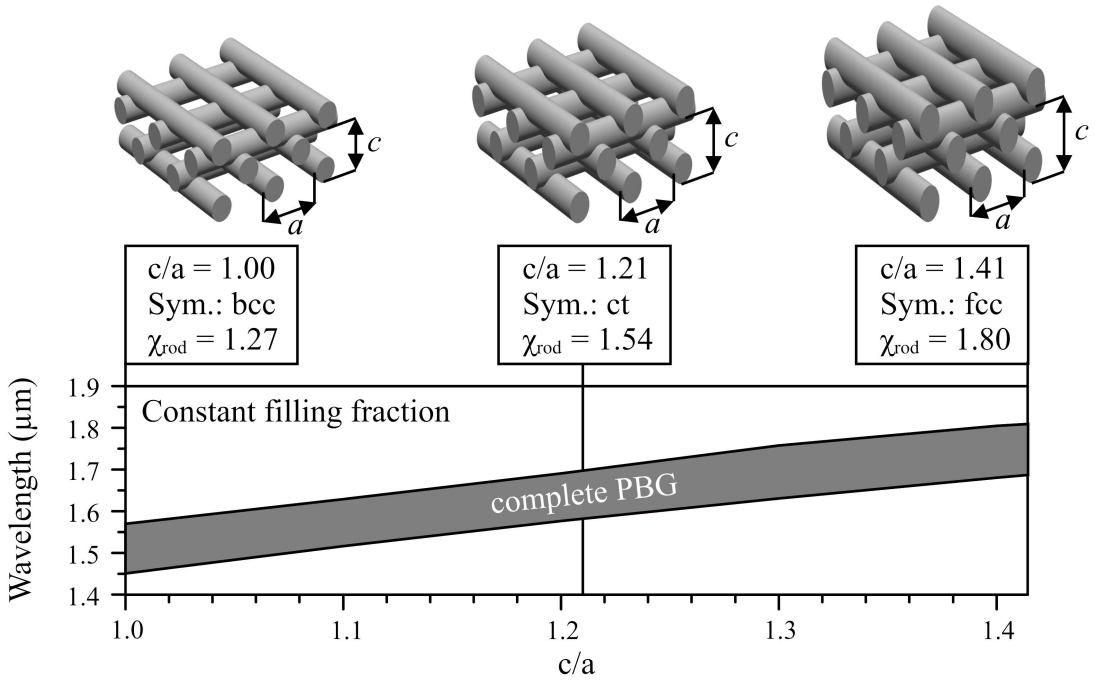

Figure 5.1: Position of the complete bandgap as a function of the ratio c/a of a woodpile structure with $a = 566\,\mathrm{nm}$, $\varepsilon = 9.9$, and $d_{\mathrm{rod}} = 0.365\,a$. Here, the filling fraction is kept constant by preserving the rod width d_{rod} and adjusting the rod aspect ratio χ_{rod} accordingly.

a linear interpolation is depicted. For illustrative purposes the structures corresponding to the fcc and the bcc case as well as to an intermediate ratio of $c/a = 1.21$ are also depicted within Fig. 5.1. The filling fraction of the structures is kept constant for all calculated points by appropriately adjusting the rod aspect ratio χ_{rod} while preserving the width d_{rod} of the rods. This adjustment is necessary in order to eliminate PBG shifts from the analysis, which are caused by filling fraction variation. An experimental method to adjust χ_{rod} is introduced in the following subsection.
From Fig. 5.1 it can indeed be observed that the PBG appears at smaller wavelengths for lower values of the ratio c/a. Furthermore, the size of the PBG stays approximately constant despite this change in symmetry. Consequently, reducing the ratio c/a provides a promising experimental route to shift the position of the PBG of a woodpile structure to smaller wavelengths without increasing the lithographic miniaturization challenge. In the following we are thus aiming at structures with an underlying lattice that is no longer fcc but closer to bcc.

5.1.2 Aspect Ratio Engineering

In the previous subsection it has been pointed out that the position of the PBG of a fcc silicon woodpile structure can be blue-shifted by a reduction of the ratio c/a, if the filling fraction is kept constant by reducing the rod aspect ratio χ_{rod} by the same factor as c/a. Furthermore, it has been demonstrated for an exemplary structure, that by doing this the size of the PBG stays approximately the same in the range from $c/a = \sqrt{2}$ to $c/a = 1.0$. However, in Subsection 4.1.3 where the two setups used for DLW are described, it is stated that the ex-

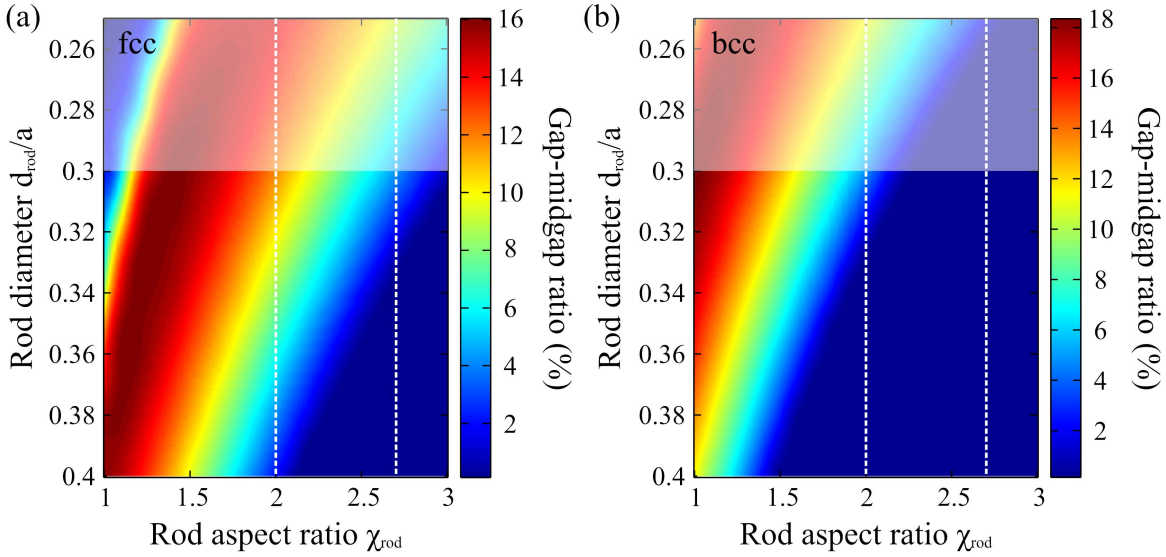

Figure 5.2: Gapmap for a fcc (a), and a bcc (b) silicon woodpile structure. For the silicon, a dielectric constant of $\varepsilon = 11.76$ is assumed. The white shaded regions indicate that fabrication reproducibility decreases for small rod diameters. The white dashed lines mark the values of the rod aspect ratios relevant for DLW with ($\chi_{\mathrm{voxel}} = 2$) and without ($\chi_{\mathrm{voxel}} = 2.7$) shaded ring filter.

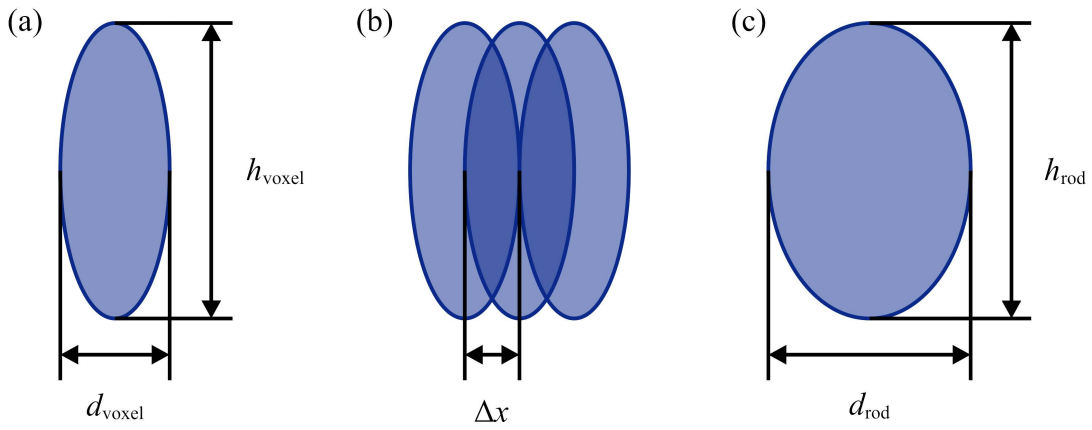

Figure 5.3: Schematical illustration showing how a rod with reduced aspect ratio χ_{rod} is built up from several individual exposures. (a) Rod cross section obtained from a single exposure. (b) Three individual exposures, which are laterally displaced by Δx with respect to each other. (c) Effective rod cross section obtained for the exposure scheme shown in (b).

perimental voxel, which is the basic building block of all structures fabricated by DLW, has a fixed aspect ratio of $\chi_{\mathrm{voxel}} \approx 2.7$ without shaded ring filter and $\chi_{\mathrm{voxel}} \approx 2.0$ with shaded ring filter, which directly translates to the aspect ratio of the rod χ_{rod}, if diffusion of radicals or photoacid as well as shrinkage effects are neglected.
In order to investigate if large PBGs are still supported for these values in a silicon woodpile structure with modified symmetry, gap-midgap ratios have been computed for a bcc silicon woodpile structure in steps of 0.1 for χ_{rod} and in steps of 0.01 for d_{rod}/a in the experimentally relevant range. For comparison, the same has been done for a fcc silicon woodpile. The calculated values are depicted in Fig. 5.2. For the graphical representation as gapmaps a 2D spline interpolation has been performed. The region of small rod diameters d_{rod}/a is marked by the transparent white shaded region to indicate that, as the rods get thinner, the reproducibility of the DLW process and the stability of the obtained structures suffer. In fact, this is not a sharp limit though. For the silicon dielectric constant a value of $\varepsilon = 11.76$ has been assumed. The values $\chi_{\mathrm{voxel}} = 2.7$ and $\chi_{\mathrm{voxel}} = 2$ are marked by the white dashed lines in Fig. 5.2. While significant PBGs can still be obtained for these values in the fcc case, in the bcc case no noteworthy PBG is found at all in the experimentally accessible range for $\chi_{\mathrm{voxel}} = 2.7$, and for $\chi_{\mathrm{voxel}} = 2$, significant PBGs are only found in or very close to the white shaded region. Nevertheless, large PBGs do still exist in the bcc case, but for smaller values of χ_{rod}.

A way to create smaller χ_{rod} values experimentally is by engineering the rod aspect ratio as illustrated in Fig. 5.3. To this end a single rod is built up from multiple exposures which are laterally displaced with respect to each other by a distance Δx, where Δx is below the resolution limit of DLW for the given writing conditions. By choosing the number of individual exposures used for a single rod and the displacement Δx, the rod aspect ratio can be tuned to a PBG-favorable value. This technique has already been employed in [136] in order

to obtain a PBG in a woodpile structure fabricated *via* DLW in chalcogenide glass.
For structures with small lattice constants (roughly below $1\,\mu\mathrm{m}$), however, this technique to engineer the rod aspect ratio only works if the employed photoresist shows sufficiently little proximity effect, as otherwise the structure is overexposed and the rods are not separated any more. In particular, this technique works very well with the photoresist IP-L described in Subsection 4.1.2.

5.1.3 Feature Size Reduction

As already pointed out in the introduction of this chapter, feature sizes and lattice constants required for silicon woodpile structures with a PBG at telecommunication wavelengths are not accessible with DLW in SU-8 that is processed according to the standard protocol described in Subsection 4.1.2. However, in [160] it is suggested that the obtainable feature sizes of photopolymerized SU-8 structures can be reduced by femtosecond optical curing. More precisely, it is demonstrated that rods can be fabricated in SU-8 without the standard post-exposure bake when tightly focused femtosecond nanojoule pulses are used for DLW. This is noteworthy, since the post-exposure bake is usually considered a compulsory step for SU-8 processing, because the exposure alone does not provide a necessary degree of cross-linking and polymerization of the photoresist (see Subsection 4.1.2). In [160] the observation that, under certain conditions, rods can nevertheless be fabricated without this step is attributed to broadband blackbody IR emission from hot, thermally non-equilibrated electrons generated by avalanche ionization in the focal volume, which is then reabsorbed by the SU-8 and acts as a localized post-exposure bake. Since the axial and lateral dimensions of rods fabricated along these lines are stated to be typically twice as small than of those obtained for the standard protocol, femtosecond optical curing of SU-8 offers a promising route to an experimental realization of PBG-materials at telecom wavelengths.

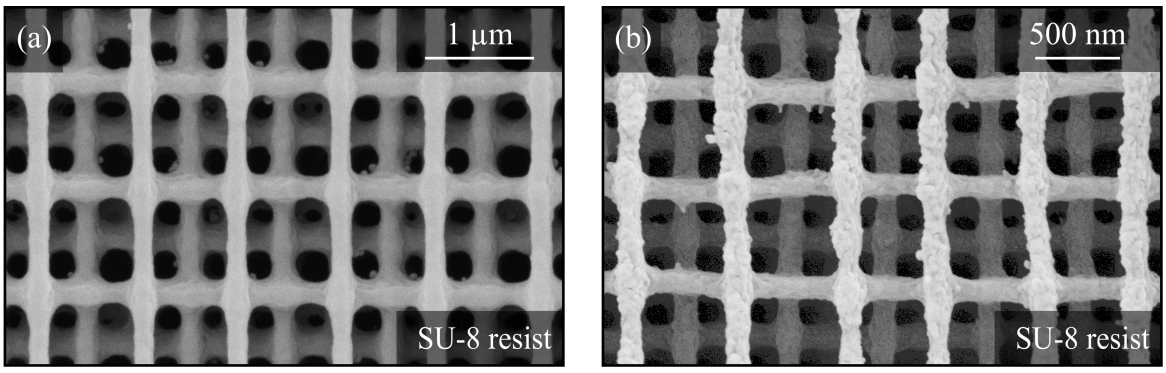

Figure 5.4: Top-view SEM images of typical SU-8 woodpiles. In (a) a template with a lateral rod distance of $1\,\mu\mathrm{m}$ processed according to the standard protocol is depicted, (b) shows a structure with $600\,\mathrm{nm}$ rod distance that has been fabricated without the standard post exposure bake.

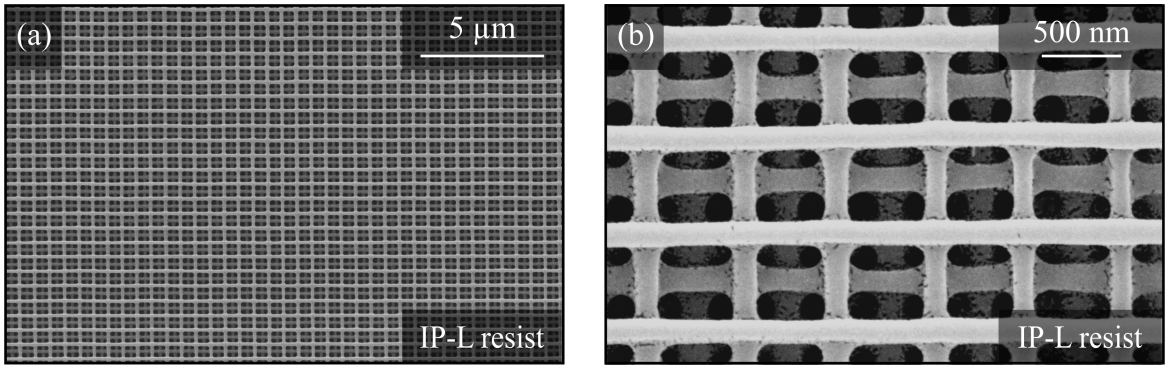

Figure 5.5: Top-view SEM images of $600\,\mathrm{nm}$ rod distance IP-L woodpiles. (a) shows an overview, (b) a magnified view for a different sample. After [134].

The exposure conditions suggested in [160] are fulfilled by DLW Setup 1 described in Subsection 4.1.3, where subpicosecond laser pulses of tens of nanojoules at a repetition rate of 1 KHz are used for DLW. Using this setup, SU-8 woodpile templates with $600\,\mathrm{nm}$ lateral rod distance can indeed be fabricated without a post-exposure bake. The best results are obtained if an additional modification of the standard protocol is made, namely if the duration of the pre-exposure bake is reduced from $1\,\mathrm{h}$ to $50\,\mathrm{min}$. Still, the quality of the obtained samples and the reproducibility of the writing process have turned out to be not satisfactory. Top view scanning electron microscope (SEM) images of typical SU-8 templates are depicted in Fig. 5.4. For comparison, (a) shows a typical SU-8 woodpile structure with a lateral rod distance of $1\,\mu\mathrm{m}$ processed according to the standard protocol. In (b), a woodpile with $600\,\mathrm{nm}$ lateral rod distance fabricated without the post-exposure bake is depicted. From Fig. 5.4 (b) it can be measured that lateral rod widths of less than $150\,\mathrm{nm}$ can be obtained. However, the surface of the rods is very rough and large spatial deviations of the rod diameter are evident. In FTIR measurements such polymer structures exhibit stop bands centered around $900\,\mathrm{nm}$ wavelength, which are shifted towards approx. $1.45\,\mu\mathrm{m}$ after SDI. Due to the low structural quality of such silicon replicated samples, which has been evaluated from focused ion beam (FIB) cross section images (not shown), a PBG is not formed though. Altogether, silicon woodpile structures can indeed be scaled down by leaving out the post-exposure bake during DLW fabrication of SU-8 templates with Setup 1, but poor reproducibility and an insufficient structural quality prevent this approach from achieving a PBG at telecom wavelengths.

Following these unsuccessful attempts using SU-8 with Setup 1, samples have been fabricated using Setup 2 (see Subsection 4.1.3), in combination with the novel commercially available high-resolution photoresist IP-L, which is processed according to its standard protocol (see Subsection 4.1.2). Figure 5.5 shows top-view SEM-images of typical IP-L woodpile templates with a nominal lateral rod distance of $600\,\mathrm{nm}$. Here, a rod is built up from three individual exposures which are laterally displaced by $\Delta x = 60\,\mathrm{nm}$ with respect to each other. Obviously, the spatial uniformity of the rod diameter as well as the achieved surface smoothness of the obtained structures are drastically enhanced compared to the SU-8

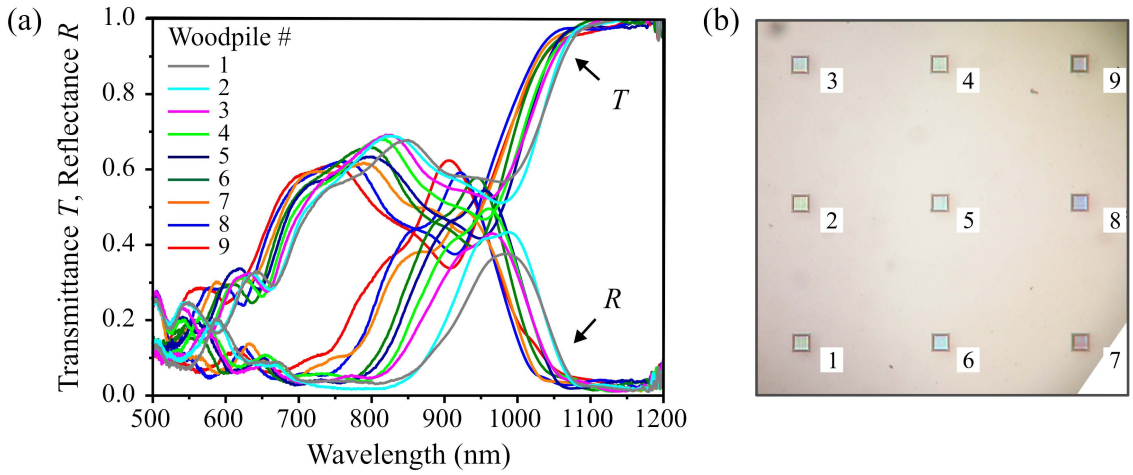

Figure 5.6: (a) Linear-optical reflectance and transmittance spectra for various 600 nm rod distance IP-L woodpile templates with different filling fractions fabricated on a single substrate by DLW. (b) Photograph of the measured structures magnified by an optical microscope, which is used in reflection mode. Taken from [132] with permission from M. Thiel.

templates shown in Fig. 5.4. The small scale roughness on the order of several nanometers, which is visible in Fig. 5.5 (b), stems from gold sputter coating for SEM inspection.
Furthermore, the excellent optical quality of the templates and the good reproducibility of the DLW process are evident from Fig. 5.6 (a), where linear-optical reflectance and transmittance spectra taken with a FTIR-spectrometer are plotted for several such IP-L woodpile templates fabricated on one single substrate [132]. For each of these templates, a pronounced stop band can be measured. Here, woodpiles with different filling fractions have been created by systematically tuning the writing laser power, which results in a gradual shift of the spectral stop band positions. Figure 5.6 (b) exhibits an optical microscope image of the measured samples in reflection mode. Bright colors, which are changing upon filling fraction variation, can be observed, which is another empirical indicator of high sample quality. Hence, the presented IP-L woodpile templates provide a promising starting point for the fabrication of silicon structures with a PBG in the telecom wavelength regime.

5.1.4 Refractive Index Tuning

As the lateral rod distance a of the woodpile templates is reduced, the structures tend to exhibit a larger filling fraction because the axial and lateral dimensions of the rods cannot be made arbitrarily small, yet mechanically stable. As a consequence, the spectral response of the fabricated structures is red-shifted with respect to a theoretically envisioned structure, where the original filling fraction is preserved upon reduction of a. The PBG formed in experimental silicon woodpile structures with approx. 600 nm lateral rod distance is therefore still likely to be positioned at the long-wavelength side of the 1.55 µm telecommunication band.

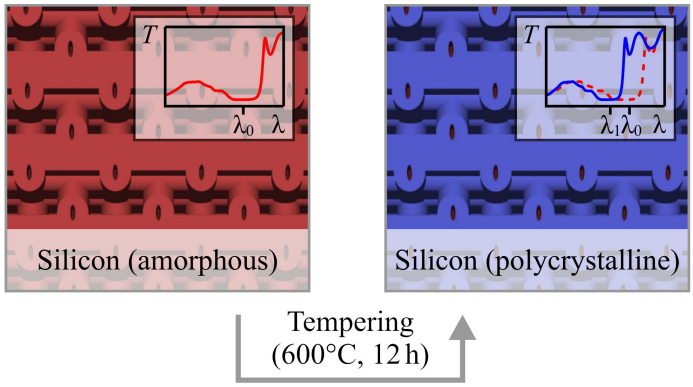

Figure 5.7: Tempering transforms the amorphous silicon (a) from the CVD process into polycrystalline material (b), which exhibits a slightly lower refractive index, while the structural features are preserved by this process. The decrease in refractive index shifts the stop band of the structure to smaller wavelengths, as schematically depicted in the corresponding insets.

Nevertheless, to a certain extent the increase in filling fraction can be compensated by a reduction of the refractive index of the silicon, which causes a blue shift of the spectral response of the structure. Although the size of the PBG is somewhat decreased upon reduction of the dielectric contrast, a slight reduction of the silicon refractive index can be accepted, as long as it is still high enough to allow for the formation of a large PBG in the woodpile structure. Experimentally, a refractive index reduction can be accomplished by tempering of the silicon double inverted structures, which transforms the amorphous silicon from the CVD process into polycrystalline material [161]. While the structural features are preserved by this process as illustrated in Fig. 5.7, the obtained refractive index reduction is on the order of 10%, and the polycrystalline material is furthermore expected to exhibit a lower residual absorption coefficient. In summary, tempering can be introduced as an additional, quality-conserving fabrication step in order to shift the spectral response of a given silicon double inverted structure to smaller wavelengths.

5.2 Experimental Realization

5.2.1 Silicon Woodpiles with a Complete Bandgap at Telecom Wavelengths

In this section, the considerations and ideas discussed in the previous section of this chapter are finally combined in order to experimentally realize silicon woodpiles with a PBG in the telecom wavelength regime.
First, polymer templates like those shown in Fig. 5.5 with a nominal lateral rod distance of $600\,\mathrm{nm}$ and a footprint of $40\,\mu\mathrm{m} \times 40\,\mu\mathrm{m}$ are produced by DLW using Setup 2 with the photoresist IP-L. As before, a rod is built up from three individual exposures which are laterally displaced by $\Delta x = 60\,\mathrm{nm}$ with respect to each other in order to reduce the rod aspect

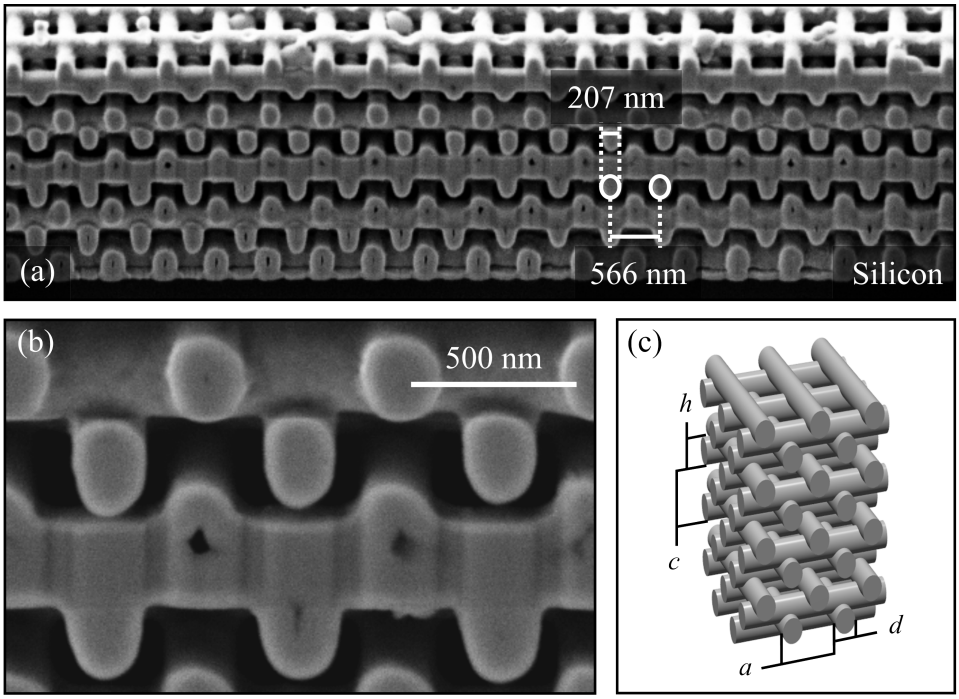

Figure 5.8: Oblique-view FIB cross section images of the fabricated silicon woodpile structure.(a) provides an overview, (b) shows a magnified view. (c) Visualization of the structural parameters. After [134].

ratio χ_{rod}. Next, the templates are double inverted into silicon (SDI) following the procedure described in Subsection 4.2.3.
Figures 5.8 (a) and (b) show electron micrographs of the fabricated silicon woodpile, where focused ion beam (FIB) milling has been performed to reveal the interior of the structure. The viewing angle in Fig. 5.8 is 54 degrees from the surface normal. The structure is composed of 16 intact individual layers, equivalent to 4 lattice constants along stacking direction. From the FIB cross section images the structural parameters of the woodpile have been determined. They are visualized in Fig. 5.8 (c). Owing to polymer and silica shrinkage effects (compare Chapter 4), the actually achieved rod distance is $a = 566\,\mathrm{nm}$. Furthermore, with $c/a = 1.15$ the structures are closer to a bcc than to a fcc woodpile and, as expected from Subsection 5.1.2, the aspect ratio of the rods is reduced from $\chi_{\mathrm{voxel}} = 2.7$, which is the value relevant for Setup 2, to approximately $\chi_{\mathrm{rod}} = 1.46$. For the lateral rod width, a value of $d = 0.365\,a$ is obtained, resulting in a filling fraction of 46.8%. Obviously, the internal structural quality is very good and high uniformity is achieved over a large sample region.

In order to assess its optical quality, the fabricated silicon woodpile structure is characterized with a FTIR spectrometer using a pair of Cassegrain lenses. Fig. 5.9 exhibits linear-optical transmittance spectra of the experimental structure recorded before and after tempering (red dashed and blue solid curve, respectively). As expected for a PBG-material, broad and prominent stop bands can be observed in both cases. Before tempering, that is, for

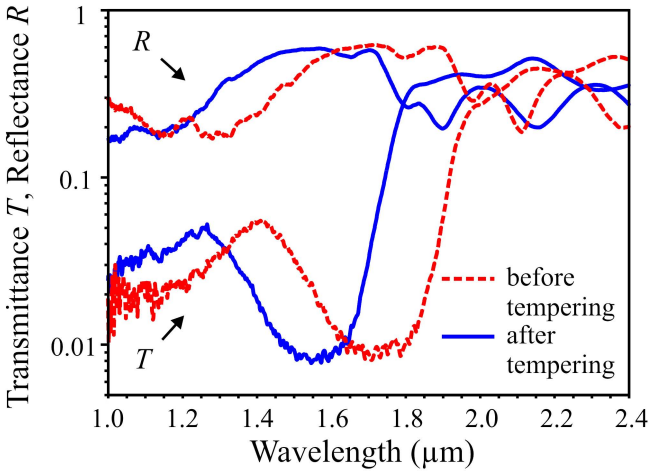

Figure 5.9: Linear-optical transmittance spectra for the fabricated silicon woodpile structure before (red dashed curve) and after (blue solid curve) tempering.

amorphous silicon, the stop band is centered around $1.725\,\mu\mathrm{m}$ wavelength and thus not yet reaching the telecommunication regime. For polycrystalline material, on the other hand, the stop band is blue-shifted to a center wavelength of approximately $1.55\,\mu\mathrm{m}$.
Nevertheless, the mere occurrence of a stop band does not yet imply the existence of a PBG. Therefore, in the following the measured spectra are compared with theoretical calculations, which have been performed for an ideal structure with experimental parameters taken from the FIB cut. The results provide strong evidence that a PBG at telecom wavelengths does indeed exist for the tempered structure.
Measured and calculated linear-optical transmittance and reflectance spectra for the tempered structure are plotted in Fig. 5.10. In these experiments, two different measurement configurations have been employed. First, transmittance and reflectance spectra have been measured using the standard cassegrain optics of the commercial FTIR-spectrometer with an angular spread from 15 – 30 degrees with respect to the surface normal, thus probing many directions in reciprocal space simultaneously. Next, additional transmittance measurements have been performed, in which the angular spread is reduced by an aperture and the sample is tilted such that illumination under a half-opening angle of 0 – 7.5 degrees incidence is achieved (see Section 4.3). In this fashion, the stop band along stacking direction is probed. As expected, the latter configuration leads to a broader transmittance minimum. In both cases an aperture with $8.3\,\mu\mathrm{m}$ on-sample diameter has been used. Under these conditions, the stop band reaches transmittance levels down to about 1%. This value coincides with the transmittance level obtained from a $200\,\mathrm{nm}$-thick opaque gold pad (gray curve in Fig. 5.10 (a)) with about the same footprint $40\,\mu\mathrm{m} \times 40\,\mu\mathrm{m}$ as the woodpiles, indicating that the measurement limit is already reached for the given conditions (compare Appendix B).
The experimental results shown in Fig. 5.10 (a) can directly be compared with calculations depicted in Fig. 5.10 (b). Here, the scattering-matrix approach described in Subsection 4.4.2 has been used. A spatial discretization of $13.02\,\mathrm{nm}$ in propagation direction and the number

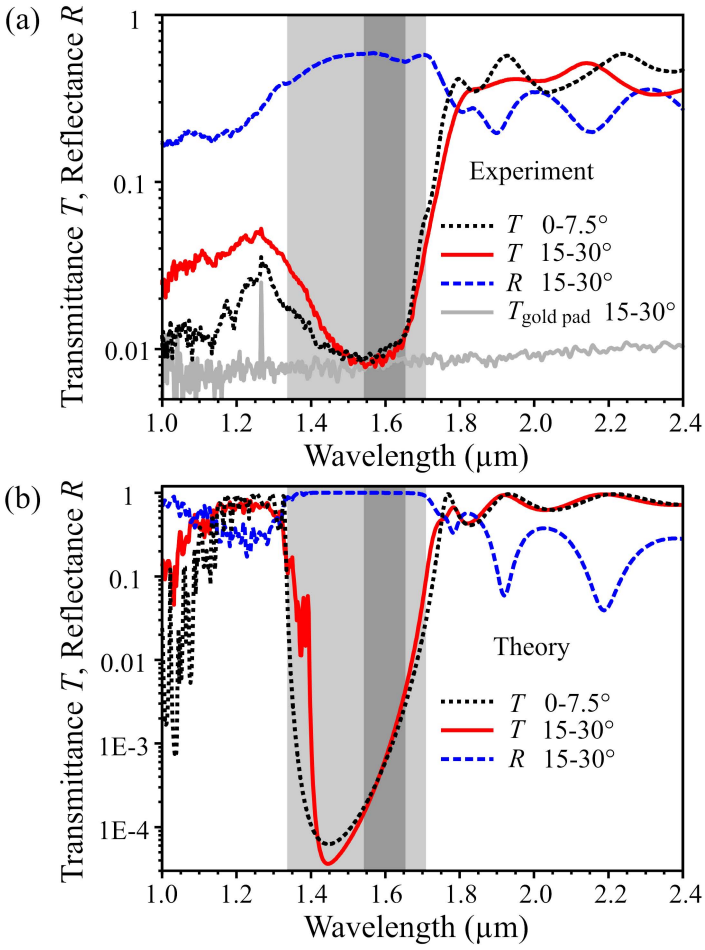

Figure 5.10: Measured (a) and calculated (b) linear-optical transmittance and reflectance spectra for the fabricated silicon woodpile structure. The dark gray region marks the position of the PBG, the light gray region that of the stop band for perpendicular incidence, both of which have been obtained by a band-structure calculation (see Fig. 5.11. Scattering-matrix calculations: S. Essig. After [134].

of 197 Fourier modes laterally lead to convergent results within the linewidth of the plots. To mimic the angular spread of the incident light, spectra are calculated for several incident angles in the respective relevant range and it is averaged over the obtained results. The woodpile structural parameters used in these calculations correspond to the experimental values taken from the FIB-cut. For the silicon dielectric function a value of $\varepsilon = 9.9$ is assumed. This value is intentionally lower than the literature value and effectively accounts for the small air pores in the rods found in the experiment (see Fig. 5.8) that are not explicitly incorporated in the calculations.

Experiment and theory agree well on the edges of the stop band. However, the stop band is deeper in the calculations than in the experiment, where the maximum suppression is determined by the above mentioned measurement limitations, such that the actual depth of the stop band cannot be assessed. Furthermore, deviations are also visible in the air band, that is, in the short wavelength region adjacent to the stop band, for which the experiment

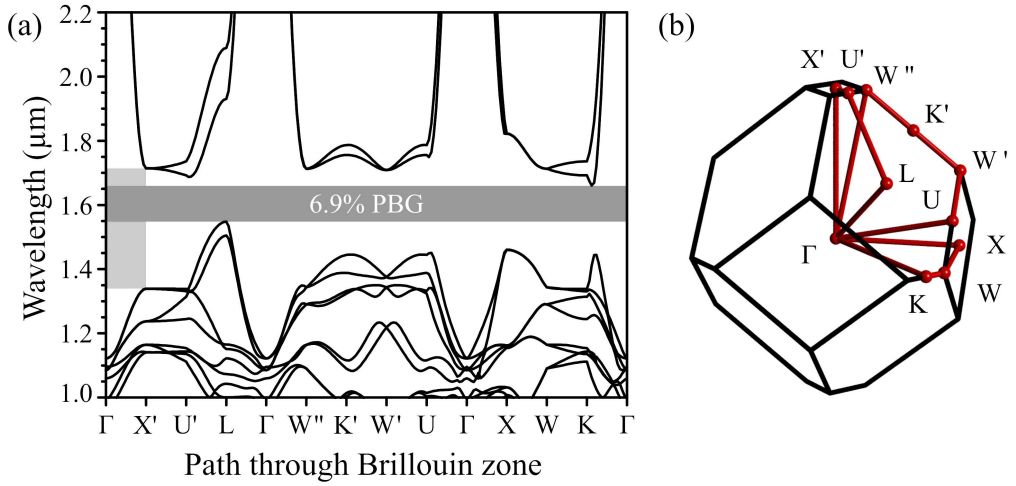

Figure 5.11: (a) Band structure calculation for an ideal woodpile structure using experimental parameters taken from Fig. 5.8. (b) Brillouin zone of the corresponding ct Bravais lattice. After [134].

shows an incomplete recovery of the transmittance. These deviations are very likely due to sample imperfections, like deviations from perfect periodicity and surface roughness (compare Fig. 5.8). The overall quality is, however, comparable to that of previous structures at longer wavelengths [24, 25]. This statement also holds true for the peak reflectance, which is about 60% here and below 70% in [25]. The peak reflectance is strongly influenced by the woodpile surface quality, which is in turn determined by repeated infiltration and reactive-ion etching processes performed during the SDI procedure[1]. For the PBG instead, the bulk quality of the sample is relevant.

Owing to the overall qualitative agreement between experiment and theory in Fig. 5.10, in particular regarding the position and the width of the stop band, it is possible to relate these findings to the photonic band structure. Figure 5.11 (a) shows corresponding results calculated with the MIT Photonic Bands (MPB) package described in Subsection 4.4.1 for identical structure parameters as used in the scattering-matrix calculations depicted in Fig. 5.10 (b). The ct Brillouin zone for $c/a = 1.15$ and its characteristic points are illustrated in Fig. 5.11 (b). The two gray areas aim at connecting the spectra in Fig. 5.10 to the band structure in Fig. 5.11 (a). The dark gray area highlights the photonic bandgap, which is relevant for measurements with large angular spread. The light gray area illustrates the stop band in $\Gamma - \mathrm{X}'$ direction, relevant for strictly normal incidence of light. Both regions agree qualitatively well with the measured stop band positions, providing evidence that the band structure is indeed a reasonable description of the actually fabricated woodpile.

The band structure exhibits a complete photonic bandgap with a gap-midgap ratio of 6.9%. It is centered around $1.6\,\mu\mathrm{m}$ wavelength and includes $1.55\,\mu\mathrm{m}$ at the air-band edge.

[1] Flipping over the sample and performing reflectance measurements on the PhC-substrate interface of the woodpile structure does not offer an alternative, since these measurements are, on the other hand, influenced by small amounts of silicon penetrating under the silica inverse structure during the CVD process (see Subsection 4.2.3).

5.2.2 Reproducibility

In order to demonstrate the reproducibility of this approach and explore the limit of how small the filling fraction can be made without loosing the mechanical stability of the templates, a second sample has been processed along these lines. Figure 5.12 (a) shows measured linear-optical transmittance spectra of this silicon double inverted woodpile structure with 10 intact layers and a footprint of $40\,\mu\mathrm{m} \times 40\,\mu\mathrm{m}$ before and after tempering. In (b), a FIB cross section image of the corresponding structure is shown. Here again, the roughness on the order of few nanometers is due to gold sputter coating needed to characterize the samples with an SEM. For the measurement performed after tempering, the sample is already covered by the sputtered gold layer (approx. $10\,\mathrm{nm}$), which causes an obvious reduction of the transmittance over the entire depicted spectral range. Furthermore, the stop band appears deeper in this measurement than in the previously depicted spectra, since it has been possible to optimize the measurement conditions (see Appendix B) for a more effective background suppression. While the absolute value of the suppression in the stop band cannot

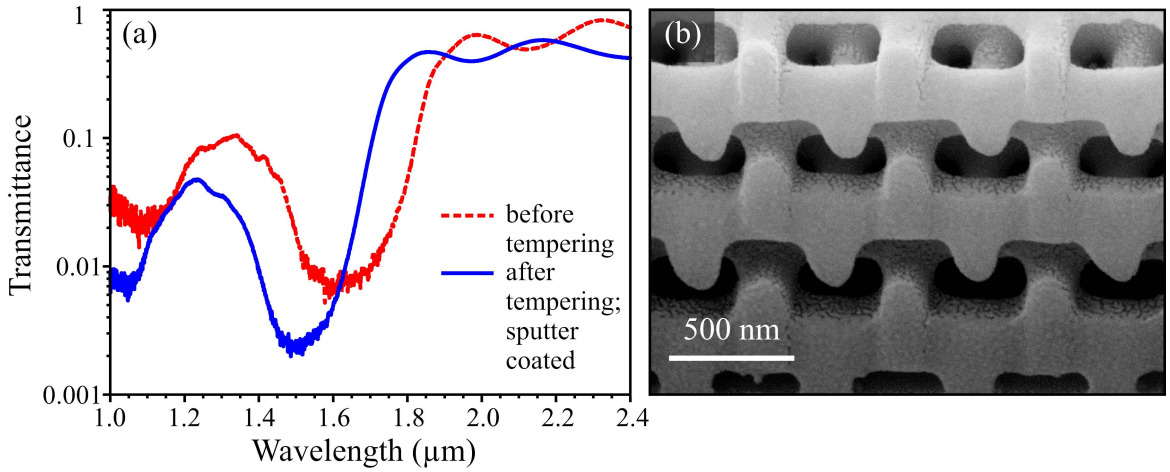

Figure 5.12: Linear-optical transmittance spectra before and after tempering (a), and oblique-view FIB cross section image (b) of a 10 layer silicon woodpile fabricated by DLW and SDI to demonstrate the reproducibility of this approach. For the measurement performed after tempering, the transmittance is reduced over the whole spectral range, because the sample is already covered with a sputter coated gold film for SEM characterization. Furthermore, the stop band appears deeper, because a better background suppression could be achieved by optimization of the measurement conditions. In (b) the viewing angle is 54 degrees.

be interpreted quantitatively because of the sputter-coated gold film, the position of strongest suppression, which is not influenced by the gold, is found at an even smaller wavelengths around $1.5\,\mu\mathrm{m}$ for this sample. This provides evidence that the $1.55\,\mu\mathrm{m}$ telecom wavelength can indeed be comfortably reached by DLW and SDI. The reason for the blue-shift observed for this sample can be attributed to a further decreased c/a-ratio (0.95) and to a smaller filling fraction (39.4%), both of which have been determined from the FIB cross section image. The results of this section give rise to the question, if the short-wavelength limit is already

reached or if it is possible, using DLW and SDI, to fabricate samples with a PBG at even smaller wavelengths. Empirically, using conventional DLW with a writing laser wavelength around $800\,\mathrm{nm}$, neither the dimensions nor the filling fraction of the woodpile structures can be made significantly smaller while at the same time preserving the high quality of the templates. The resulting filling fraction could, however, be reduced during the SDI procedure by re-infiltration of the silica inverse woodpiles with a thin layer of silica prior to silicon infiltration, as already performed in [24]. Alternatively, a reduction of the filling fraction could be achieved by carefully wet-etching the surfaces of the resulting silicon woodpiles. In [162] it is further demonstrated that woodpiles with even smaller rod distances of $450\,\mathrm{nm}$ can be obtained for DLW in IP-L, when a continuous-wave writing laser operating at $532\,\mathrm{nm}$ wavelength is employed. By SDI of such templates, a PBG covering the $1.3\,\mu\mathrm{m}$ telecommunication wavelength is within reach. Ultimately, PBGs at yet even smaller wavelengths will become accessible by SDI of templates obtained *via* stimulated emission depletion (STED) DLW (sDLW) [163], which fundamentally improves the resolution of the writing process. When such sDLW templates are replicated into TiO_2, which is transparent in the VIS, instead of silicon, by use of an appropriate double inversion procedure based on TiO_2-ALD [164], even bandgaps in the VIS spectral region can probably be achieved.

In conclusion, by systematically improving the approach introduced by [24], which is based on DLW and a subsequent SDI procedure, 3D silicon woodpile photonic crystals with a PBG that includes the $1.55\,\mu\mathrm{m}$ telecommunication wavelength have been fabricated, thus demonstrating that the technologically most relevant wavelength regime can be accessed by this approach. Taking this result a starting point, the following chapters are devoted to the introduction of functional elements into PBG-materials using DLW and SDI.

Chapter 6

Functional Defect Design

In Chapter 3 the choice of the woodpile structure as host PBG-material for the introduction of functional defects has already been motivated. Given this choice, appropriate cavity and waveguide designs have to be found which are compatible with all necessary fabrication steps, compact enough to be treated numerically, and which provide the desired optical functionalities of localization and guiding of light, respectively.
In this thesis, the idea is to design one basic defect element which can then be arranged or concatenated with several other such elements to form cavities, waveguides, or even much more complex defect architectures. The corresponding design process is described in the first part of this chapter. Following this, the optical properties of a point defect cavity and a line defect waveguide based on the developed design are investigated numerically. Finally, experimental proof is provided that the proposed design is compatible with fabrication *via* DLW and SDI. Thereby different approaches for defect introduction are explored.

6.1 A Basic Defect Element

In order to develop a design for a basic defect element, which can then act as a fundamental building block to create more complex structures, first the constraints imposed by the fabrication process and by the demand to perform numerical calculations have to be analyzed in more detail.
As pointed out before in Section 4.1, DLW is a very flexible technique, which therefore largely maintains the design freedom. One has to keep in mind, however, that the basic building block of all structures written by conventional DLW is an ellipsoidal voxel and that the written structures have to be mechanically stable. In particular, "flying features" cannot be realized. Less obviously, the developer for the photoresist has to be given channels to penetrate into all the unexposed regions, and finally, polymer shrinkage effects have to be taken into account as well.
SDI, in contrast, noticeably limits the design freedom. The reason is that this technology relies on infiltration techniques, which suffer from the inherent problem of bottleneck formation. The creation of a bulk volume of additional dielectric inside the 3D PhC can therefore only be accomplished in some special cases. The introduction of air or compound de-

fects (see classification of different defect types in Subsection 2.3.3) is therefore much more amenable to fabrication by DLW and SDI than the creation of dielectric defects, which are thus not further considered in the following.
The demand to perform numerical band-structure and scattering-matrix calculations for the resulting defect structures further narrows down the number of suitable design options. In the context of supercell calculations it is favorable if the defect is confined to approximately one unit cell. If, instead, the defect spans several unit cells, the corresponding supercell has to be chosen larger, which is computationally more expensive (compare Section 4.4) and convergent results cannot be achieved in reasonable computational time with the available computational resources.
Still, even when taking all mentioned constraints into account, there are several possibilities left to introduce a basic defect element into the woodpile structure. This remaining design freedom can now be used to tailor the optical properties of the created photonic structures. A general design objective regarding the optical properties of air defects is to avoid the formation of surface modes, which are undesirable as they will strongly scatter in the presence of disorder. In Ref. [165] an empirical design rule has been introduced for this purpose in the context of air-core waveguides in 3D PhC. The procedure involves examining the band-edge mode profiles of the undisturbed PhC at the center of the Brillouin zone, locating the regions of maximal electric-field intensity and placing the air defects such that they enclose these regions. While keeping all other design constraints in mind, this rule has been applied to the

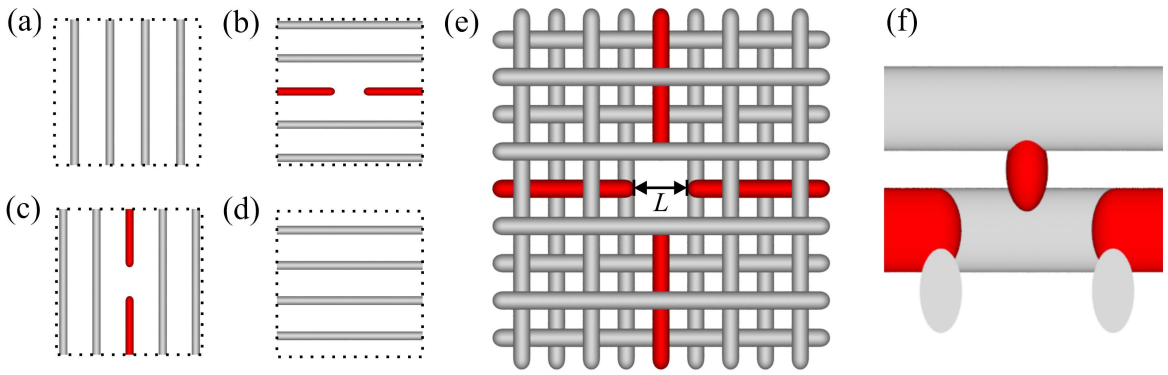

Figure 6.1: Sketch of a basic defect element design compatible with the listed constraints. In (a)–(d), four layers (one stacking sequence) of a woodpile structure with the defect rods in the second and third layers are depicted separately and in consecutive order. Top and side-views of the assembled sequence are shown in (e) and (f), respectively. Defect rods are marked in red.

woodpile model system specified in Subsection 3.1.2. In this case, the maxima of electric-field intensity at the Γ-point are located inside or directly adjacent to the small volume where two elliptical rods overlap. Instead of removing a part of a single rod, the concept described in Ref. [165] therefore suggests to remove an entire rod crossing point, thereby not cutting through but enclosing the high-intensity regions in the removed volume. A basic defect element based on these considerations can be formed by discontinuing two rods symmetrically to their former overlap, as shown in Fig. 6.1. The construction scheme is depicted in (a)–(d),

while (e) and (f) shows the assembled stacking sequence. The length of the removed rod sections is denoted by L. The kind of defect that is created by embedding such basic defect elements into a woodpile structure depends on their arrangement. For example, by placing one element in an isolated manner, a point defect cavity is formed, and by placing several of such elements in a row, a linear waveguide is created. For these two particular cases, the expected optical properties will be investigated in the following two sections.

6.2 Model System of a Point Defect

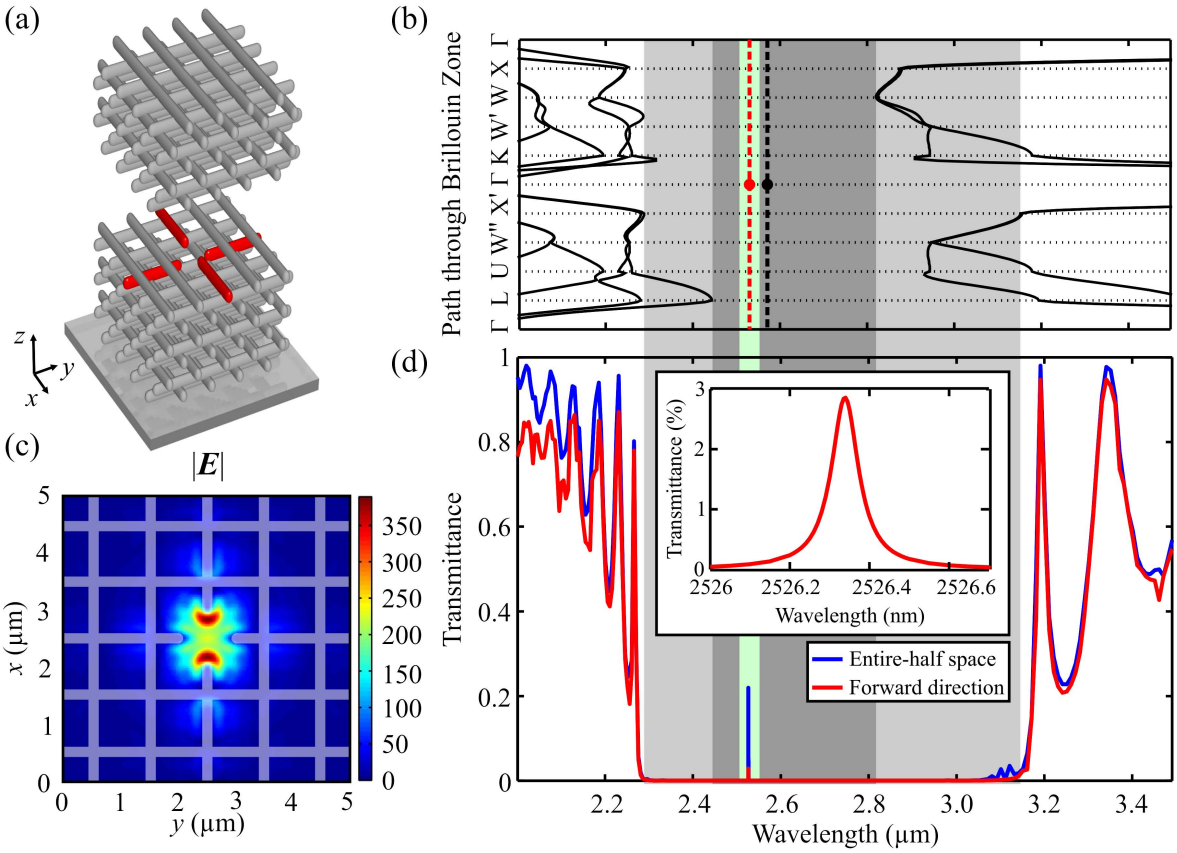

Figure 6.2: (a) Schematic of the 3D point defect cavity design. (b) Cavity mode frequencies (red and black dashed) calculated at the Γ-point plotted together with the band structure of the perfect crystal. (c) Numerical calculation of the mode profile. The light blue structure represents the distribution of the silicon and acts as a guide for the eyes. (d) Perpendicular incidence transmittance spectra for x-polarized light into the forward direction (red solid curve) and into the entire-half space (blue solid curve) of a structure containing one cavity in the supercell. The inset is a close-up of the transmittance into the forward direction. Scattering-matrix calculations: S. Essig. After [123].

The first case to be investigated here is that of a point defect cavity formed by introducing a single basic defect element into the woodpile structure. This situation is illustrated in

Fig. 6.2 (a), where the defect rods are again marked in red and the upper part of the woodpile structure has been elevated in order to reveal the defect inside. Band-structure and scattering-matrix calculations have been performed for this defect-containing fcc woodpile structure using the parameters of the fcc model system introduced in Subsection 3.1.2 ($a = 1\,\mu\mathrm{m}$, $c = \sqrt{2}\,a$, $d = 0.25\,a$, $\chi = 2$, $\varepsilon = 11.76$) and a defect length of $L = 0.75\,a$. The corresponding mode frequencies and theoretical spectra are displayed in Fig. 6.2 (b)-(d). The frequencies of the defect modes (red and black dashed) shown in (b) have been computed at the Γ-point using a $5 \times 5 \times 3$-supercell and are depicted together with the band structure of the perfect crystal. The supercell is chosen to match the in-plane (perpendicular to stacking direction) size of the 3D-periodically continued supercell needed for the band-structure calculation to the size of the 2D-periodically continued supercell used for scattering-matrix calculations (see below), while fixing the volume of the 3D-periodically continued supercell to a numerically treatable size. Owing to the presence of the defect, two modes are shifted into the PBG, one of which is twofold degenerate. The degenerate mode is located at $2,530\,\mathrm{nm}$, the non-degenerate mode at $2,571\,\mathrm{nm}$. For comparison, if a symmetrical $4\times4\times4$-supercell is used, the degenerate mode is found at almost the same position ($2,534\,\mathrm{nm}$), but for a $3 \times 3 \times 3$-supercell, where coupling effects are still significant, it is shifted to $2,508\,\mathrm{nm}$. Throughout the right hand side of Fig. 6.2, the dark gray area indicates the region of the PBG (14.3% gap-midgap ratio), the light gray area marks the stop band for strictly perpendicular incidence ($\Gamma - \mathrm{X}'$-direction), and the light green area highlights the position of the degenerate cavity mode.

Corresponding scattering-matrix calculations have been conducted using a 5×5-supercell and 1,185 Fourier modes. Fig. 6.2 (c) shows a cross section of the calculated mode-profile for one of the two degenerate cavity modes (red dashed in Fig. 6.2) excited by linearly polarized incident light, where the electric field is oriented parallel to the x-axis. The host woodpile structure is placed on a glass substrate with refractive index 1.5 and has an overall thickness of 22 layers, whereas the defect is situated in layers 11 and 12 (see Fig. 6.2 (a)). The modulus of the field amplitude is shown in a z-plane at the center of the defect between layers 11 and 12. On resonance, the field enhancement is roughly a factor of 350 (corresponding to an intensity enhancement of 122,500). The second degenerate mode can be excited with an incoming polarization parallel to the y-axis, and the resulting field distribution will be oriented along the y-axis.

Calculated linear-optical transmittance spectra for the defect mode excited by x-polarized light are shown in Fig. 6.2 (d). The fundamental stop band centered at approx. $2,700\,\mathrm{nm}$ wavelength is clearly visible. Here, the blue curve depicts transmittance in all calculated orders, the red curve in forward direction only. In both curves the signature of the doubly degenerate defect mode can be observed as a sharp peak located at $2,526\,\mathrm{nm}$. The spectral position of this peak nicely agrees with the position of the degenerate defect mode found in the band structure calculation (below 2 ‰ deviation). A close-up of this peak is shown in the inset of (c). From this peak, a theoretical quality factor of the defect mode of $Q \approx 30,000$ is derived. This value can be increased further by increasing the amount of cladding layers. As discussed in Subsection 2.3.4, even infinitely large quality factors can be reached for infinitely extended samples, in sharp contrast to 2D photonic crystal slabs, where the quality

factor stays finite (albeit large). The non-degenerate defect mode (black dashed in Fig, 6.2) revealed by the band-structure calculation cannot be seen in the transmittance calculations due to a symmetry mismatch between plane-wave excitation and mode profile under perpendicular incidence. It can, however, be excited for oblique-incident light, which has been verified by corresponding scattering-matrix calculations (not shown).

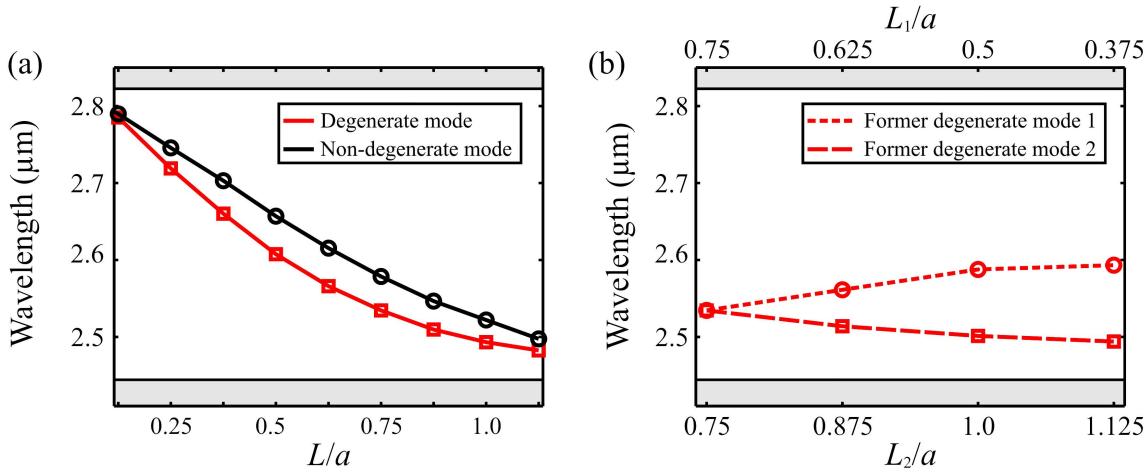

Figure 6.3: (a) Cavity mode frequencies for various cavity lengths L. (b) Mode frequencies of the former degenerate mode for differently chosen intersection lengths L_1 and L_2. The gray areas indicate the position of the edges of the PBG.

In order to study the behavior of the cavity modes upon parameter modification, additional band-structure calculations have been performed. In a first set of calculations, the length of the removed rod section has been varied symmetrically for both defect rods. The results are summarized in Fig. 6.3 (a), where the cavity mode frequencies are plotted as a function of the defect length. By a second set of calculations it is shown that the degeneracy of the mode plotted in red in Fig. 6.3 (a) can be lifted by an asymmetric cavity design, where the lengths of the two removed rod sections denoted by L_1 and L_2 are chosen differently. These results are depicted in Fig. 6.3 (b). Finally, band structure calculations have been carried out for the original defect design with $L = 0.75\,a$, but now using a different host material, namely a bcc woodpile structure with the parameters specified for the bcc model system in Subsection 3.1.2 ($a = 1\,\mu\text{m}$, $c = a$, $d = 0.25\,a$, $\chi = \sqrt{2}$, $\varepsilon = 11.76$). In this case, the same qualitative behavior is found regarding number and degeneracy of the modes shifted into the PBG (not shown).

6.3 Model System of a Line Defect

In the last section a point defect cavity was created by placing one isolated basic defect element into the woodpile structure. A straight vertical waveguide can instead be formed by placing several of these basic defect elements directly on top of each other in stacking

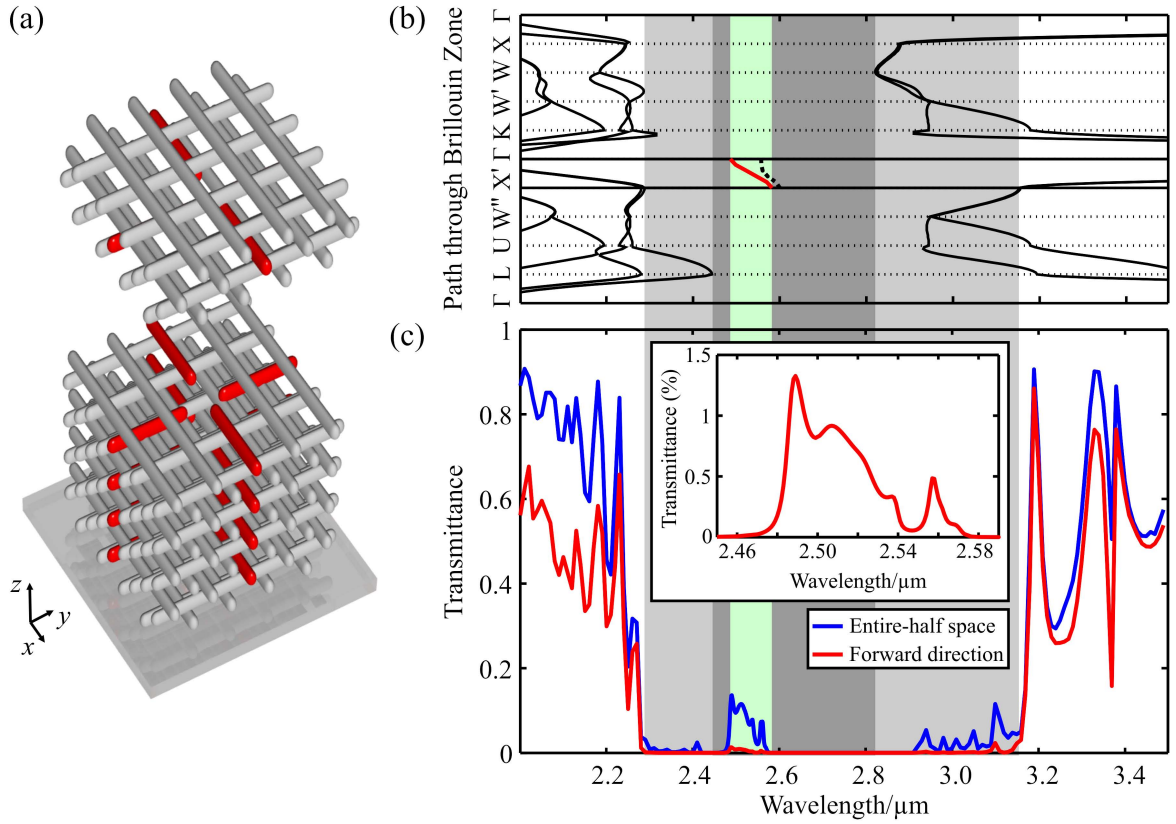

Figure 6.4: (a) Sketch of the 3D line defect waveguide design. (b) Waveguide dispersion relation (red and black solid curves) in woodpile stacking direction ($\Gamma - \mathrm{X}'$), depicted together with the band structure of the perfect crystal. (c) Perpendicular-incidence polarization-averaged transmittance spectra for the waveguide-containing woodpile structure into forward direction (red solid curve) and into the entire-half space (blue solid curve). The inset is a close-up of the transmittance into the forward direction. Scattering-matrix calculations: S. Essig.

direction, as illustrated in Fig. 6.4 (a), where the upper part of the woodpile has again been elevated to provide a better view of the waveguide. In this way one arrives at a design similar to that investigated in Refs. [13, 21] for woodpiles with non-overlapping rectangular rods (see Fig. 3.6 (g)). In the following the theoretical optical properties of this waveguide are studied by corresponding band-structure and scattering-matrix calculations. Analogously to the previous section, an intersection length of $L = 0.75\,a$ and woodpile parameters of the model system introduced in Subsection 3.1.2 ($a = 1\,\mu\mathrm{m}$, $c = \sqrt{2}\,a$, $d = 0.25\,a$, $\chi = 2$, $\varepsilon = 11.76$) are assumed. The waveguide dispersion calculated for propagation in stacking direction ($\Gamma - \mathrm{X}'$) is displayed together with the band structure of the perfect PhC in Fig. 6.4 (b). Here, a 5×5-supercell has been used[1]. Again two modes (red solid and black dashed curves in Fig. 6.4) are shifted into the PBG, where the one at smaller wavelengths is twofold degenerate. This degenerate mode, which is highlighted by the light green area

[1] Actually, a $5 \times 5 \times 1$-supercell is employed in the calculation. Since for waveguide structures the supercell size in waveguide direction is always one, this information is skipped in the following.

throughout the right hand part of Fig. 6.4, can also be found in corresponding theoretical transmittance spectra depicted in Fig. 6.4 (c), where it shows up as a broad peak in the stop band. Spectra have been calculated both for x and for y-polarized light. Here, the blue curve depicts polarization averaged transmittance into the entire half space and the red curve into forward direction only. In these calculations, a 5×5-supercell and 1,185 Fourier modes are used. The computed structure is placed on a glass substrate (refractive index $n_{\mathrm{glass}} = 1.5$) and consists of 22 layers with defects situated as depicted in Fig. 6.4 (a). Excitation of the non-degenerate mode is again forbidden by the mode symmetry under these conditions. For the degenerate mode a bandwidth of $96.9\,\mathrm{nm}$ is derived from the dispersion diagram, corresponding to a band-midband ratio of 3.8%. The single-mode bandwidth of this waveguide mode is reduced by the presence of the non-degenerate mode to a value of $71.7\,\mathrm{nm}$. Furthermore, the degeneracy of this mode allows for polarization independent light propagation along the waveguide.
By additional band-structure calculations (not shown) it has been verified that the midband position of this mode can be adjusted by variation of the waveguide cross section and that its degeneracy can be lifted by introducing an asymmetry, as already the case for the point defect cavity. Moreover, the same waveguide design has also been investigated for a bcc woodpile structure with the bcc model system parameters specified in Subsection 3.1.2 ($a = 1\,\mu\mathrm{m}$, $c = a$, $d = 0.25\,a$, $\chi = \sqrt{2}$, $\varepsilon = 11.76$) by corresponding band-structure calculations (not shown). Again, the same qualitative behavior as for the fcc case is found regarding number and degeneracy of the modes shifted into the PBG, such that both the fcc as well as the bcc woodpile structure are identified as proper host PBG-materials for the introduction of this kind of waveguides.

6.4 Fabrication of Designed Defect Structures

In the last two sections it has been found that the basic defect element introduced in Section 6.1 can be arranged to create both a resonant cavity supporting localized modes in the PBG as well as a vertical waveguide supporting guided modes. Yet, it has to be demonstrated experimentally that the design proposed for this basic element is indeed compatible with fabrication by DLW and SDI. This is done in this section, where different fabrication possibilities are explored.

For the intrinsic introduction (see classification in Section 3.3) of designed defects into the 3D PhC by DLW and SDI, the defect elements have to be introduced already at the very first step of the fabrication procedure, that is, during the DLW process. This results in defect-containing polymer templates, which are then transformed into silicon structures by SDI without any additional effort compared to an undisturbed woodpile structure.
In the writing process, the creation of defects according to the previously proposed design is accomplished by switching off the writing laser for the time it takes the piezo scanning stage to move over the defect site. There are different ways how this can be implemented.

One way is to stop the piezo scanning stage at the positions of the rod endings (beginnings), not switching off (on) the writing laser until the respective target position is reached. The advantage of this method is that, by allowing the piezo scanning stage to stop, points can be approached with high accuracy, which translates to an exact defect positioning and alignment. However, upon acceleration and deceleration of the piezo scanning stage the local exposure dose deposited by the writing laser is changed, which translates into variations of the rod diameter, such that typically the ends of the rods are thickened if no countermeasures are taken. A way to overcome this problem is by use of the "Perfect Shape" technology provided by the Nanoscribe software. It is based on a semi-empirical approach, which approximates the velocity behavior of the piezo scanning stage and can be tuned by four independent parameters in order to keep the deposited dose constant at the rod endings.

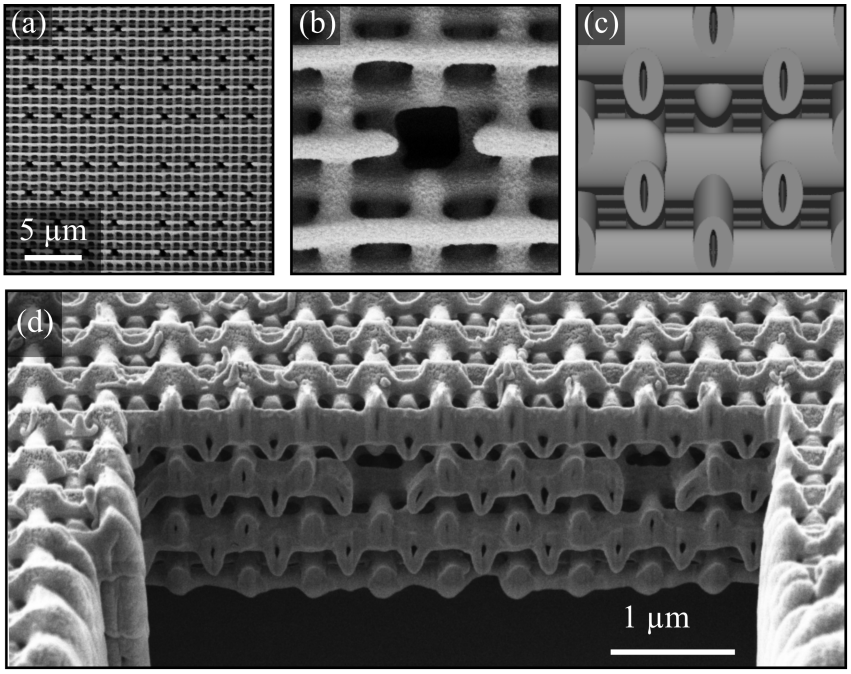

Figure 6.5: SEM-images demonstrating the feasibility of defect introduction by stopping the piezo scanning stage at each rod ending position during the writing process of the woodpiles. (a) Top-view image of a woodpile PhC hosting several defects in its top-most layers. In (b) a magnified view of a single defect is displayed. (c) Schematic representation of the cavity design after SDI. (d) Oblique-view FIB cross-section image revealing two cavities inside a silicon PhC. After [123].

In order to demonstrate the feasibility of this approach, two sets of polymer templates are fabricated. In the first set, two defect layers are placed on top of the woodpile structure for scanning electron microscope inspection. In these experiments, the photoresist SU-8 is used and DLW is performed using Setup 1 described in Subsection 4.1.3. Corresponding results are depicted in Fig. 6.5 (a)–(b). In (a), a top view of the defect layer is displayed, where four fields with 16 defects each are clearly visible. The close-up in (b) demonstrates the high fidelity of the defect design for appropriate parameters. The intersection of the rods is nicely centered, and no obvious widening of the rod diameter is visible at the rod endings. The

depicted woodpile structures have a nominal rod spacing of $a = 940\,\mathrm{nm}$. Next, a second set of polymer templates is fabricated with the defects buried deep inside the 3D PhC, in order to demonstrate that conversion into silicon is actually possible for the proposed defect design. Again the photoresist SU-8 is used, the writing process is performed using Setup 2 (see Subsection 4.1.3). Figure 6.5 (d) depicts a corresponding experimental 3D structure after silicon double-inversion. Here, a FIB cross-section image is shown, which reveals two cavities embedded inside the silicon double-inverted woodpile. The obvious voids inside the rods stem from bottleneck formation during the silicon CVD process (see Subsection 4.2.3). The experimental realization comes very close to the sketch of an ideal structure shown in Fig. 6.5 (c), which nicely demonstrates the feasibility of this fabrication approach.

Nevertheless, by stopping the piezo stage at every defect site the writing process is considerably slowed down. Therefore a second possibility to implement the writing of the defects is tested, which is to switch off the writing laser "on the fly", while the piezo stage is moving at its unaltered writing speed. Depending on the number of introduced defects, the writing time is drastically reduced by this approach compared to the previous solution, where the piezo scanning stage comes to a halt at each single rod ending. Furthermore, for this implementation, the thickening of the rod endings is not an issue any more, because accelerations and decelerations of the piezo scanning stage do not take place any more at the defect sites. However, the challenge is now transferred to the proper alignment of the missing rod sections with respect to the surrounding lattice. Here, the difficulty is caused by non-linear deviations, which occur between the nominal and the actual positions of the piezo scanning stage while it is in motion, and which can amount to several micrometers of displacement. In order to achieve a proper alignment despite these deviations, a readout of the actual piezo position as a function of specified piezo position is performed prior to the writing process. This relation can then be inversely evaluated to derive the nominal defect positions that have to be specified in the DLW coordinate file in order to place the defects at their correct positions in the fabricated structure. Taking an additional constant empirical offset into account, a precise alignment of the missing rod sections becomes possible.

This is demonstrated by Fig. 6.6 (a) and (b), showing top-view SEM images of a first set of polymer-woodpile templates, where several basic defect elements are incorporated into the woodpiles' top layers. The nominal rod distance of the host woodpile structure is 900 nm. An entire field of basic defect elements is depicted in (a), a close-up of one such element is displayed in (b), demonstrating that a very good alignment of the removed rod sections is obtained. A slight deformation of the surrounding woodpile lattice can be observed, which is due to polymer shrinkage pulling the endings of the discontinued rods away from the defect site.

Again, a second set of templates is fabricated with the defects buried inside the bulk of the woodpile structures, which is then subjected to a SDI procedure. In Fig. 6.6 (c) and (d) examples for the successful silicon replication of a point defect cavity and a vertical waveguide, respectively, are displayed. Again, the host woodpile structures have a nominal rod spacing of 900 nm. In both cases a high structural quality in the defect region as well as in the surrounding woodpile material is achieved. For SDI of the waveguide-containing woodpile

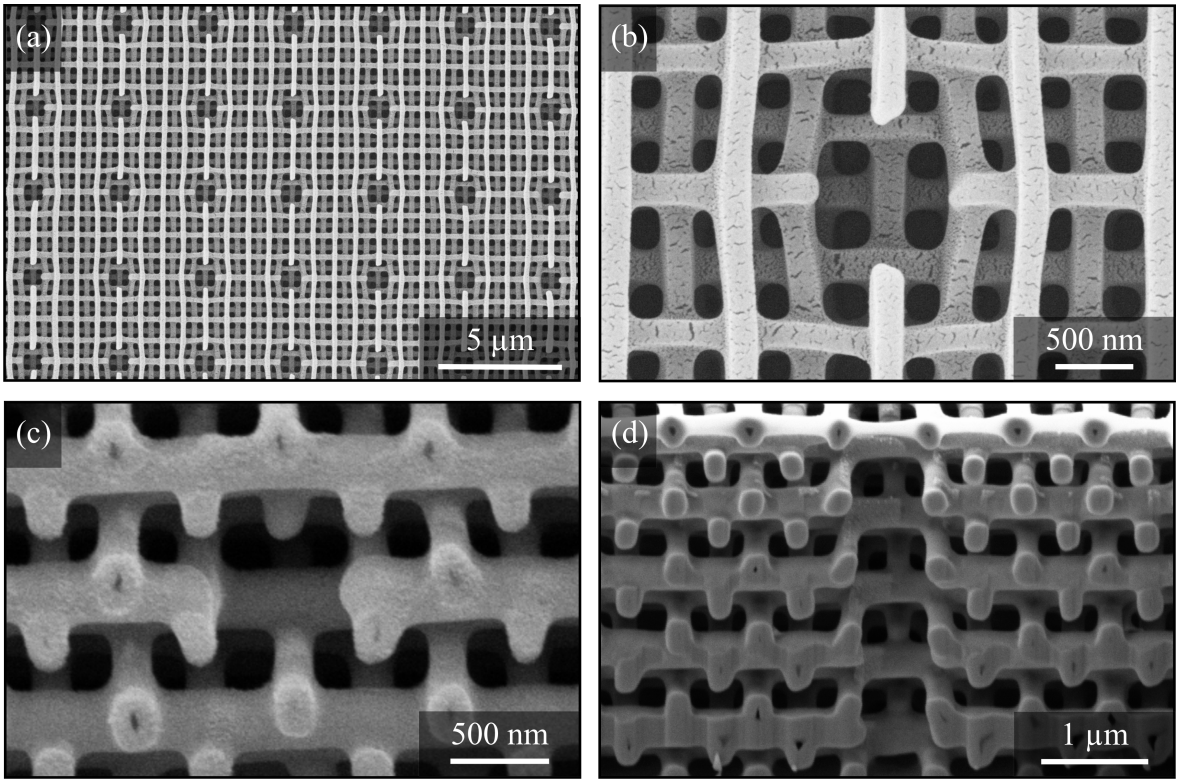

Figure 6.6: Electron micrographs of defect structures introduced by switching off the writing laser for a defined moment at each defect site, while the piezo scanning stage keeps on moving at unaltered speed. (a) and (b) show top-view images of IP-L woodpile structures with defects in their top-most layers. In (a) an entire field of cavities is displayed, (b) depicts a magnified view of the defect region. The small-scale roughness visible in (b) stems from sputter-coated metallization for SEM observation. (d) and (e) show oblique-view FIB cross-section images of a cavity and a straight vertical waveguide, respectively, embedded inside silicon double inverted woodpile PhCs.

structures, two particularities have to be taken into account: First, the silica thickness deposited during the ALD process has to be chosen larger than for an undisturbed woodpile template (compare Subsection 4.2.3), at least $(a - d)/2$, in order to completely infiltrate the entire defect region with silica. Second, and connected to the first aspect, to completely remove the bulk block of silica inside the defect channel in the last fabrication step of the SDI procedure, the HF wet-etching durations have to be increased (approximately doubled) for the waveguide-containing structure compared to a bare woodpile. All structures shown in Fig. 6.6 are written using the photoresist IP-L with Setup 2 (see Subsection 4.1.3).
A completely different, extrinsic method (see classification in Section 3.3) to introduce defects into PhCs fabricated by DLW and SDI shall not remain unmentioned here. By FIB milling into an undisturbed silicon double inverted woodpile structure, vertical waveguides according to the design scheme proposed in Section 6.3 can be realized. Figure 6.7 (a) and (b) show top-view SEM images of vertical waveguides milled into a woodpile structure with nominally $600\,\mathrm{nm}$ lateral rod distance. Roughness and periodic diameter variations of the

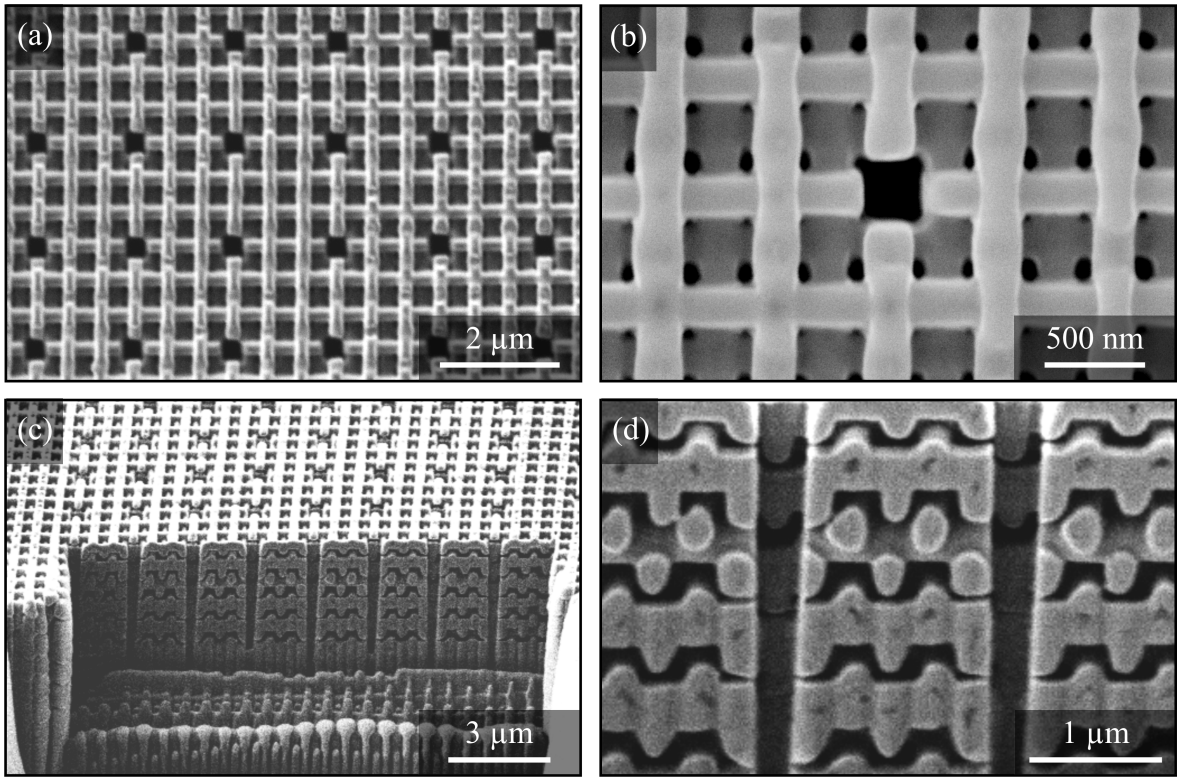

Figure 6.7: SEM-images of linear vertical waveguides introduced by FIB milling into a silicon double inverted woodpile structure with lateral rod distances of approximately $600\,\mathrm{nm}$. (a) Top-view image of an array of waveguides with an intersection length of $L \approx 300\,\mathrm{nm}$ arranged in a 3×3-supercell, (b) shows a close-up of a single waveguide structure. (c) Oblique-view FIB cross-section images revealing the interior of a 3×3-supercell array of waveguides with an intersection length of $L \approx 436\,\mathrm{nm}$ in the top defect layer, which narrows down to $302\,\mathrm{nm}$ in the bottom layer. In (d) a close-up is displayed. FIB milling: P. Brenner

rods belonging to the topmost woodpile layers stem from repeated reactive ion etching and infiltration processes performed in the course of the SDI procedure. In (c) and (d), oblique-view FIB cross-section images are depicted, which reveal the interior of another fabricated structure with increased waveguide cross section. For milling of the defects, a Zeiss XB 1540 (cross beam) operating with gallium ions is used at an acceleration voltage of $30\,\mathrm{kV}$ and a milling current of $50\,\mathrm{pA}$. In order to make the sample conductive, it has previously been coated with a transparent film of indium-tin-oxide (ITO), that is obtained by electron beam evaporation and subsequent tempering for $12\,\mathrm{h}$ at $450^{\circ}\mathrm{C}$. The arrays of vertical waveguides are defined using the pattern generator provided by the software of the instrument. As obvious from the images, a precise positioning and size control can be achieved by this technique even for these small feature sizes, and additionally, no polymer shrinkage effects, that might lead to deformations in the defect area for the intrinsic method, have to be taken into account at all. From Fig. 6.7 (d), small artifacts introduced by the milling process can be observed: the inclinations of the side walls are measured to lie between 0.4 degrees and 3 degrees, and

the cross sections of the rods adjacent to the waveguides appear slightly increased compared to those of the other rods. This can be attributed to material deposited at the rod surfaces during the milling process. Still, this method provides a powerful platform for basic research on waveguides in 3D PhCs, because it allows for optical reflectance and transmittance measurements on one and the same woodpile structure before and after milling, that is, with and without defects, or even with gradually increased defect densities, thereby making a direct assignment of changes in the spectrum to the presence of the defects possible. Such measurements have been performed for the depicted structures, however, since the host woodpile structure used for this proof-of-principle experiment does not possess a PBG, a mere deterioration of the stop band with increasing defect density has been observed.

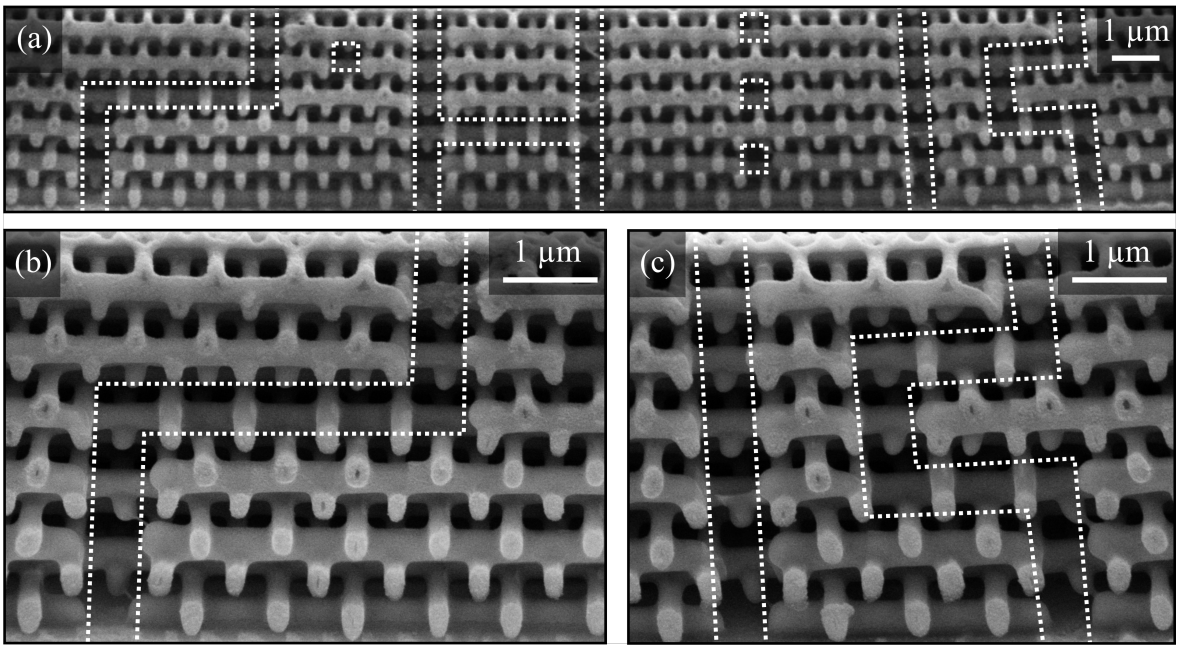

Figure 6.8: Electron micrograph of a variety of cavity and waveguide structures (from left to right: a doubly bent waveguide, an isolated cavity, three interconnected waveguides, a coupled resonator optical waveguide consisting of three cavities, a straight vertical waveguide, a fourfold bent waveguide) embedded in a single silicon woodpile: (a) shows an overview, (b) and (c) are close-ups of selected elements. After [135].

In this thesis the extrinsic approach has not been pursued further for two reasons: First, when thinking about applications, the process itself is less attractive compared to the intrinsic method due to the additional fabrication step, which requires a FIB and an alignment procedure, and second, the accessible geometries are limited to straight vertical waveguides only. The other way around, the intrinsic fabrication method is favored because it is based on two comparably inexpensive table-top technologies and because of its high flexibility. In order to actually verify this claim of high flexibility experimentally and to provide an impression of the level of complexity that is within reach of this fabrication approach, a single

woodpile structure containing a complex defect network has been realized in silicon using the fast defect writing approach, where the piezo scanning stage is not stopped at the defect sites. Inside this structure, numerous basic defect elements are arranged to form isolated and coupled cavities as well as straight, bent, and interconnected waveguides. A FIB cross-section image of a significant portion of this network is shown in Fig. 6.8 (a), the close-ups displayed in (b) and (c) aim at demonstrating the high quality of the fabricated structures. Huge supercells would be needed for calculation of the theoretical optical properties of such a system using the scattering-matrix method, which is not possible with reasonable computational resources at the current state of the art. Novel approaches, based, *e.g.*, on 3D Wannier functions, might provide a future route to efficiently treat such systems numerically and allow for an investigation and optimization of their optical properties.

To wrap up this chapter, a basic defect element design has been proposed and it has been demonstrated theoretically, that the two fundamental functionalities of localizing and guiding light inside a 3D PBG-material are supported by this design. Furthermore, the feasibility of this design regarding fabrication by DLW and SDI has been verified experimentally.
Nevertheless, in order to assess the actual optical functionality of the fabricated photonic structures, a characterization *via* SEM inspection has to be complemented by optical measurements and their comparison with numerical calculations. This step is performed in the next chapter for the fundamental example of a straight vertical waveguide.

Chapter 7

Light Propagation in Vertical Waveguides

One of the most prominent ideas driving the interest in 3D PBG-materials is to use them as a basis for the realization of ultrasmall all-optical integrated circuits. The soundness of this concept strongly relies on the ability of defect waveguides to laterally confine and effectively guide light in order to connect the different functional components of the photonic circuit. In theory it has already been demonstrated that the efficient confinement and propagation of electromagnetic waves through straight lines, sharp bends, and multi-branches is indeed possible (see Section 3.2).
However, experimental realizations of waveguide architectures in 3D PBG-materials, which include an optical characterization, are extremely sparse, as reviewed in detail in Section 3.3. In particular, up to now only two groups have reported on the measurement of light propagation through waveguides in 3D PBG-materials [20, 21]. For fabrication, [21] relies on conventional lithography in combination with wafer fusion, [20] uses DLW in an infiltrated artificial opal, followed by a single inversion procedure. A distinct waveguide mode in the stop band has only been identified in [21], and in this case no quantitative transmittance values have been determined. Furthermore, the host woodpile structures consist of only 9 stacked layers at maximum.
In this chapter, light propagation through air-core waveguides transversing more than five lattice constants (22 layers) of PBG woodpile material is reported, and the measured spectra are compared with theoretical predictions. Furthermore, an experimental route for ex-post tuning of the waveguide mode frequency is demonstrated.

7.1 Sample Design and Fabrication

For an optical characterization of the waveguide modes several points have to be dealt with experimentally. Using the FTIR-spectrometer described in Section 4.3 for transmittance and reflectance measurements, it is crucial that the theoretically predicted defect signature in the stop band is strong enough to exceed the detection limit of the instrument. This is particularly difficult to achieve in transmittance measurements, where the background suppression

of the FTIR for small footprint samples is rather poor (see Appendix B). Furthermore, it is expected that, due to sample imperfections, light propagating in the waveguide channel will undergo losses, for the strength of which, up to now, no empirical values are known. It is therefore vital to favor a strong defect signature already by the design of the structure. In this context, the blueprint of a straight vertical acceptor-type waveguide discussed in Section 6.3 is a promising candidate, since its doubly degenerate shorter-wavelength mode is connected to a pronounced signature exceeding a transmittance level of 0.5% over a spectral range of more than $40\,\mathrm{nm}$ for the assumed 5×5-supercell and spectroscopy in forward direction. One possibility to further enhance the defect signature strength is to increase the defect density, since the signals of nominally identical waveguides in the measurement area are expected to sum up. Therefore, instead of single waveguides, 2D arrays of waveguides arranged in a regular fashion have been investigated. An additional advantage of this approach besides optimization of the defect signature strength is that no supercell *approximation* has to be made any more for the theoretical calculations, but instead the same supercell setting can be studied in the calculations as well as in the experiment.

The optimum size of the supercell is determined by several aspects. On the one hand, as the size of the supercell is decreased, the mode signature becomes more pronounced. This can intuitively be understood, as for a smaller supercell more waveguides fit within the same measurement area. If, on the other hand, the supercell is chosen too small, coupling becomes dominant and single-waveguide properties cannot be studied any more. Additionally, in the experiment, a deterioration of the bulk woodpile properties is observed if the defect density is chosen too high since the degree of connectivity and thus the stability of the structure are reduced by the presence of the defects. While for the theoretical study in Section 6.3 a 5×5-supercell was used, in this chapter a 4×4-supercell has been found to optimally balance these aspects.

A visualization of 12 ideal waveguides arranged in a 4×4-supercell array is shown in top-view in Fig. 7.1 (a) and a corresponding experimental realization is depicted in (b), where a top-view SEM image of a typical defect-containing IP-L template with nominally 900 nm lateral rod distance is displayed. For DLW of these templates the fast defect writing mode has been employed (see Section 6.4). Furthermore, the rods of the woodpile templates are built up from three individual exposures, which are laterally displaced by $\Delta x = 80\mathrm{nm}$ in order to achieve a bandgap-favorable small rod aspect ratio (see Subsection 5.1.2).

Such templates with an overall footprint of $40\,\mu\mathrm{m} \times 40\,\mu\mathrm{m}$ have been double inverted into silicon according to the procedure described in Subsection 4.2.3. Thereby, the particularities for vertical waveguide structures regarding silica ALD and HF wet-etch durations, which are discussed in Section 6.4, have been taken into account.

In Fig. 7.1 (c), a sketch of the interior of an ideal structure is shown, where the two waveguides within the displayed region are marked by white dashed lines. The depicted structural parameters are the same as for the actually fabricated silicon woodpile structure ($a = 782\,\mathrm{nm}$, $d = 0.28\,a$, $\chi_{rod} = 1.3$, $c = a$, $L = 0.73\,a$) with embedded vertical waveguides shown in (d). Here, two waveguides inside the woodpile structure have been revealed by focused ion beam milling. In both images, the viewing angle is 54 degrees from the surface normal. Obviously, the structural quality of the fabricated structure is very high, both

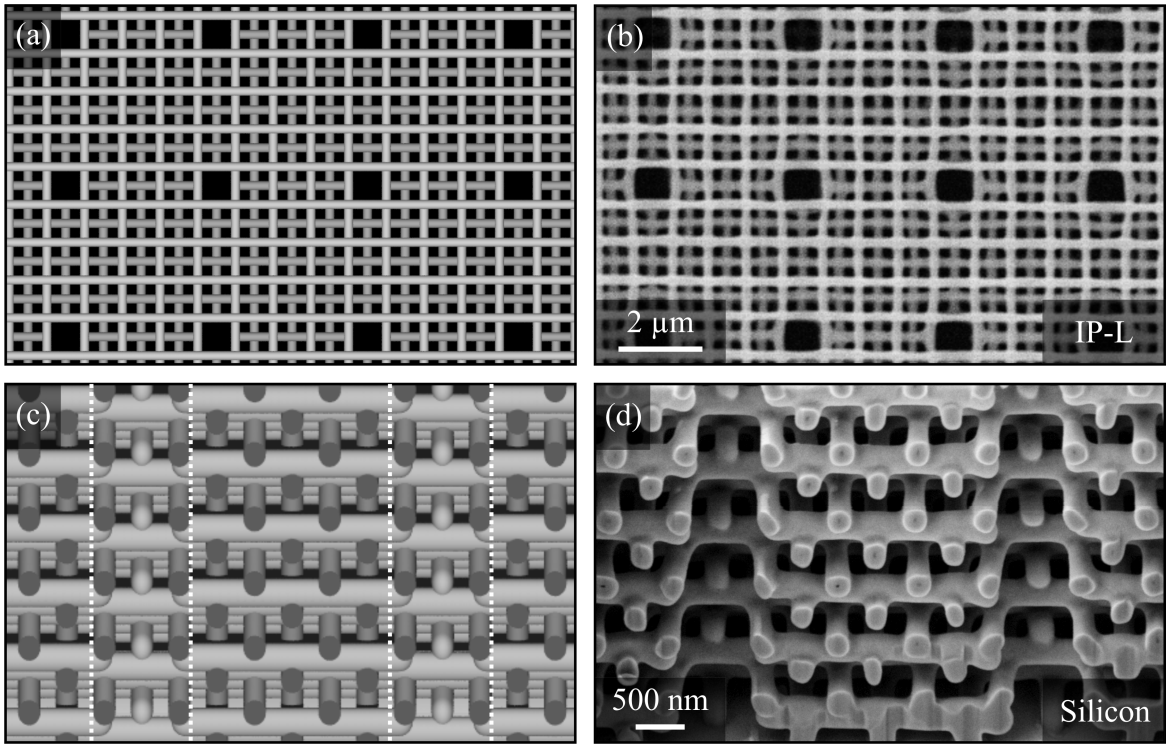

Figure 7.1: (a) Top-view sketch of a woodpile containing an array of waveguides arranged in a 4×4-supercell and (b) SEM image of a corresponding IP-L photoresist template. (c) Oblique-view visualization of an ideal structure and corresponding (d) FIB cross-section image revealing two straight vertical waveguides inside the silicon PhC. After [135].

in the defect region as well as in the bulk woodpile material. Since $c = a$ holds in good approximation for the fabricated woodpile, the underlying lattice of this structure has bcc symmetry.

7.2 Optical Characterization

Linear optical reflectance and transmittance spectra of the fabricated silicon structure have been recorded using the FTIR in combination with its standard Cassegrain optics (see Section 4.3) and an aperture with $16.7\,\mu\mathrm{m}$ sampling area diameter to achieve optimized background suppression in transmittance mode for a $40\,\mu\mathrm{m} \times 40\,\mu\mathrm{m}$ footprint sample (see Appendix B). The results are summarized in Fig. 7.2. In (a) normal-incidence intensity reflectance and transmittance spectra are shown on a logarithmic scale and for unpolarized incident light. These spectra reveal a broad stop band that is superimposed by a peak in transmittance and a dip in reflectance. In Fig. 7.2 (b), reflectance spectra for linearly polarized reflected light with the electric field oriented parallel and perpendicular to the rods of the topmost woodpile layer are displayed on a linear scale. In both polarizations a narrow peak can be identified in the stop band, the precise position of which somewhat depends

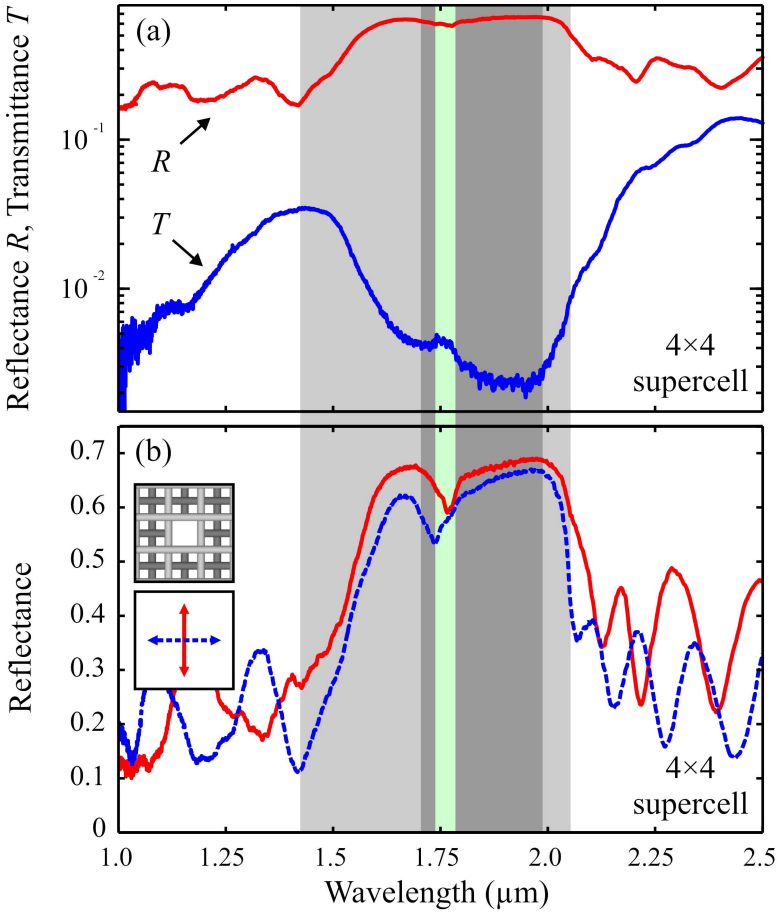

Figure 7.2: Measurements performed on a 4×4-supercell array of linear waveguides introduced in a silicon woodpile structure: Linear-optical (a) reflectance and transmittance spectra for unpolarized light on a logarithmic scale, and (b) reflectance spectra for linearly polarized reflected light on a linear scale. In (b) the insets show the orientation of the electric field with respect to the topmost woodpile layer. After [135].

on polarization. Since these sharp features result from the superposition of about 20 different waveguides within the measurement area, their mere presence already imposes an upper bound on the possible structural variations among the different waveguides.

To further analyze these experimental findings, they are compared to band-structure and scattering-matrix calculations in the following. As a first step, the band structure of the bare woodpile structure, which does not contain any waveguides, is calculated using the parameters depicted in Fig. 7.1 (a) and (c). The result is depicted in Fig. 7.3 (a). Analogous to the calculations performed in Chapter 5, the actual silicon rods with hollow core arising from the double inversion procedure (see Subsection 4.2.3) are described by massive rods with identical shape and dimensions but with an effective dielectric constant of $\varepsilon = 11$, which is slightly below the value of bulk silicon at these wavelengths. The relatively high effective-ε-value (compare Section 5.2, where $\varepsilon = 9.9$) nicely agrees with the observation that only very small

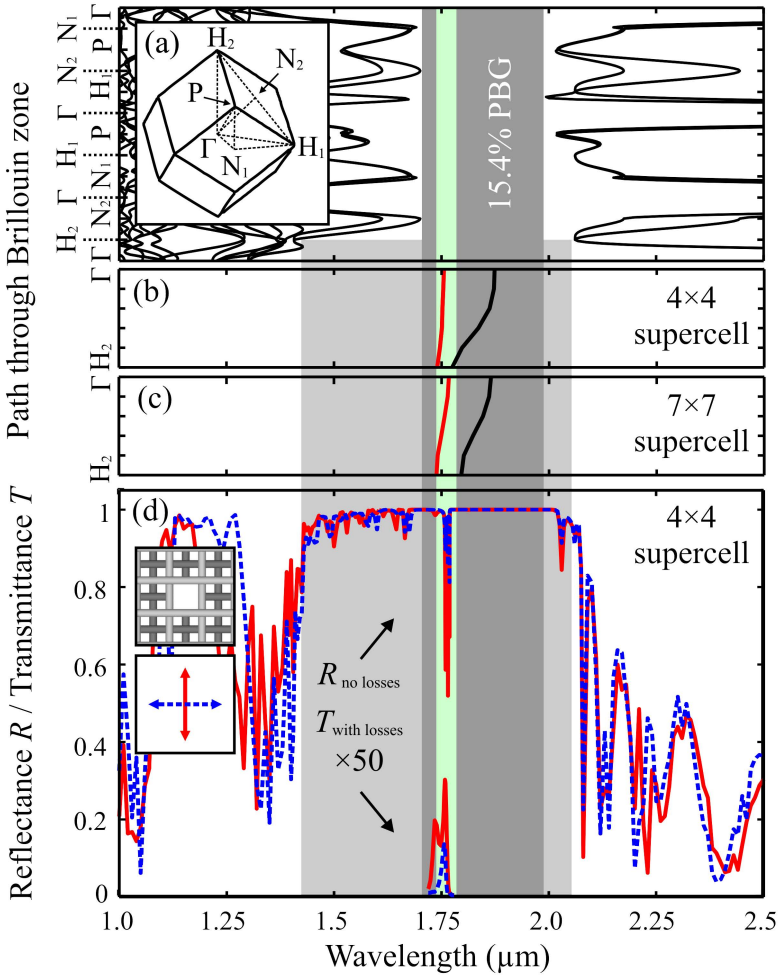

Figure 7.3: (a) Computed band structure of the undisturbed bcc woodpile structure. (b) Calculated waveguide dispersion in stacking direction for the actually fabricated 4×4-supercell and (c) for a 7×7-supercell. (d) Polarization resolved theoretical reflectance $R_{\text{no losses}}$ and transmittance $T_{\text{with losses}}$ spectra for the waveguide-containing woodpile structure using a 4×4-supercell. In (d) the orientation of the electric field with respect to the topmost woodpile layer is indicated by the insets. Scattering-matrix calculations: S. Essig. After [135].

pores are present in this structure, as obvious from Fig. 7.1 (d). The resulting band structure shown in Fig. 7.3 (a) exhibits a PBG with a gap-midgap ratio of 15.4%, which is highlighted by the dark gray area throughout Figs. 7.2 and 7.3. Analogously, the stop band in $\Gamma - \mathrm{H}_2$ direction relevant for perpendicular incidence of light is marked in light gray.

Next, the band structure of the complete structure comprising the 2D array of 1D waveguides within the 3D woodpile PhC is calculated. The waveguide dispersion in $\Gamma - \mathrm{H}_2$ direction is depicted in Fig. 7.3 (b) for the actually used 4×4-supercell. As expected from the properties of the waveguide model system investigated in Section 6.3, two dispersion branches lie within the PBG. The longer-wavelength branch depicted in black is not relevant here, because light cannot couple to this mode under normal incidence conditions due to the mismatch in

symmetry and even for the experimental conditions using the Cassegrain optics, coupling to this mode is expected to be weak. The doubly degenerate short-wavelength branch plotted in red, in contrast, can be coupled to. Its spectral position is highlighted in light green throughout Figs. 7.2 and Fig. 7.3. For comparison, the results for the 7×7-supercell are shown in (c). They are found to be very similar to those of the 4×4-supercell, indicating that interaction effects among the waveguides in the array are only of minor importance and that single-waveguide properties can effectively be studied in this setting in good approximation. In order to obtain theoretical transmittance and reflectance spectra which allow for an even more direct comparison with experiments, additional scattering-matrix calculations have been performed. Calculated normal-incidence reflectance spectra ($R_{\text{no losses}}$) of the actual structure with its finite thickness of 22 layers on a glass substrate ($n_{\text{glass}} = 1.5$) are depicted in Fig. 7.3 (d). In these calculations, exactly the same parameters as for the band-structure calculations are used. A spatial discretization of $15.6\,\text{nm}$ in propagation direction and a number of 1,185 Fourier modes laterally lead to results that are converged better than 1%.
The resulting stopband in Fig. 7.3 (d) nicely agrees with that obtained from the band-structure calculations for normal incidence ($\Gamma - \text{H}_2$-direction, light gray area in Fig. 7.3). Compared to the theoretical results the experimental stop band is smoothed out, in particular on its short wavelength side. This is at least partly due to the finite opening angle of the Cassegrain optics allowing for the coupling of the incident light to modes of the perfect crystal, which are symmetry-forbidden under strictly normal incidence (compare results in Chapter 5). Furthermore, the experimental stop band shows an incomplete recovery of the transmittance, especially in the air band, which is very likely caused by sample imperfections. Such imperfections can be observed in Fig. 7.1 (d), like the slight deformation of the entire structure caused by shrinkage, and the fact that, for the same reason, the rod endings are somewhat pulled away from the defect sites, thus slightly distorting the surrounding woodpile material (see Section 6.4). The experimental peak reflectance reaches values between 60% and 70% for both polarizations. These are typical values for woodpile structures fabricated by DLW and silicon replication or inversion [25, 134]. The losses are mainly attributed to roughness at the woodpile surface, which strongly influences the peak reflectance, but is not relevant for the interior structure quality, as discussed in Chapter 5.
The prominent dip for the complete structure found in the reflectance spectra depicted in Fig. 7.3 (d) for both linear polarizations nicely agrees with the expectation from the waveguide band shown in Fig. 7.3 (b). It also agrees with the experimental findings displayed in Fig. 7.2. The observed broadening of the experimental dips can be attributed to small variations in size and shape of the different waveguides in the measurement area. Additional symmetry breaking by sample imperfections leads to a splitting between the two otherwise degenerate waveguide modes for the two orthogonal linear polarizations (see Fig. 7.2 (b)). This behavior has recently also been found in closely related waveguide structures (see Ref. [21]) and can furthermore be expected from the theoretical analysis performed for an asymmetric model system in Chapter 6. Furthermore, this experimentally observed mode-splitting behavior provides additional evidence that the resonances found in the measured stop bands can indeed be attributed to the twofold degenerate waveguide mode.
Having in mind the aim to connect different components on a photonic chip by PBG wave-

guides, the waveguide performance is obviously a key quantity. For the waveguides presented in this chapter an estimate for the losses can be given on the basis of theory: For zero loss, the total transmittance corresponding to the reflectance shown in Fig. 7.3 (d) is simply the complement of the reflectance, i.e., roughly 35% at the waveguide resonance (not depicted), while the experimental transmittance plotted in Fig. 7.2 (a) reaches only about 0.45% at its peak position. From 2D photonic crystal waveguides it is known that propagation losses mainly originate from Rayleigh scattering due to surface roughness. These losses can be mimicked by adding a fictitious imaginary part of the air refractive index $\mathrm{Im}(n_{\mathrm{air}})$ [166]. Following this approach to model waveguide losses, additional scattering-matrix calculations have been performed, where the imaginary part of the air refractive index has been adjusted such that the total transmittance at the waveguide resonance roughly matches the experimental observation of 0.45% in Fig. 2 (a). This is found to be the case for $\mathrm{Im}(n_{\mathrm{air}}) = 0.004$. Corresponding transmittance spectra ($T_{\mathrm{with\ losses}}$) multiplied by a factor of 50 are shown at the bottom of Fig. 7.3 (d). The value of $\mathrm{Im}(n_{\mathrm{air}}) = 0.004$ represents an upper bound as the 0.45% also include diffraction of light at the output of the waveguide array that is not collected by the microscope lens, whereas the theory collects all diffracted orders. An exact experimental determination of the losses would require the comparison of waveguides of different length to separate in-coupling losses from propagation losses. The estimated value of $\mathrm{Im}(n_{\mathrm{air}}) = 0.004$ can presently not be compared to any other published 3D experiment but it may serve as a reference for future publications.
Altogether, high-quality straight vertical acceptor-type waveguides embedded in 3D silicon woodpile PBG-materials fabricated by DLW and SDI have been optically characterized and a good overall qualitative agreement to theoretical predictions has been achieved. This provides experimental proof of light propagation through 22 layers of woodpile material, where the mode is predominantly confined in air.

7.3 Tuning the Waveguide Mode

In this section, an experimental route to shifting the spectral position of the waveguide mode to a desired position is demonstrated. This kind of supplementary (fine-)tuning of the waveguide mode center frequency (or generally of defect mode frequencies) is crucial, if the waveguide mode frequency has to be shifted to an externally determined operating wavelength, or if several 3D PBG-material based devices with slightly different mode frequencies have to be adjusted to operate at the same frequency.

With this aim in mind the waveguide-containing silicon woodpile structure from the previous section is stepwise re-infiltrated by several individual cycles of silica ALD. At each cycle, approximately $25\,\mathrm{nm}$ of silica are deposited at the accessible air-material interfaces inside the 3D structure. After each cycle, reflectance spectra of the sample are taken for the two linear polarizations parallel and perpendicular to the orientation of the rods forming the topmost woodpile layer. The results of these measurements are depicted in Fig. 7.4 (a) and (b). Here, the spectra for subsequent cycles are offset by $R = 0.2$. For both polarizations it is

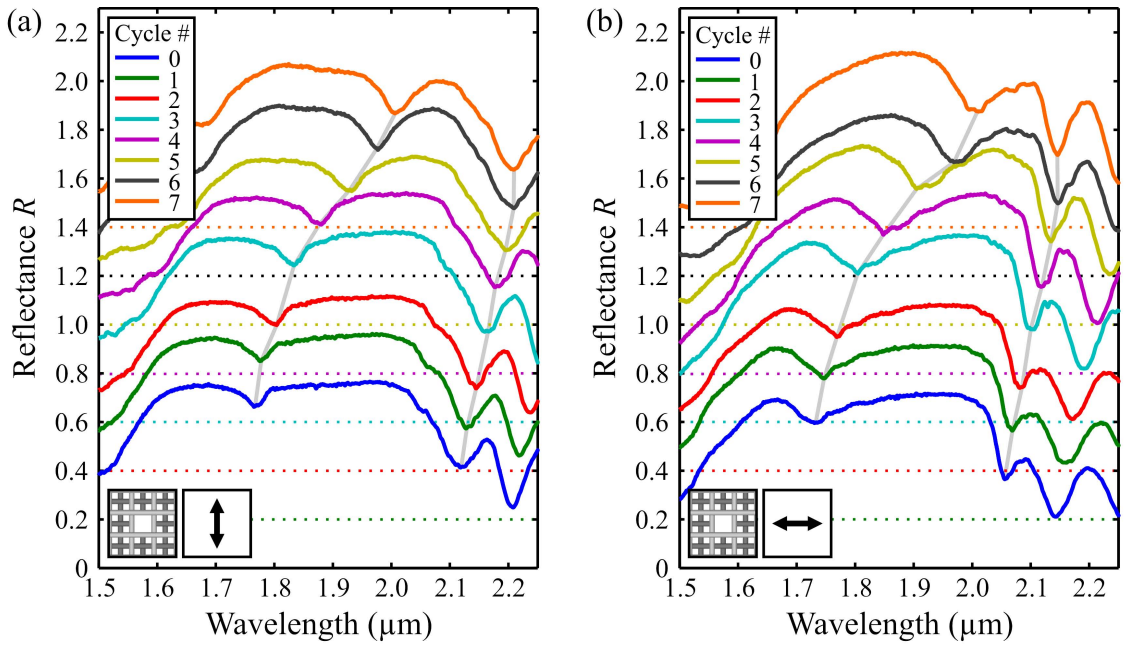

Figure 7.4: Linear-optical transmittance spectra for linearly polarized reflected light for the waveguide-containing silicon woodpile structure measured after subsequent individual cycles of silica ALD. The light gray lines are guides to the eye, highlighting the respective positions of the waveguide mode signature and the dielectric stop band edge. The insets indicate the respective directions in which the electric field is oriented with respect to the topmost woodpile layer in (a) and (b).

clearly visible how the waveguide mode is red-shifted after each cycle owing to the increase of silica layer thickness in the defect channel. The entire stop band is also red-shifted, but in smaller steps. From cycle 6 to cycle 7, no further shift of the stop band can be observed any more, that is, the host woodpile structure is already completely infiltrated before the start of cycle 7. At this point the silica layer has reached a thickness of half the infiltration bottleneck of the woodpile structure, and thus the precursor gases cannot penetrate the 3D structure any more such that material deposition inside is stopped. The bottleneck appears between neighboring rods in next but one layers, as indicated by the green arrow in Fig. 7.5 (a), where a FIB cross-section image of the structure after 12 cycles of silica ALD is depicted. Using the same structure parameters as in the previous section ($a = 782\,\mathrm{nm}$, $d = 0.28\,a$, $\chi_{rod} = 1.3$, $c = a$, $L = 0.73\,a$), the bottleneck width is calculated to be $303\,\mathrm{nm}$, resulting in a maximum silica layer thickness of $151.5\,\mathrm{nm}$ that can be deposited in the woodpile structure before the bottlenecks are closed.

The waveguide channel, on the other hand, is not yet completely infiltrated after deposition of $151.5\,\mathrm{nm}$ of silica and the precursor gases responsible for silica growth can still penetrate this region from the top of the sample. This can also be observed from Fig. 7.5 (a), where the silica layer thickness deposited in the defect region is obviously larger than in the surrounding woodpile material. Consequently, while the stop band position remains unchanged after cycle 6, the waveguide mode is further red-shifted by the 7th ALD cycle, thereby once again

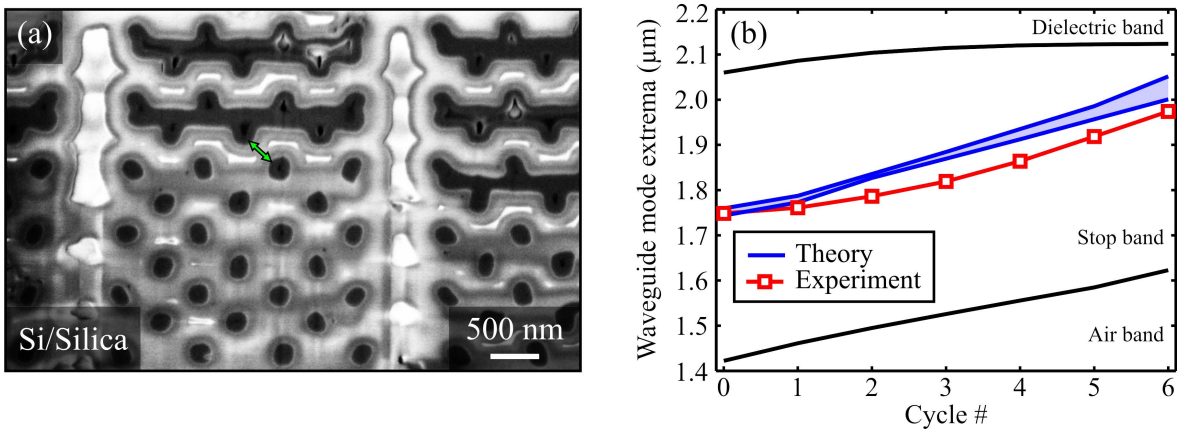

Figure 7.5: (a) FIB cross-section image of the defect-containing silicon woodpile structure, which has been completely re-infiltrated by 12 cycles of silica ALD. Silicon appears in dark gray, silica in light gray. White regions are either air regions or stem from electric charging effects. The green arrow marks the position of the infiltration bottleneck in this woodpile structure. (b) Calculated band extrema of the degenerate waveguide mode (blue) and measured waveguide signature positions found in the experiment (red) after each silica ALD cycle. After cycle 6 the host woodpile structure is completely infiltrated.

indicating that the resonances found in the spectra are indeed the signatures of the waveguide modes.

In order to compare these experimental findings with theory, additional band-structure calculations that include the silica layer have been performed for cycles 1 to 6, that is, for each ALD cycle contributing to the complete infiltration of the host woodpile structure. In these calculations, the silica layer thickness deposited at each ALD cycle is set to one sixth of the theoretical half-width of the bottleneck, namely $25\,\mathrm{nm}$, and the refractive index of the silica is taken as 1.45. Corresponding results are depicted in Fig. 7.5 (b), where the band extrema (blue) of the waveguide mode are plotted against the performed number of ALD deposition cycles. The midband position is shifted from $1.75\,\mu\mathrm{m}$ for the uninfiltrated case to $2.03\,\mu\mathrm{m}$ for the completely infiltrated structure, which is in good agreement with experimental observations (red line) also included in Fig. 7.5 (b). The plotted experimental data correspond to the dip minima positions averaged over the two measured linear polarizations. In the experiment the shift is slightly smaller than in theory, which can be attributed to deviations from perfect periodicity narrowing down the effective width of the bottlenecks. This results in an overestimate of the actually deposited silica layer thickness and thus in an overestimated shift. As visible from Fig. 7.5 (b), not only the midband position but also the expected bandwidth of the waveguide mode (highlighted in light blue) is changed by silica re-infiltration. Starting from cycle 2, it is increased towards larger cycle numbers. Qualitatively, this behavior can also be found in the experiment, where the dips become broader and more pronounced as the number of performed ALD cycles increases (see Fig. 7.4).
Using this technique to shift the waveguide mode position, one has to keep in mind, however,

that the size of the PBG is decreased by the reduction of the refractive index contrast connected to silica infiltration. After one cycle, the above calculations still predict a PBG with a gap-midgap ratio of 14.4%; for the completely infiltrated structure, however, this value is reduced to 0.7%.
Altogether it has been shown that the waveguide mode can be tuned by cycle-wise re-infiltration of the 3D structure with silica and experimental tuning over a wavelength range of approximately $250\,\mathrm{nm}$ has been demonstrated, which is compatible with corresponding band-structure calculations.
The degree of control could further be improved by use of an ALD process, where exactly one atomic layer per cycle is deposited. In this way, a very precise fine-tuning of the waveguide mode position would become possible. Furthermore, for such a fine-tuning only very thin layers of silica have to be infiltrated into the woodpile structure and consequently the size of the PBG is only marginally decreased.

To summarize, it has been experimentally verified that, using DLW and SDI, it is not only possible to include designed line defect structures into PBG-materials in a precise and controlled manner, but also that the optical quality of the fabricated structures is indeed sufficiently high to provide the desired optical functionality of guiding light from one location in the 3D PhC to another. In combination with the high flexibility of the employed fabrication approach demonstrated in Section 6.4 this result raises hopes that the realization of ultrasmall all-optical integrated circuitry based on 3D PBG-materials may finally come into reach in the not too distant future.
While all-optical integrated circuits are a classic among the envisioned applications for 3D PBG-materials, the next chapter is devoted to a completely different potential device based on defect structures in silicon woodpile structures, namely a PBG particle accelerator.

Chapter 8

A Silicon Woodpile Particle Accelerator

At first glance, one of the most prominent characteristics of a modern high-energy particle accelerator is its size. The International Linear Collider (ILC), for example, which is currently at the planning stage, is designed to have a length of 31 km and will cost billions of Euros to build. But even relatively modest accelerators used to drive synchrotrons take up the area of several thousand square meters. In conventional high-energy accelerators the actual particle acceleration is typically performed by copper or superconducting high-frequency (up to GHz) metal cavities. Their accelerating gradient, which directly translates to the length an accelerator needs to accelerate a particle to a desired energy, is limited by the maximum fields that can be sustained without electrical breakdown. The acceleration technology of the ILC is based on 16,000 superconducting cavities made of pure niobium, which support an accelerating gradient of $31.5\,\mathrm{MV/m}$ [167]. An illustration of charged particle acceleration

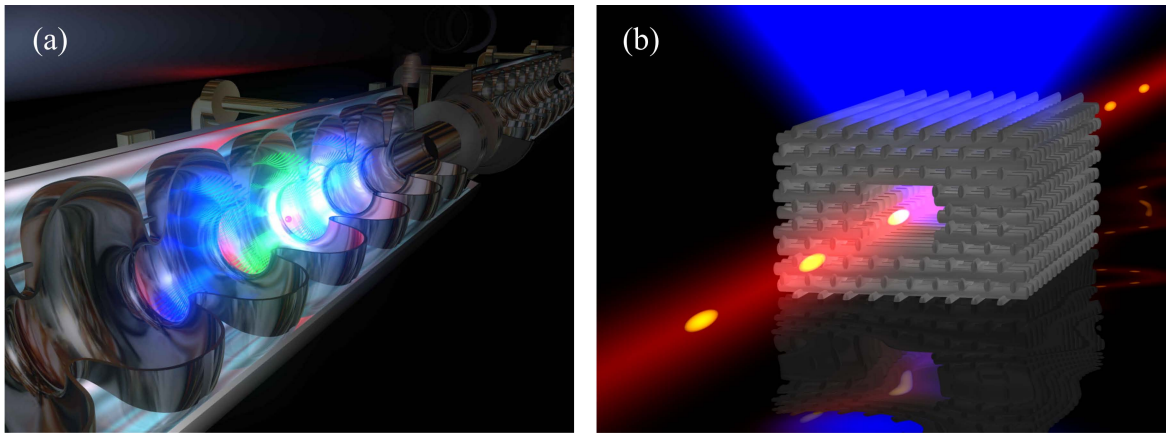

Figure 8.1: (a) Illustration of particle acceleration in a conventional high-frequency accelerating cavity. Taken from [168]. (b) An artist's view of laser driven particle acceleration using a woodpile structure with a designed defect waveguide.

by such a superconducting niobium cavity resonator is depicted in Fig. 8.1 (a).
Driven both by the wish to accelerate particles to higher and higher energies on the one hand, and, on the other hand, to allow for the construction of smaller and cheaper systems

for moderate demands, such as medical applications, the quest for alternative acceleration mechanisms using unconventional acceleration mechanisms has become an active field of research. Owing to the extraordinary electric fields and efficiencies available from laser systems, approaches based on laser-driven charged particle acceleration are promising candidates in this context. Acceleration of charged particles requires electric field components in particle beam direction, so a transverse-electric mode provided by a laser beam in free space cannot directly be used for this purpose. However, several possibilities to overcome this limitation have been proposed. Among them, one of the most promising is that of wake-field acceleration, where electrons are carried forward by plasma wakes, which are generated by sending a Terawatt laser through a gas [169]. Other approaches in the field of laser-driven particle acceleration focus on photonic submicron structures, which have the great advantage that only micro-Joule class lasers are needed, that is, compact devices like fiber lasers, instead of large-scale multi-staged amplifier systems. Furthermore, high accelerating gradients and efficiencies are possible based on such approaches and fabrication is envisioned to be realized by inexpensive mass-scale manufacturing. In this category, hollow core PhC fibers [170], double grating structures [171], and PhC accelerator structures [19, 172] are to be mentioned. The approach taken up in this thesis is that proposed by B. M. Cowan in 2008 [19], which is based on a line defect waveguide geometry inside a silicon woodpile 3D PBG-material. In [19] it is demonstrated theoretically that such a structure can in principle be used for efficient charged particle acceleration. An artist's view of the underlying concept is provided in Fig. 8.1 (b). Short electron bunches and a picosecond laser are synchronously coupled into a line defect waveguide, where the electrons are then accelerated by the waveguide mode excited by the laser. In the following, the structure geometry as well as the acceleration mechanism and performance of this concept are discussed in more detail. Subsequently, it is demonstrated that a combination of DLW and SDI can provide a feasible experimental route to fabricate corresponding 3D submicron structures.

8.1 Functional Principle

8.1.1 Structure Geometry

The host structure assumed in [19] for the accelerating device is a fcc ($c = \sqrt{2}a$) silicon woodpile structure made of stacked rectangular rods with $d = 0.28\,a$. For a silicon dielectric constant of $\varepsilon = 12.1$, the woodpile exhibits a 3D PBG with a gap-midgap ratio of 18.7%. Inside this structure a waveguide is formed by removing all dielectric material in a region which is rectangular in the transverse x and y directions, and extends over the entire length of the woodpile structure in the e-beam propagation direction z. Furthermore, two additional modifications of the structure geometry are performed. First, the structure is made vertically symmetric by inverting the upper half of the lattice, which serves to avoid deflecting fields in the accelerating mode. Second, the central bars are extended into the waveguide by $0.124\,a$ on both sides in order to suppress quadrupole fields, which would otherwise exert focusing or defocusing forces on the charged particles. The woodpile geometry including the

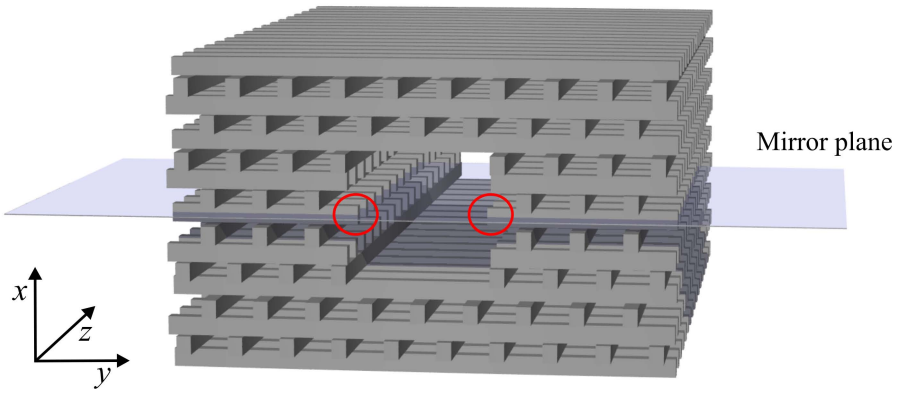

Figure 8.2: Illustration of the 3D photonic crystal particle accelerator structure proposed in [19].

waveguide is visualized in Fig. 8.2. The modifications performed to suppress the undesired deflecting and focusing fields are highlighted by the mirror plane (light blue) and the two red circles, respectively. As evidenced by finite-difference time-domain simulations in [19], this waveguide supports a confined accelerating mode with the electric field pointing along z-direction within the waveguide channel. For this mode, $a/\lambda = 0.364$ and $v_g = 0.269\,c_0$. Since the mode has to be excited using an external laser source, it is desirable to construct the accelerating device for operation wavelengths in the telecom wavelength regime, where efficient and cheap laser sources are on hand. Assuming an operation wavelength of $1.55\,\mu\mathrm{m}$ results in structural dimensions of $a = 565\,\mathrm{nm}$, $d = 158\,\mathrm{nm}$, and $h = 200\,\mathrm{nm}$. Nevertheless, owing to scalability, these values can as well be relaxed as long as appropriate laser sources are available. Ultimately, the operation wavelength will be chosen by maximizing the optical damage threshold of the silicon (see Subsection 8.1.3).

8.1.2 Acceleration Mechanism

The waveguide-containing woodpile structure described in the previous subsection is envisioned to operate as a traveling-wave accelerator, where the particles and the electromagnetic fields move synchronously along the waveguide and the particles stay at the peak of the accelerating phase all the time (in contrast to a standing-wave accelerator). A necessary requirement for traveling-wave acceleration is synchronization, that is, the phase velocity of the accelerating mode has to be equal to c_0 in order to further accelerate a relativistic particle traveling nearly at the speed of light[1], otherwise the particle would slip out of phase and the net energy gain would be zero, as stated by the Lawson-Woodward theorem [174]. In order to verify that an accelerating waveguide mode allows for synchronization, its dispersion diagram and the light line have to be intersecting each other for a proper combination of the

[1]The speed v of a relativistic particle as a function of its energy E is given by $\frac{v}{c_0} = \sqrt{1 - \left(\frac{m_0 c_0^2}{E}\right)^2}$, that is, v asymptotically approaches c_0 for high energies. For example, for electrons with $m_0 c_0^2 = 511\,\mathrm{keV}$ and $E = 10\,\mathrm{MeV}$, one already obtains $\frac{v}{c_0} \approx 0.9987$.

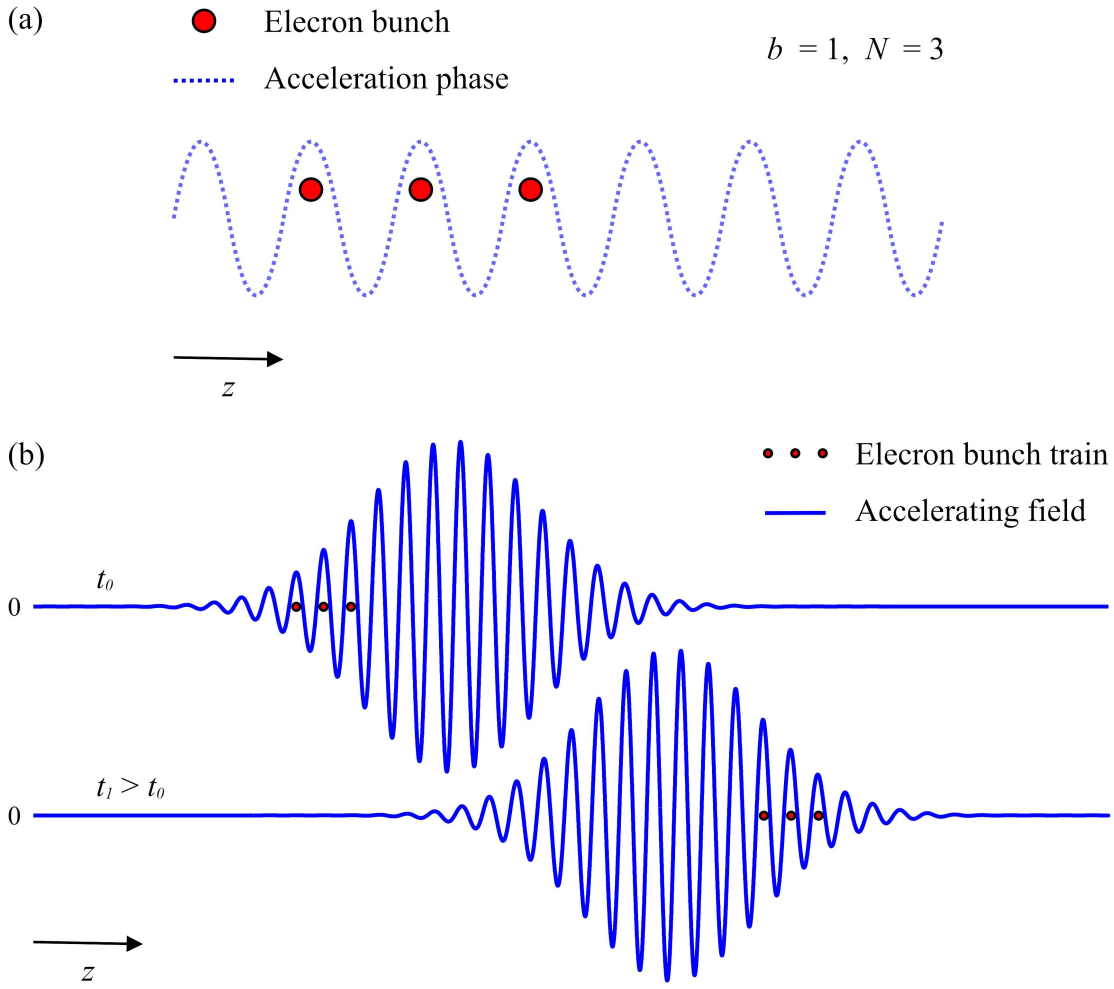

Figure 8.3: (a) Schematic of a train of particle bunches situated at the peak of the acceleration phase. Adapted from [173]. (b) Snap shots of the accelerating field and the particle bunch train at two different time steps (not to scale), if ultrashort laser pulses are used to excite the accelerating mode with $v_g < c_0$.

mode's frequency ω and wave vector k. If this condition is fulfilled, the charged particles, which are identified with electrons in the following, must further be optically microbunched [175] to lengths much smaller than λ in order to sample only a small range of optical phases of the accelerating mode. If the bunches are not short enough, electrons at different z-positions of a single bunch will experience significantly different accelerating forces and a large energy spread will develop in the beam. Given an proper bunch length, single bunch and multiple bunch operation can be considered. In the latter case the particles are assumed to come in trains of N bunches spaced by $b\lambda$, where b is an integer [173]. This results in a total length of the particle bunch train of $Nb\lambda$. The situation for multiple bunches operation, where the bunches are set to be on the peak of acceleration phase, is schematically illustrated in Fig. 8.3 (a) for $b = 1$ and $N = 3$.

The strength of the electric fields in the accelerating mode determines how strong the particles can be accelerated. Remarkably, the accelerating gradient of the above described waveguide structure is not limited by the power provided by the available laser sources, but by optical breakdown of the structure material. In order to optimize the performance of the structure, one would therefore adjust the laser power as close to the threshold as possible without causing damage to the structure material, and furthermore choose the properties of the exciting laser light such that the threshold itself occurs for high input laser powers. To this end it is favorable to use ultrafast laser pulses of duration σ_τ on the order of $1\,\mathrm{ps}$, for which the breakdown threshold of silicon is comparably high [176]. This demand to use short laser pulses has consequences for the accelerator design. Given that the group velocity v_g of the waveguide mode is less than c_0 ($v_g = 0.269\,c_0$ in the case of the woodpile waveguide structure), a relativistic particle beam will outrun a laser pulse propagating along the waveguide after a certain distance [19], or, in other words, the laser pulse envelope will slip with respect to the particle bunch train. The dynamics of the laser pulse and the particle bunch train with respect to each other are schematically depicted in Fig. 8.3 (b). For reason of this slippage, the accelerator has to be constructed in short segments and laser pulses have to be coupled in periodically. In order to estimate the maximum possible length L of a segment, the quasisingle bunch approximation

$$\Delta\tau \gg \frac{Nb\lambda}{c_0} \tag{8.1}$$

is made. Here, $\Delta\tau$ denotes the time the laser pulse envelope slips relative to the particle beam as it passes through the accelerator. This time is given by

$$\Delta\tau = \frac{L}{c_0}\frac{1 - v_g}{v_g}. \tag{8.2}$$

Assuming $\Delta\tau = 3\sigma_\tau$ as an acceptable value for the slipping time results in a maximum structure length of $L = 331\,\mu\mathrm{m}$ [19].

8.1.3 Accelerator Performance

As already mentioned in the previous subsection, the maximum sustainable accelerating gradient on axis E_{acc} is limited by optical breakdown of the structure material. An estimate of E_{acc} can be performed by relating the accelerating gradient to the breakdown threshold of the dielectric. To this purpose, the damage impedance Z_{d}, which is a property of the accelerating mode itself, is defined by

$$Z_{\mathrm{d}} = \frac{E_{\mathrm{acc}}^2}{2u_{\mathrm{max}}c_0}, \tag{8.3}$$

where u_{max} is the maximum electromagnetic energy density anywhere in the material. Assuming that breakdown occurs when the electromagnetic energy density exceeds a certain threshold u_{th} in the material, E_{acc} can be written as

$$E_{\mathrm{acc}} = \sqrt{2Z_{\mathrm{d}}u_{\mathrm{th}}c_0}. \tag{8.4}$$

Using this expression and literature values for the silicon optical breakdown threshold at $1.55\,\mu\mathrm{m}$ wavelength and $1\,\mathrm{ps}$ FWHM pulse width [176], an unloaded accelerating gradient of $301\,\mathrm{MV/m}$ is obtained for the accelerating mode in the silicon woodpile structure [19]. This value is reduced to 218 MV/m due to the advancement of the electrons with respect to the Gaussian laser pulse envelope. Furthermore, a bunch will generate wakefields in the waveguide which destructively interfere with the incident laser pulse. This further decreases the average gradient to $197\,\mathrm{MV/m}$ [19]. Still, for an electron passing through an accelerating segment with a length of only $100\,\mu\mathrm{m}$, this value corresponds to an energy gain of $19.7\,\mathrm{keV}$.

Another crucial performance measure for laser driven accelerator structures is optical-to-beam efficiency, that is, the sum of all the kinetic energy gains divided by the input laser energy. A procedure to calculate this quantity is given in Refs. [173, 177]. It depends on several parameters:

- The characteristic impedance of the mode, which describes the relationship between input laser power and accelerating gradient.
- Energy losses introduced by wakefield effects.
- Energy losses due to wideband Čerenkov radiation.

Furthermore, the efficiency can be increased significantly by incorporating the accelerator into an optical cavity, which serves to recover the energy that would otherwise be lost due to wakefield generation [177]. Given this setting, optical-to-beam efficiency has been evaluated for the accelerating mode of the waveguide-containing woodpile structure. For single bunch operation it reaches 38%, while for a train of 100 bunches, an efficiency of 76% can be achieved [19].

8.1.4 "Accelerator on a Chip"

Besides a large accelerating gradient and high efficiency, the above described waveguide structure has the advantage, that not only accelerating modes, but also focusing modes are supported by the structure for a slightly modified geometry. More specifically, by extending the central bars by $0.188\,a$ into the waveguide region, the focusing gradient for fields at damage threshold is equivalent to an $831\,\mathrm{kT/m}$ magnet. Making use of these focusing forces, particle bunches can be propagated stably in a system of focusing and accelerating elements designed to confine the particle beam, as shown by full simulations of particle trajectories performed in [19]. This is a remarkable result given the extremely small aperture of the waveguide, which is approximately λ in each transverse direction.
Another crucial element needed for a functional accelerator — and provided by the woodpile structure — are efficient couplers, that laterally couple the laser beam to the accelerator in order to avoid aligning the beam source and the laser source on the same axis. Designs and simulations for such couplers are proposed in [178] for the woodpile accelerator structure.
Ultimately, accelerating and focusing elements as well as beam couplers could directly be

integrated into the woodpile structure during the same lithography process. This comes already close to the idea of creating an "accelerator on a chip", as envisioned by C. D. Barnes *et al.* , setting the goal "...to lithographically produce the power source, power transmission system, accelerator structures, and beam diagnostics on a single substrate by semiconductor process" [179].
Naturally, this ambitious vision poses serious challenges for the employed fabrication method. Even for the experimental realization of one single accelerating segment, the method has to be able to introduce designed defects into relatively large-scale (structure lengths on the order of $100\,\mu\mathrm{m}$) high-quality silicon woodpile structures with a substantial number of layers, namely 17 in [19]. Although a four-layer test woodpile structure has been fabricated in [180] based on a combination of conventional lithography and a stacking technique [28, 181], an experimental realization of the full woodpile geometry comprising the defect waveguide has not been accomplished yet by any method. In the following section corresponding results are presented for the first time. For fabrication, a combination of DLW and SDI is used, demonstrating that this approach is in principle capable to meet the above mentioned demands.

8.2 Experimental Realization: First Steps

8.2.1 Sample Fabrication

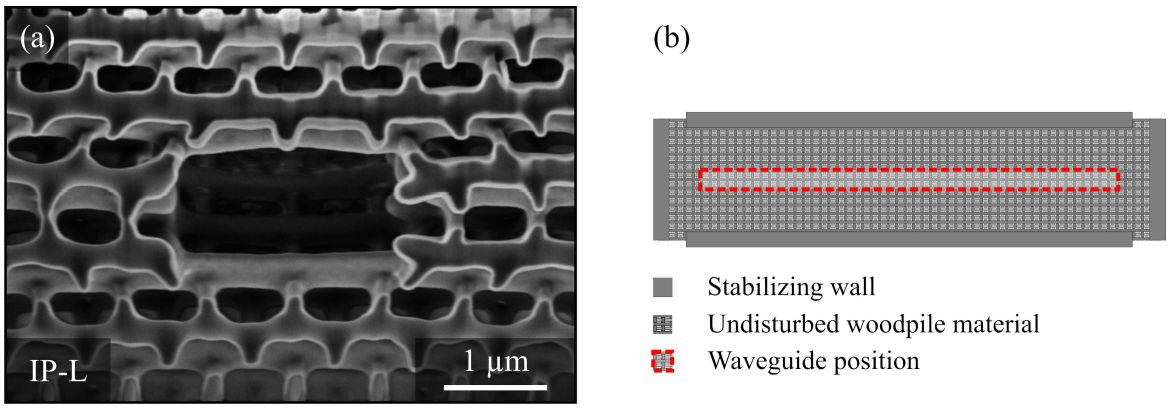

Figure 8.4: (a) FIB cross-section image of an IP-L woodpile template containing the waveguide defect. (b) Layout of an IP-L template of the waveguide-containing woodpile structure designed for silicon inversion (schematic).

In order to arrive at an experimental pilot sample of the full woodpile accelerator geometry, the compatibility of the structure design with DLW and SDI is checked successively for the two fabrication steps. First, experiments focusing on the DLW process are performed. In several iterations of DLW and SEM inspection a suitable DLW input file is developed, which controls the precise introduction of the waveguide into the host woodpile structure. The defect rods in y-direction are interrupted using the fast defect writing approach (see Section 6.4), those in z-direction are simply not written. The nominal lateral rod distance

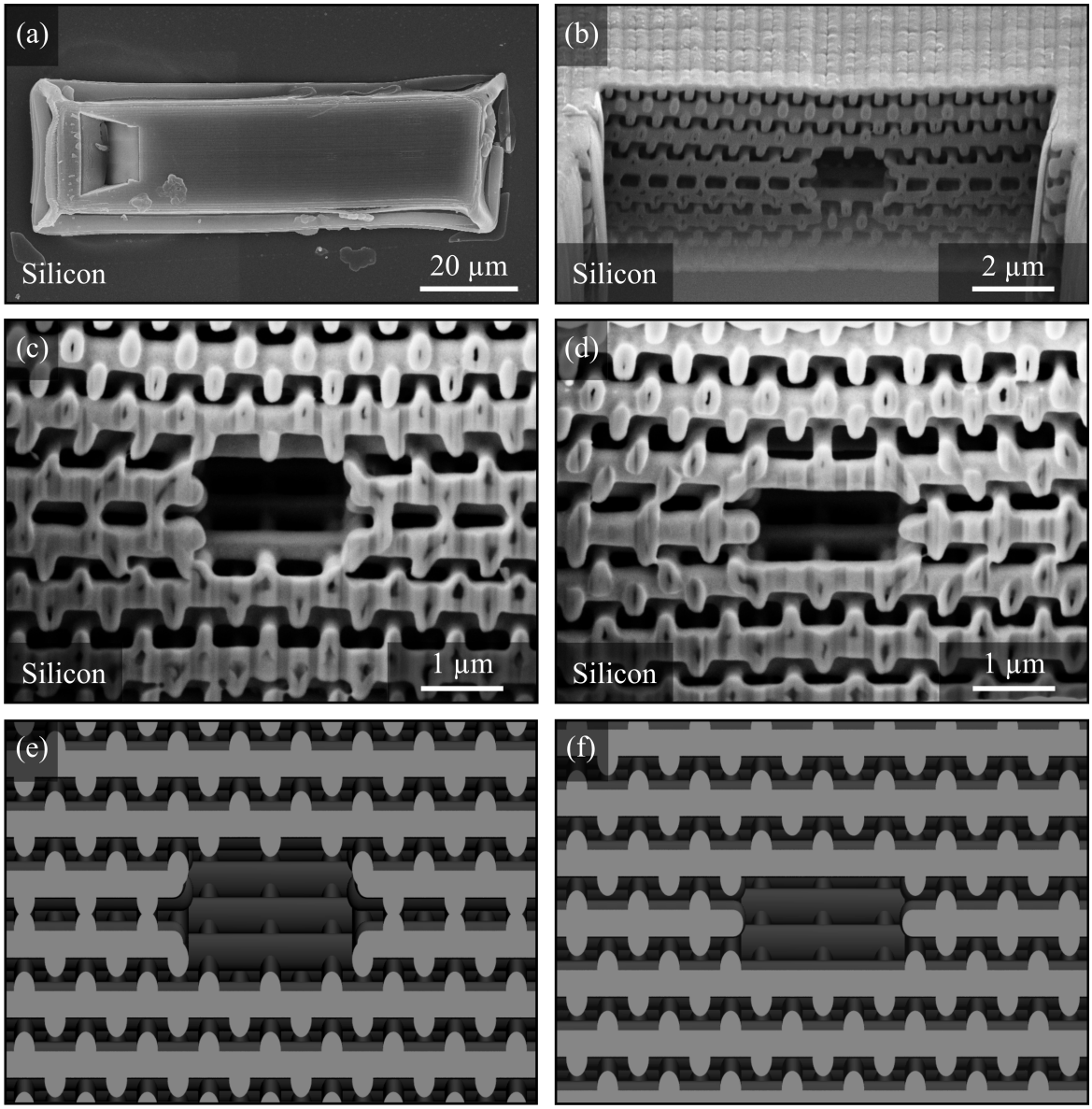

Figure 8.5: SEM images of a pilot sample for the accelerating segment. FIB milling has been performed in order to reveal the waveguide buried inside the silicon woodpile structure. (a) shows a top-view SEM image, (b) a FIB cross-section overview image. Close-ups at two different z-positions of the FIB cut, which differ by half a lateral rod distance, are displayed in (c) and (d). For comparison with an ideal structure, corresponding 3D renderings are depicted in (e) and (f).

of the woodpile structure is $800\,\mathrm{nm}$ and each rod is built up by three individual exposures, which are laterally displaced by $65\,\mathrm{nm}$ with respect to each other. A FIB cross-section image of a resulting IP-L template is shown in Fig. 8.4 (a), where the waveguide inside the woodpile structure spanning 7 layers in x-direction and three rod distances in y-direction is clearly visible.

Based on these positive DLW results, in the second step it is tested if this particular defect

geometry can be replicated into silicon by SDI. To this end templates similar to that depicted in in Fig. 8.4 (a) have been prepared using DLW. As schematically illustrated in Fig. 8.4 (b), these templates are surrounded by walls to stabilize the structures and reduce shrinkage effects. Comprising the walls, they are approx. $30\,\mu\mathrm{m}$ wide and $100\,\mu\mathrm{m}$ long, that is, their footprints are already on the order of magnitude of the ultimately demanded dimensions ($331\,\mu\mathrm{m}$ length). The waveguide is oriented along the long axis of the sample. In order to prevent the silicon from penetrating into the defect region, several lattice constants of undisturbed woodpile material are included at both ends of the woodpile structure, such that the waveguide is completely surrounded by woodpile material from all sides (see Fig. 8.4 (b)). The prepared polymer templates have been inverted into silicon using the SDI procedure described in Subsection 4.2.3, whereupon no additional efforts are necessary compared to SDI of a bare woodpile structure. Electron micrographs of the resulting structures and corresponding sketches of an ideal structure for comparison are depicted in Fig. 8.5 (a)-(d) and (e)-(f), respectively. After the SDI procedure, which results in the destruction of the stabilizing walls, the length of the silicon woodpile structure is approx. $80\,\mu\mathrm{m}$. The experimentally realized waveguide geometries shown in these images come already close to the ideal structure, which demonstrates that the defect geometry of the accelerating waveguide defect is indeed accessible using DLW and SDI. Integration of accelerating segments with focusing segments and couplers is straightforward owing to the high flexibility of the fabrication approach (compare Section 6.4).

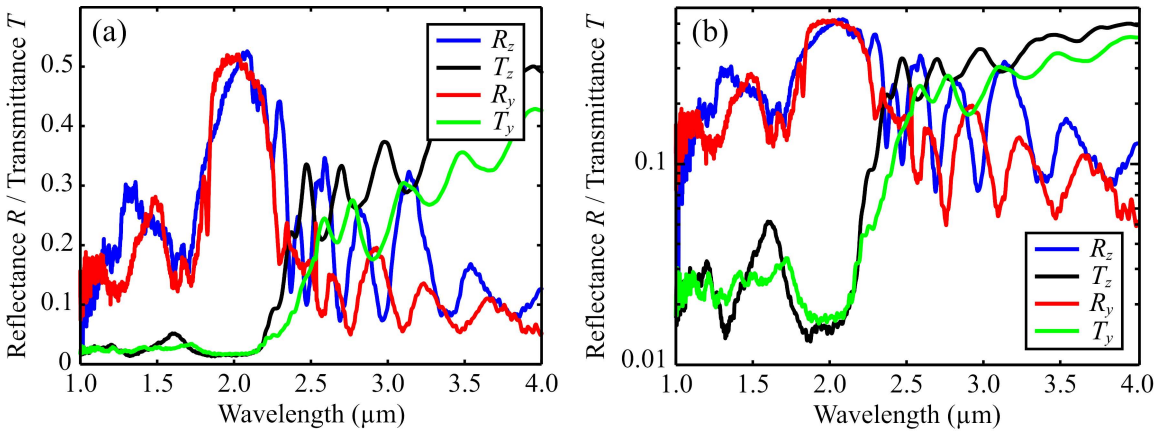

Figure 8.6: Polarization-resolved linear-optical transmittance and reflectance measurements for a pilot sample of the accelerating segment, (a) on a linear and (b) on a logarithmic scale.

In order to assess the optical quality of the obtained structures, the aforementioned fabrication steps have been reproduced and linear-optical reflectance and transmittance spectra of the resulting structure have been recorded using a commercial FTIR spectrometer (see Section 4.3). Measurements have been performed for linearly polarized incident light with the electric field oriented parallel (z-polarization) and perpendicular (y-polarization) to the propagation direction of the waveguide. The results are depicted in Fig. 8.6 (a) on a linear scale and in (b) on a logarithmic scale. In both figures the stop band around 2 μm is clearly

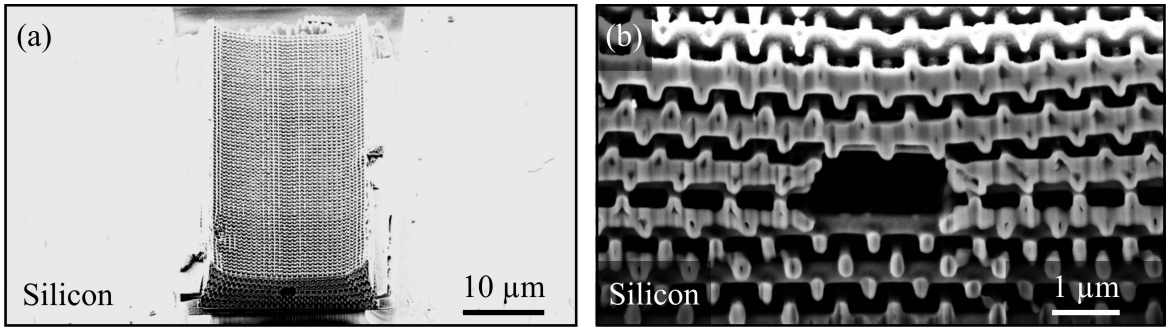

Figure 8.7: SEM images of the sample corresponding to the measured spectra plotted in Fig. 8.6. In (a) an overview of the entire structure is given, (b) shows a close-up of the front face.

visible, indicating that a fairly high optical quality has been achieved despite the presence of the large defect waveguide. Furthermore, significant differences in the shape of the spectra for the two linear polarizations can be observed, which may be attributed to coupling to the defect waveguide. Especially in reflectance, where the measurement is not hampered by the limited background suppression caused by the small lateral width of the structures (see Appendix B), differences can clearly be observed. In Fig. 8.7 (a) and (b), SEM images of the corresponding silicon woodpile waveguide structure are shown. Both ends of this structure have been removed by FIB milling. In this way, the originally completely embedded waveguide is opened up such that a particle beam could be coupled in. Numerical calculations of reflectance and transmittance spectra for the above structure are extremely challenging because of the large size of the defect waveguide, which in turn demands for a large computational cell. Such calculations are a topic of current research (C. McGuinness, SLAC National Accelerator Laboratory) and will ultimately allow for comparison with measured data.

8.2.2 Towards Functional Devices

While an experimental realization of the central geometrical features of a photonic accelerator has been demonstrated in the previous subsection, a number of issues remains to be addressed in order to fabricate functional accelerator structures.

Structure Breakdown Studies One critical issue pointed out in Ref. [19] is that a greater understanding of the structure breakdown threshold is needed. While corresponding literature values used to estimate the accelerating gradient of the woodpile structure (see Subsection 8.1.3) have been measured for bulk silicon [182], this value is in fact expected to depend on the geometric structure. Therefore, systematic material breakdown studies on fabricated prototypes will have to be performed, for which a large number of prototype structures has to be provided. The need for such experiments brings out another advantage of the approach pursued in this thesis compared to stacking techniques, namely its speed: using DLW and SDI the number of structures that can be produced within several days is on the order of 100.

Structure Quality Another issue of major importance is the quality of the fabricated structures. In [182] preliminary studies on the fabrication tolerance of the accelerator structures have been performed based on the criterion that the accumulated phase error has to be less than π over the length of an accelerating segment, which is taken as $100\,\mu\mathrm{m}$. This study indicates that an root mean square layer-to-layer horizontal misalignment of only $0.05\,a$ is tolerable, which is not yet achieved for the above structures. It is therefore crucial to further improve the quality of the manufactured samples. This quality is essentially limited by shrinkage effects, which occur mainly during development of the photoresist templates and again, to a weaker extent, during resist calcination, which has to be performed as a compulsory step of the SDI procedure. The structures depicted in the previous subsection clearly show the influence of these effects, in particular in the woodpile material surrounding the waveguide, where the open rod endings are pulled away from the defect region. Compared to the straight vertical waveguide discussed in Chapter 7, these effects are stronger for the accelerating waveguide defect because of its larger volume. The DLW control file used for writing of the structures already includes shrinkage pre-compensation by adiabatically displacing the z-rods next to the waveguide for a fraction of the lateral rod distance in direction of the defect. Using this technique, the rods end up closer to their designated positions. However, since the amount of shrinkage depends on the filling fraction and on the obtained degree of cross-linking of the photoresist, an exact shrinkage pre-compensation is extremely challenging. Furthermore, while a correct positioning of the rods may in principle be achieved, shrinkage-induced deformations of the rods can generally not be avoided by this technique. Therefore additional approaches have to be explored in order to further improve the sample quality.

The shrinkage contribution caused by resist calcination can probably be avoided by substituting the silica as intermediate material during the SDI procedure (see Subsection 4.2.3) by a thermally more stable material, like, e.g., zinc oxide (ZnO), that can be deposited by a suitable ALD process.

The contribution due to polymer shrinkage is more difficult to address. Nevertheless, several approaches for improvement are worth considering. One possibility is to change the way the waveguide is introduced into the woodpile structure. Instead of interrupting the y-defect-rods and leaving out the z-defect-rods, the entire waveguide can be defined as bulk material. In this way shrinkage effects in the waveguide region are drastically reduced since there are no loose ends any more. After silicon replication or inversion, the bulk defect transforms into a hole owing to bottleneck formation. However, for SDI, a silicon skin necessarily forms at the edges of the defect region and an accelerating mode is not supported any more by the resulting geometry, since the modes tend to concentrate their electric-field intensity inside the skin in this case, as verified by numerical simulations performed by C. McGuinness [183]. Therefore, an additional step is needed to remove the skin. Possibly, this could be done by wet-etching the silica-silicon composite structure with KOH after opening up the defect channel with a FIB. In this situation, the bulk woodpile material would be protected by the silica while the bare lying silicon skin at the defect edges could be attacked by the etchant.

A completely different route, which also starts from a template with a bulk defect but avoids the additional etching step, is to perform a SSI procedure of the template instead of an SDI

procedure. By doing this, the waveguide can directly be fabricated without any disturbing skin, but the host structure will be an inverse woodpile in this case. The potential of such a structure to support an efficient accelerating mode has yet to be investigated theoretically.

Ultimately, general advances in DLW technology are expected to rule out quality limitations caused by polymer shrinkage. Using stimulated emission depletion (STED) DLW (sDLW) [163], for example, a higher degree of cross linking and thus a higher mechanical stability of polymer templates with small feature sizes is anticipated. Improvements can, in particular, also be expected from advances in photoresist chemistry. Actually, resists that do not show any shrinkage effects already exist, like, e.g., chalcogenide glasses [136] or the positive resist AZ 9260 employed in [121]. Yet, their potential to stack a sufficient number of layers has to be explored and routes to transform the written templates into silicon structures have to be established. More likely, the development of completely new 3D resists for DLW will bring the breakthrough to achieve the desired optical quality for a functional woodpile accelerator.

Altogether, encouraging results regarding the fabrication of test samples and related considerations strongly support that the combination of DLW and SDI provides a promising route towards the fabrication of functional woodpile accelerator structures.

Chapter 9

Conclusions and Outlook

Photonic bandgap materials with embedded functional elements offer unique opportunities to control and manipulate the behavior of light. Based on this concept a large number of potential applications have been proposed. However, the fabrication of three-dimensional photonic bandgap materials at optical frequencies, and, even more, the introduction of functional elements therein, is extremely demanding.

In this thesis, this challenge has, for the first time, been addressed using a combination of direct laser writing and silicon double inversion. This inherently three-dimensional approach is characterized by its ability to create high-quality reasonable-size three-dimensional photonic bandgap structures operating in the near-infrared spectral region, while simultaneously preserving a high degree of structural flexibility. It has been demonstrated in this thesis that this flexibility can indeed be exploited to introduce functional elements into the fabricated photonic bandgap materials in a precise and controlled manner. This has been evidenced by the successful fabrication of various designed defect structures embedded inside three-dimensional silicon photonic crystals and the investigation of their structural and optical properties. All these structures are based on the woodpile geometry as host photonic bandgap material, which, when made out of silicon, exhibits a large and robust photonic bandgap.

One of the major fields of application envisioned for photonic bandgap materials is to provide the basis for the next generation optical signal processing and communication systems. It is therefore a crucial prerequisite for any corresponding fabrication method to be able to produce structures covering this operation wavelength regime. This is extremely challenging because of the small dimensions required for photonic bandgap materials operating in this regime. More precisely, lateral rod distances of $600\,\mathrm{nm}$ or below have to be realized for silicon woodpile structures to support a photonic bandgap around $1.55\,\mu\mathrm{m}$. Since a simple downscaling of previously reported results [24] has proven impossible, four different ideas have been combined in Chapter 5 of this thesis in order to make this regime accessible by direct laser writing and silicon double inversion. Namely, symmetry considerations, engineering of the rod aspect ratio, a proper choice of the employed photoresist, and tempering

of the silicon structures to slightly decrease the refractive index have been performed for this purpose. The fabricated structures exhibit a high structural quality as well as broad and prominent stop bands at telecom wavelengths. Evidence of the existence of a photonic bandgap in the fabricated silicon woodpile structures has been provided by comparison of the measured spectra with supplementary scattering-matrix and band-structure calculations performed for experimental structure parameters, for which a good overall qualitative agreement with the Fourier-transform infrared microscope spectrometer measurements is obtained. According to these calculations, the investigated structure exhibits a gap-midgap ratio of 6.9%, which is centered at $1.6\ \mu\mathrm{m}$ and includes $1.55\ \mu\mathrm{m}$ near the air-band edge. The result, that the technologically most relevant wavelength regime can indeed be accessed, makes this fabrication approach a promising candidate for actual applications, and therefore provides a strong motivation for efforts regarding the introduction of defect structures into photonic bandgap materials fabricated by direct laser writing and silicon double inversion.

The first step towards an experimental realization of functional defect structures inside silicon woodpile structures is the development of a proper defect design, which is compatible with all necessary fabrication steps. Although numerous theoretical defect design proposals exist for the woodpile structure, they do not consider the particular constraints imposed by direct laser writing and silicon double inversion. In Chapter 6 of this thesis, a basic defect element has been developed, which takes these constraints into account. It has been shown by numerical calculations, that, by adequately placing or concatenating such basic elements, both point defect cavities creating localized modes in the photonic bandgap as well as straight waveguides supporting guided modes can be obtained. Furthermore, it has been verified experimentally that functional elements based on this design are indeed accessible by direct laser writing and silicon double inversion. Different fabrication conditions for their introduction, both intrinsic by direct laser writing and extrinsic by focused ion beam milling, have been explored. In detail, isolated point defects, straight waveguides, and a complex network consisting of different bent, coupled and interconnected cavities and waveguide structures have been demonstrated. The high structural quality of these structures, both in the defect region and in the surrounding woodpile material, as well as the precise placement of the individual defect elements with respect to the woodpile lattice have been documented by scanning electron microscope inspection.

Nevertheless, for an actual quality assessment of *photonic* structures, scanning electron microscope inspection has to be complemented by *optical* characterization. Therefore, in Chapter 7 of this thesis, the propagation of light through straight vertical air-core waveguides based on the previously introduced design has been investigated. Waveguides are an essential element of integrated optical circuits, needed to efficiently connect the other functional components on the photonic chip. For optical characterization of the fabricated waveguide structures using a Fourier-transform infrared microscope spectrometer, the waveguides have been arranged in 4×4-supercell arrays in order to optimize the strength of the waveguide signature. The measurements reveal a pronounced photonic stop band superimposed by a dip in reflectance and a peak in transmittance, which is the characteristic signature of the inves-

tigated waveguide structure. These results have been compared to numerical band-structure and scattering-matrix calculations, which show a good overall qualitative agreement and nicely reproduce the spectral positions of the waveguide mode. Additional band structure calculations for the host woodpile reveal that a photonic bandgap with a gap-midgap ratio of 15.4% centered around $1.84\,\mu\mathrm{m}$ is supported by this structure. These results provide evidence of the propagation of light in designed air-core waveguides through more than five lattice constants of photonic bandgap woodpile material in stacking direction, which is more than a factor of two more than in the only previous realization of waveguides in three-dimensional photonic bandgap materials providing a transmittance measurement of the waveguide mode [21]. Further on, supplementary tuning of the defect signature has been demonstrated by cycle-wise re-infiltrating the waveguide-containing silicon woodpile structure with silica *via* atomic layer deposition and recording reflectance spectra after each cycle. The positions of the dips observed in the stop band agree well with corresponding midband positions of the waveguide mode obtained from band-structure calculations. This experimental route to shift the waveguide frequency to a desired spectral position can, for example, be used to fine-tune the operation wavelength of a fabricated device to match an externally specified wavelength.

Chapter 8 of this thesis finally focuses on a completely different potential application of defects in silicon woodpile photonic crystals with a photonic bandgap, namely a silicon woodpile particle-accelerator. Such photonic accelerators aim at providing an alternative to conventional accelerating technology, driven by the vision to create cheaper and more compact sources for high-energetic charged particle beams. The device investigated in this thesis is based on a complex waveguide geometry inside a silicon woodpile structure. Fabrication of this structure ideally exploits the advantages provided by direct laser writing and silicon double inversion, since high precision has to be obtained while at the same time relatively large samples have to be fabricated and many layers have to be stacked. In this thesis, the full geometry of such a woodpile-photonic-crystal accelerating segment comprising all central geometrical features has been fabricated for the first time and the quality of the fabricated structures has been assessed by scanning electron microscope inspection and Fourier-transform infrared microscope spectroscopy. While several issues remain to be addressed in order to create functional devices, the potential of direct laser writing and silicon double inversion to become the fabrication method of choice could be pointed out.
Future work will involve an identification and optical characterization of the accelerating mode for optimized prototypes in close collaboration with theory. Following this, first experiments to couple in the electron beam can be performed.

Generally, the results of this thesis provide a starting point for many exciting new experiments. On the one hand, as demonstrated in this thesis, more complex structures, like bent, interconnected, and coupled cavity waveguides can now readily be fabricated using direct laser writing and silicon double inversion. Their optical characterization forms an abundant field for future studies.
On the other hand, a deeper understanding of the *performance* of the fabricated structures is

needed. While in this thesis an upper bound for the losses inside the simple model system of a straight vertical waveguide has been determined, an experimental approach to measure losses exactly would provide the possibility to optimize the performance. Improvements in performance can be expected both from an optimization of the waveguide design and from further systematic improvement of the structural quality. Opportunities for such improvement are given by general advances in direct laser writing technology and photoresist development to reduce polymer shrinkage effects, as well as by new materials used for the intermediate step in the double inversion procedure, which do not show any significant shrinkage upon polymer removal.

In principle, both mentioned directions for future studies can be pursued using conventional Fourier-transform infrared microscope spectroscopy. More precisely, for performance measurements, arrays of waveguides with different lengths can be compared, thereby separating in-coupling losses from propagation losses. Likewise, for the characterization of complex waveguide structures, supercell arrays of the respective elements could again be fabricated to obtain a measurable signal. In the medium term, it would, however, be highly desirable to replace a characterization using conventional Fourier-transform infrared microscope spectroscopy with a measurement apparatus to selectively couple into individual defect elements. This renders the experimental supercell approach dispensable, thereby eliminating effects like broadening, which are caused by averaging over many slightly different structures. Furthermore, coupling from a free-space mode to the waveguides is not the ideal setting to investigate their properties. For two-dimensional photonic crystal waveguide structures, several elaborate coupling schemes involving tapered fibers, grating couplers, and adiabatic waveguide tapers are routinely in use to overcome this problem. For a sensitive characterization of three-dimensional components, such concepts will have to be translated into the three-dimensional case. This would also finally allow for the optical characterization of passive cavity structures in photonic bandgap materials without the need to deliberately deteriorate their optical properties in order to obtain a measurable signal. High-Q cavities could, for example, be laterally coupled to a linear waveguide. A possible experimental route to achieve the desired selective and efficient coupling to the input waveguide is to place a scanning near-field optical microscope probe directly on top of the waveguide aperture.

In addition, future experimental research on defect architectures in three-dimensional photonic bandgap materials will highly profit from advances on the theoretical side. Since large computational cells are required in order to calculate the theoretically expected optical properties of complex defect elements, calculations are rather costly. This highlights the strong demand for even more efficient computational methods to facilitate the design process for complex defect architectures and allow for an evaluation of corresponding experimentally obtained findings.
These suggestions for future experiments show that defect elements in three-dimensional photonic bandgap materials continue to be an active and exciting field of research, driven by their huge potential regarding prospective applications as well as by the simple fascination of precisely molding the flow of light.

Appendix A

Ellipsometry Measurements on Silicon Films

The optical properties of amorphous silicon films significantly depend on the respective film growth conditions, like the precursor gas, the type of reactor, and the process parameters [184]. Literature values can therefore not easily be adopted to the experimentally obtained amorphous silicon films deposited by CVD from disilane using the setup described in Subsection 4.2.2. In order to obtain reliable values for the refractive index $\mathrm{Re}(\mathrm{n_{Si}})$ and the extinction coefficient $\mathrm{Im}(\mathrm{n_{Si}})$ of these films, ellipsometry measurements and ellipsometric data analysis have been performed in cooperation with F. Peiris (Kenyon College).

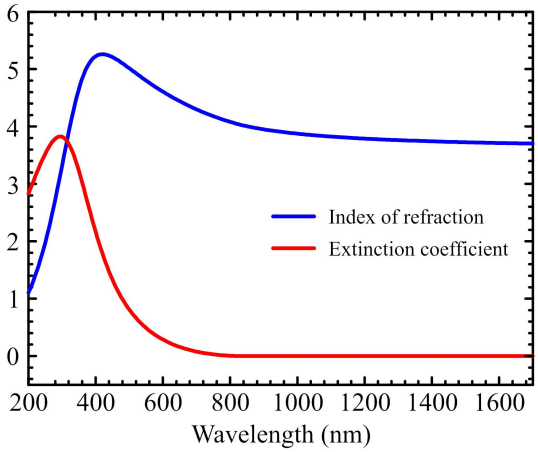

Figure A.1: Optical properties of a silicon film grown by CVD from disilane onto a glass substrate. Ellipsometry measurement and ellipsometric data analysis: F. Peiris, Kenyon College.

Six different silicon films with varying thickness grown on conventional glass cover slides following the procedure described in Subsection 4.2.2 have been investigated. The spectral range covered by the employed ellipsometer (variable-angle spectroscopic ellipsometer from J. A. Woollam) is 200–$1800\,\mathrm{nm}$. Corresponding results for the refractive index and the extinction coefficient are depicted in Fig. A.1 for a representative sample with a thickness of

approx. $163\,\mathrm{nm}$. For all other samples almost identical results have been obtained.
The data plotted in Fig. A.1 serves as a starting point for ε-values used in band-structure and scattering-matrix calculations performed to compare the spectra of actually fabricated amorphous silicon 3D PhC samples with corresponding theoretical expectations. At a wavelength of $1.55\,\mu\mathrm{m}$, for example, the derived value for $\mathrm{Re}(\mathrm{n_{Si}})$ is 3.72, corresponding to a dielectric constant of $\varepsilon = 13.84$, while no non-zero value for $\mathrm{Im}(\mathrm{n_{Si}})$ has been retrieved at this wavelength. Correspondingly, $\mathrm{Im}(\mathrm{n_{Si}})$ is neglected in the calculations.

Appendix B

FTIR Measurements on Finite Footprint Samples

In transmittance, the stop bands of the silicon woodpile PhCs investigated in this thesis are systematically deeper in theory (scattering-matrix calculations) than in the experiment (FTIR transmittance measurements) by several orders of magnitude. In this section it is demonstrated that this discrepancy is not entirely due to sample imperfections, like deviation from perfect periodicity and surface roughness, but that the actually observed minimum transmittance levels are determined by the measurement itself. Limiting factors for the maximum background suppression (*i.e.*, the minimum transmittance level) achievable in a transmittance measurement are issues of photometric accuracy characteristic for FTIR spectrometry [144] on the one hand, and, on the other hand, the finite footprint of the fabricated structures (usually approx. $40\,\mu\mathrm{m} \times 40\,\mu\mathrm{m}$), which allows a small fraction of the incident light to go *around* instead of *through* the sample, presumably by diffraction at the sample edges.

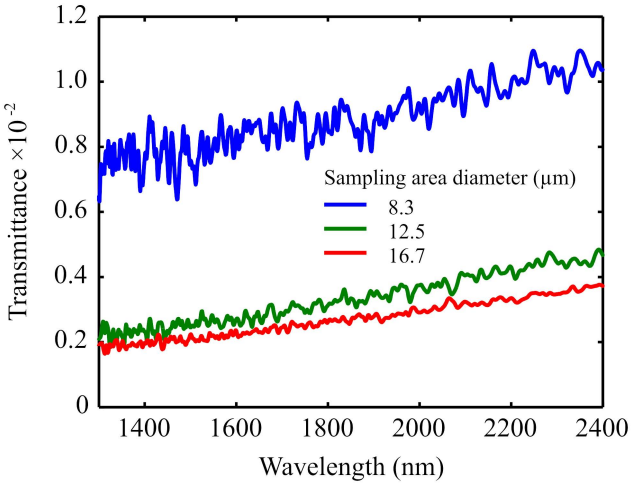

Figure B.1: Transmittance of a $40\,\mu\mathrm{m} \times 40\,\mu\mathrm{m}$ footprint $200\,\mathrm{nm}$ thick gold pad on a glass substrate for three different diameters of the employed aperture.

In order to allow for a quantitative understanding of the minimum transmittance levels obtained in the stop band regions of finite footprint PBG-materials, reference measurements have been performed on opaque $200\,\mathrm{nm}$ thick square shaped gold pads with footprints of $40\,\mu\mathrm{m} \times 40\,\mu\mathrm{m}$. These gold pads have been fabricated on a conventional microscope cover slide by electron-beam lithography, gold evaporation, and a lift-off procedure by M. Decker. FTIR transmittance spectra of such a gold pad are displayed in Fig. B.1 for unpolarized light and three different diameters of the employed aperture.
The blue curve shows the background transmittance level relevant for the measurements on PBG-materials operating at telecom wavelengths presented in Section 5.2, for which an aperture with $8.3\,\mu\mathrm{m}$ sampling area diameter has been used. The reference transmittance values are in excellent agreement with the minimum transmittance levels found for the woodpile structures (see Fig. 5.10 (a)). Based on these findings, additional transmittance measurements have been performed on the gold pads for different diameters of the employed aperture in order to optimize the measurement conditions for successive experiments. Remarkably, as a result of the two different limiting factors, the optimum background suppression is not obtained for the smallest provided aperture ($8.3\,\mu\mathrm{m}$ sampling area diameter), but for the aperture with $16.7\,\mu\mathrm{m}$ sampling area diameter. The corresponding curve is shown in red in Fig. B.1. As expected for a larger aperture the noise of the measurement is reduced as well. The background transmittance measured for an intermediate aperture diameter with sampling area of $12.5\,\mu\mathrm{m}$ is also depicted in Fig. B.1 (green curve) for comparison.
The transmittance measurements for the waveguide structures in Chapter 7 have been performed using the optimized conditions. Given the small peak transmittance values (approximately 0.0045) for the waveguide mode (compare Fig.7.2 (a)), an efficient background suppression is essential for these measurements to be able to detect the waveguide signature.
The spectra recorded for the woodpile particle accelerator structures in Chapter 8 cannot directly be compared to the background measurements shown in Fig. B.1, since these structures have different footprints (approx. $20\,\mu\mathrm{m} \times 80\,\mu\mathrm{m}$). Qualitatively, a less effective background transmittance is expected for these structures due to their small lateral dimensions, which is consistent with experimental findings (see Fig. 8.6).

Bibliography

[1] J. F. von Schönberg, *Die Schildbürger* (1598).

[2] S. John, *Strong Localization of Photons in Certain Disordered Dielectric Superlattices*, Phys. Rev. **58** (23), 2486 (1987).

[3] E. Yablonovitch, *Inhibited Spontaneous Emission in Solid-State Physics and Electronics*, Phys. Rev. **58** (20), 2059 (1987).

[4] S. Fan, P. R. Villeneuve, J. D. Joannopoulos, and H. A. Haus, *Channel drop filters in photonic crystals*, Opt. Express **3** (1), 4 (1998).

[5] M. Lončar, Axel Scherer, and Y. Qiu, *Photonic crystal laser sources for chemical detection*, Appl. Phys. Lett. **82** (26), 4648 (2003).

[6] O. Painter, R. K. Lee, A. Scherer, A. Yariv, J. D. O'Brien, P. D. Dapkus, and I. Kim, *Two-Dimensional Photonic Band-Gap Defect Mode Laser*, Science **284** (5421), 1819 (1999).

[7] H.-G. Park, S.-H. Kim, S.-H. Kwon, Y.-G. Ju, J.-K. Yang, J.-H. Baek, S.-B. Kim, and Y.-H. Lee, *Electrically Driven Single-Cell Photonic Crystal Laser*, Science **305** (5689), 1444 (2004).

[8] M. Soljačić, M. Ibanescu, S. G. Johnson, Y. Fink, and J. D. Joannopoulos, *Optimal bistable switching in nonlinear photonic crystals*, Phys. Rev. E **66** (5), 055601 (2002).

[9] A. Mekis, J. C. Chen, I. Kurland, S. Fan, P. R. Villeneuve, and J. D. Joannopoulos, *High Transmission through Sharp Bends in Photonic Crystal Waveguides*, Phys. Rev. Lett. **77**, 3787 (1996).

[10] S.-Y. Lin, E. Chow, V. Hietala, P. R. Villeneuve, and J. D. Joannopoulos, *Experimental Demonstration of Guiding and Bending of Electromagnetic Waves in a Photonic Crystal*, Science **282** (5387), 274 (1998).

[11] S. Fan, S. G. Johnson, J. D. Joannopoulos, C. Manolatou, and H. A. Haus, *Waveguide branches in photonic crystals*, J. Opt. Soc. Am. B **18** (2), 162 (2001).

[12] A. Chutinan and S. Noda, *Highly confined waveguides and waveguide bends in three-dimensional photonic crystal*, Appl. Phys. Lett. **75** (24), 3739 (1999).

[13] Z.-Y. Li and K.-M. Ho, *Waveguides in three-dimensional layer-by-layer photonic crystals*, J. Opt. Soc. Am. B **20** (5), 801 (2003).

[14] D. Roundy, E. Lidorikis, and J. D. Joannopoulos, *Polarization-selective waveguide bends in a photonic crystal structure with layered square symmetry*, J. Appl. Phys. **96** (12), 7750 (2004).

[15] C. Sell, C. Christensen, J. Muehlmeier, G. Tuttle, Z.-Y. Li, and K.-M. Ho, *Waveguide networks in three-dimensional layer-by-layer photonic crystals*, Appl. Phys. Lett. **84** (23), 4605 (2004).

[16] A. Chutinan and S. John, *Light localization for broadband integrated optics in three dimensions*, Phys. Rev. B **72** (16), 161316(R) (2005).

[17] M. Soljačić, S. G. Johnson, S. Fan, M. Ibanescu, E. Ippen, and J. D. Joannopoulos, *Photonic-crystal slow-light enhancement of nonlinear phase sensitivity*, J. Opt. Soc. Am. B **19** (9), 2052 (2002).

[18] A. Yariv, Y. Xu, R. K. Lee, and Axel Scherer, *Coupled-resonator optical waveguide: a proposal and analysis*, Opt. Lett. **24** (11), 711 (1999).

[19] B. M. Cowan, *Three-dimensional dielectric photonic crystal structures for laser-driven acceleration*, Phys. Rev. Spec. Top. Accel Beams **11** (1), 011301 (2008).

[20] S. A. Rinne, F. García-Santamaría, and P. V. Braun, *Embedded cavities and waveguides in three-dimensional silicon photonic crystals*, Nat. Photonics **2** (1), 52 (2008).

[21] S. Kawashima, K. Ishizaki, and S. Noda, *Light propagation in three-dimensional photonic crystals*, Opt. Express **18** (1), 386 (2010).

[22] S. Maruo, O. Nakamura, and S. Kawata, *Three-dimensional microfabrication with two-photon-absorbed photopolymerization*, Opt. Lett. **22** (2), 132 (1997).

[23] M. Deubel, G. von Freymann, M. Wegener, S. Pereira, K. Busch, and C. M. Soukoulis, *Direct laser writing of three-dimensional photonic-crystal templates for telecommunications*, Nat. Mater. **3** (7), 444 (2004).

[24] N. Tétreault, G. von Freymann, M. Deubel, M. Hermatschweiler, F. Pérez-Willard, S. John, M. Wegener, and G. A. Ozin, *New Route to Three-Dimensional Photonic Bandgap Materials: Silicon Double Inversion of Polymer Templates*, Adv. Mat. **18** (4), 457 (2006).

[25] M. Hermatschweiler, A. Ledermann, G. A. Ozin, M. Wegener, and G. von Freymann, *Fabrication of Silicon Inverse Woodpile Photonic Crystals*, Adv. Funct. Mat. **17** (14), 2273 (2007).

[26] N. Yamamoto, S. Noda, and A. Chutinan, *Development of One Period of a Three-Dimensional Photonic Crystal in the 5-10 μm Wavelength Region by Wafer Fusion and Laser Beam Diffraction Pattern Observation Techniques*, Jpn. J. Appl. Phys. (Part 2) **37** (9A/B), L1052 (1998).

[27] S. Noda, K. Tomoda, N. Yamamoto, and A. Chutinan, *Full Three-Dimensional Photonic Bandgap Crystals at Near-Infrared Wavelengths*, Science **289** (5479), 604 (2000).

[28] S.-Y. Lin, J. G. Fleming, D. L. Hetherington, B. K. Smith, R. Biswas, K. M. Ho, M. M. Sigalas, W. Zubrzycki, S. R. Kurtz, and J. Bur, *A three-dimensional photonic crystal operating at infrared wavelengths*, Nature **394** (6690), 251 (1998).

[29] G. Subramania, Y.-J. Lee, A. J. Fischer, and D. D. Koleske, *Log-Pile TiO_2 Photonic Crystal for Light Control at Near-UV and Visible Wavelengths*, Adv. Mat. **22** (4), 487 (2009).

[30] K. Aoki, H. T. Miyazaki, H. Hirayama, K. Inoshita, T. Baba, K. Sakoda, N. Shinya, and Y. Aoyagi, *Microassembly of semiconductor three-dimensional photonic crystals*, Nat. Mater. **2** (2), 117 (2003).

[31] C. Lopez, *Materials Aspects of Photonic Crystals*, Adv. Mat. **15** (20), 1690 (2003).

[32] Emanuel Istrate and Edward H. Sargent, *Photonic crystal heterostructures and interfaces*, Rev. Mod. Phys. **78** (2), 455 (2006).

[33] P. V. Braun, S. A. Rinne, and F. García-Santamaría, *Introducing Defects in 3D Photonic Crystals: State of the Art*, Adv. Mat. **18** (20), 2665 (2006).

[34] K. A. Arpin, A. Mihi, H. T. Johnson, A. J. Baca, J. A. Rogers, J. A. Lewis, and P. V. Braun, *Multidimensional Architectures for Functional Optical Devices*, Adv. Mat. **22** (10), 1084 (2010).

[35] V. Kuzmiak, A. A. Maradudin, and F. Pincemin, *Photonic band structures of two-dimensional systems containing metallic components*, Phys. Rev. B **50** (23), 16835 (1994).

[36] V. Poborchii, T. Tada, T. Kanayama, and A. Moroz, *Silver-coated silicon pillar photonic crystals: Enhancement of a photonic band gap*, Appl. Phys. Lett. **82** (4), 508 (2003).

[37] J. D. Joannopoulos, J. G. Johnson, J. N. Winn, and R. D. Meade, *Photonic Crystals - Molding the Flow of Light* (Princeton University Press, Princeton, NJ, 2008), second edition.

[38] J. B. Pendry, A. J. Holden, D. J. Robbins, and W. J. Stewart, *Magnetism from Conductors and Enhanced Nonlinear Phenomena*, IEEE Trans. Microw. Theory Tech. **47** (11), 2075 (1999).

[39] N. W. Ashcroft and N. D. Mermin, *Solid State Physics*, Fort Worth (Harcourt Brace College Publishers, 1976).

[40] K. Busch and S. John, *Photonic band gap formation in certain self-organizing systems*, Phys. Rev. E **58** (3), 3896 (1998).

[41] K. Sakoda, *Optical Properties of Photonic Crystals* (Springer Verlag, Berlin, 2001).

[42] R. D. Meade, K. D. Brommer, A. M. Rappe, and J. D. Joannopoulos, *Photonic bound states in periodic dielectric materials*, Phys. Rev. B **44** (24), 13772 (1991).

[43] B. Simon, *The bound state of weakly coupled Schrödinger operators in one and two dimensions*, Ann. of Phys. **97** (2), 279 (1976).

[44] K. Yang and M. de Llano, *Simple variational proof that any two-dimensional potential well supports at least one bound state*, Am. J. Phys. **57** (1), 85 (1989).

[45] E. Yablonovitch, T. J. Gmitter, R. D. Meade, A. M. Rappe, K. D. Brommer, and J. D. Joannopoulos, *Donor and acceptor modes in photonic band structure*, Phys. Rev. Lett. **67** (24), 3380 (1991).

[46] S. Kawashima, M. Okano, M. Imada, and S. Noda, *Design of compound-defect waveguides in three-dimensional photonic crystals*, Opt. Express **14** (13), 6303 (2006).

[47] O. Painter and K. Srinivasan, *Localized defect states in two-dimensional photonic crystal slab waveguides: A simple model based upon symmetry analysis*, Phys. Rev. B **68** (3), 035110 (2003).

[48] M. L. Gorodetsky, A. A. Savchenkov, and V. S. Ilchenko, *Ultimate Q of optical microsphere resonators*, Opt. Lett. **21** (7), 453 (1996).

[49] Y. Akahane, T. Asano, B. S. Song, and S. Noda, *High-Q photonic nanocavity in a two-dimensional photonic crystal*, Nature **425** (6961), 944 (2003).

[50] Y. Arakawa, A. Tandaechanurat, S. Iwamoto, M. Nomura, and D. Guimard, *Advances in 3D photonic crystal nanocavity with quantum dots*, in *Quantum Sensing and Nanophotonic Devices VII*, edited by M. Razeghi, R. Sudharsanan, and G. J. Brown, volume 7608 (2010).

[51] E. M. Purcell, *Spontaneous emission probabilities at radio frequencies*, Phys. Rev. **69** (11-1), 681 (1946).

[52] R. Ramaswami, K. N. Sivarajan, and G. H. Sasaki, *Optical Networks: A Practical Perspective* (Morgan Kaufmann, 2009), third edition.

[53] R. D. Meade, A. Devenyi, J. D. Joannopoulos, O. L. Alerhand, D. A. Smith, and K. Kash, *Novel applications of photonic band gap materials: Low-loss bends and high Q cavities*, J. Appl. Phys. **75** (9), 4753 (1994).

[54] K. M. Ho, C. T. Chan, and C. M. Soukoulis, *Existence of a photonic gap in periodic dielectric structures*, Phys. Rev. **65** (25), 3152 (1990).

[55] E. Yablonovitch, T. J. Gmitter, and K. M. Leung, *Photonic Band Structure : The Face-Centered-Cubic Case Employing Nonspherical Atoms*, Phys. Rev. **67** (17), 2295 (1991).

[56] K. M. Ho, C. T. Chan, C. M. Soukoulis, R. Biswas, and M. Sigalas, *Photonic band gaps in three dimensions: New layer-by-layer periodic structures*, Solid State Commun. **89** (5), 413 (1994).

[57] H. S. Sözüer and J. P. Dowling, *Photonic Band Calculations for Woodpile Structures*, J. Mod. Opt. **41** (2), 231 (1994).

[58] O. Toader, M. Berciu, and S. John, *Photonic Band Gaps Based on Tetragonal Lattices of Slanted Pores*, Phys. Rev. Lett. **90** (23), 233901 (2003).

[59] O. Toader and S. John, *Slanted-pore photonic band-gap materials*, Phys. Rev. E **71** (3), 036605 (2005).

[60] H. S. Sözüer, J. W. Haus, and R. Inguva, *Photonic bands: Convergence problems with the plane-wave method*, Phys. Rev. B **45** (24), 13962 (1992).

[61] A. Blanco, E. Chomski, S. Grabtchak, M. Ibisate, S. John, S. W. Leonard, C. Lopez, F. Meseguer, H. Miguez, J. P. Mondia, G. A. Ozin, O. Toader, and H. M. van Driel, *Large-scale synthesis of a silicon photonic crystal with a complete three-dimensional bandgap near 1,5 micrometres*, Nature **405** (6785), 437 (2000).

[62] S. G. Johnson and J. D. Joannopoulos, *Three-dimensionally periodic dielectric layered structure with omnidirectional photonic band gap*, Appl. Phys. Lett. **77** (22), 3490 (2000).

[63] V. Berger, O. Gauthier-Lafaye, and E. Costard, *Photonic band gaps and holography*, J. Appl. Phys. **82** (1), 60 (1997).

[64] O. Toader and S. John, *Proposed Square Spiral Microfabrication Architecture for Large Three-Dimensional Photonic Band Gap Crystals*, Science **292** (5519), 1133 (2001).

[65] A. Chutinan and S. Noda, *Spiral three-dimensional photonic-band-gap structures*, Phys. Rev. B **57** (4), R2006 (1998).

[66] K. Edagawa, S. Kanoko, and M. Notomi, *Photonic Amorphous Diamond Structure with a 3D Photonic Band Gap*, Phys. Rev. Lett. **100** (1), 013901 (2008).

[67] Y. Lin and P. R. Herman, *Effect of structural variation on the photonic band gap in woodpile photonic crystal with body-centered cubic symmetry*, J. Appl. Phys. **98** (6), 063104 (2005).

[68] E. Özbay, G. Tuttle, M. Sigalas, C. M. Soukoulis, and K. M. Ho, *Defect structures in a layer-by-layer photonic band-gap crystal*, Phys. Rev. B **51** (20), 13961 (1995).

[69] A. Chelnokov, S. Rowson, J.-M. Lourtioz, L. Duvillaret, and J.-L. Coutaz, *Light controllable defect modes in three-dimensional photonic crystal*, Electron. Lett. **34** (20), 1965 (1998).

[70] S. Y. Lin, J. G. Fleming, M. M. Sigalas, R. Biswas, and K. M. Ho, *Photonic band-gap microcavities in three dimensions*, Phys. Rev. B **59** (24), 579 (1999).

[71] M. Okano, A. Chutinan, and S. Noda, *Analysis and design of single-defect cavities in a three-dimensional photonic crystal*, Phys. Rev. B **66** (16), 165211 (2002).

[72] M. Okano and S. Noda, *Analysis of multimode point-defect cavities in three-dimensional photonic crystals using group theory in frequency and time domains*, Phys. Rev. B **70** (12), 125105 (2004).

[73] S. Kawashima, L. H. Lee, M. Okano, M. Imada, and S. Noda, *Design of donor-type line-defect waveguides in three-dimensional photonic crystals*, Opt. Express **13** (24), 9774 (2005).

[74] M. Bayindir, E. Ozbay, B. Temelkuran, M. M. Sigalas, C. M. Soukoulis, R. Biswas, and K. M. Ho, *Guiding, bending, and splitting of electromagnetic waves in highly confined photonic crystal waveguides*, Phys. Rev. B **63** (8), 081107 (2001).

[75] M. Okano, S. Kako, and S. Noda, *Coupling between a point-defect cavity and a line-defect waveguide in three-dimensional photonic crystal*, Phys. Rev. B **68** (23), 235110 (2003).

[76] M. M. Sigalas and R. Biswas, *Slot defect in three-dimensional photonic crystals*, Phys. Rev. B **78** (3), 033101 (2008).

[77] M. Bayindir and E. Ozbay, *Dropping of electromagnetic waves through localized modes in three-dimensional photonic band gap structures*, Appl. Phys. Lett. **81** (24), 4514 (2002).

[78] M. Bayindir, B. Temelkuran, and E. Ozbay, *Photonic-crystal-based beam splitters*, Appl. Phys. Lett. **77** (24), 3902 (2000).

[79] M. Bayindir, B. Temelkuran, and E. Ozbay, *Propagation of photons by hopping: A waveguiding mechanism through localized coupled cavities in three-dimensional photonic crystals*, Phys. Rev. B **61** (18), R11 855 (2000).

[80] S. Ogawa, M. Imada, S. Yoshimoto, M. Okano, and S. Noda, *Control of Light Emission by 3D Photonic Crystals*, Science **305** (5681), 227 (2004).

[81] M. Qi, E. Lidorikis, P. T. Rakich, S. G. Johnson, J. D. Joannopoulos, E. P. Ippen, and H. I. Smith, *A three-dimensional optical photonic crystal with designed point defects*, Nature **429** (6991), 538 (2004).

[82] M. Imada, L. H. Lee, M. Okano, S. Kawashima, and S. Noda, *Development of three-dimensional photonic-crystal waveguides at optical-communication wavelengths*, Appl. Phys. Lett. **88** (17), 171107 (2006).

[83] S. Ogawa, K. Ishizaki, T. Furukawa, and S. Noda, *Spontaneous emission control by 17 layers of three-dimensional photonic crystals*, Electron. Lett. **44** (5), 377 (2008).

[84] K. Ishizaki and S. Noda, *Manipulation of photons at the surface of three-dimensional photonic crystals*, Nature **460** (7253), 367 (2009).

[85] G. Subramania, Y.-J. Lee, and A. J. Fischer, *Silicon-Based Near-Visible Logpile Photonic Crystal*, Adv. Mat. **22** (37), 4180 (2010).

[86] V. Lehmann, *The Physics of Macropore Formation in Low Doped n-Type Silicon*, J. Electrochem. Soc. **140** (10), 2836 (1993).

[87] G. Mertens, R. B. Wehrspohn, H.-S. Kitzerowa, S. Matthias, C. Jamois, and U. Gösele, *Tunable defect mode in a three-dimensional photonic crystal*, Appl. Phys. Lett. **87** (24), 241108 (2005).

[88] S. Takahashi, K. Suzuki, M. Okano, M. Imada, T. Nakamori, Y. Ota, K. Ishizaki, and S. Noda, *Direct creation of three-dimensional photonic crystals by a top-down approach*, Nat. Mater. **8** (9), 721 (2009).

[89] F. Laermer and A. Schilp of Robert Bosch GmbH, *US Patent 5,501,893: Method of Anisotropically Etching Silicon* (1996).

[90] L. A. Woldering, R. W. Tjerkstra, H. V. Jansen, I. D. Setija, and W. L. Vos, *Periodic arrays of deep nanopores made in silicon with reactive ion etching and deep UV lithography*, Nanotechnology **19** (14), 145304 (2008).

[91] R. W. Tjerkstra, L. A. Woldering, J. M. van den Broek, J. J. Kelly, F. Roozeboom, I. D. Setija, and W. L. Vos, (submitted 2010).

[92] S. R. Kennedy, M. J. Brett, O. Toader, and S. John, *Fabrication of Tetragonal Square Spiral Photonic Crystals*, Nano Lett. **2** (1), 59 (2002).

[93] A. C. van Popta, M. J. Brett, and J. C. Sit, *Double-handed circular Bragg phenomena in polygonal helix thin films*, J. Appl. Phys. **98** (8), 083517 (2005).

[94] M. O. Jensen and M. J. Brett, *Functional Pattern Engineering in Glancing Angle Deposition Thin Films*, J. Nanosci. Nanotechnol. **5** (5), 723 (2005).

[95] S. Kawakami, *Fabrication of submicrometre 3D periodic structures composed of Si/SiO_2*, Electron. Lett. **33** (14), 1260 (1997).

[96] S. Kawakami, T. Sato, K. Miura, Y. Ohtera, T. Kawashima, and H. Ohkubo, *3-D photonic-crystal heterostructures: fabrication and in-line resonator*, IEEE Photonics Technol. Lett. **15** (6), 816 (2003).

[97] O. Hanaizumi, Y. Ohtera, T. Sato, and S. Kawakami, *Propagation of light beams along line defects formed in a-Si/SiO_2 three-dimensional photonic crystals: Fabrication and observation*, Appl. Phys. Lett. **74** (6), 777 (1999).

[98] F. García-Santamaría, H. T. Miyazaki, A. Urquía, M. Ibisate, M. Belmonte, N. Shinya, F. Meseguer, and C. López, *Nanorobotic Manipulation of Microspheres for On-Chip Diamond Architectures*, Adv. Mat. **14** (16), 1144 (2002).

[99] H. Morishita and Y. Hatamura, *Development of ultra micromanipulator system under stereo SEM observation*, Int. Conf. Intelligent Robots and Systems **3** (3), 1717 (1993).

[100] K. Aoki, D. Guimard, M. Nishioka, M. Nomura, S. Iwamoto, and Y. Arakawa, *Coupling of quantum-dot light emission with a three-dimensional photonic-crystal nanocavity*, Nat. Photonics **2** (11), 688 (2008).

[101] A. Tandaechanurat, S. Ishida, K. Aoki, D. Guimard, M. Nomura, S. Iwamoto, and Y. Arakawa, *Demonstration of high-Q (>8600) three-dimensional photonic crystal nanocavity embedding quantum dots*, Appl. Phys. Lett. **94** (17), 171115 (2009).

[102] G. M. Gratson, F. García-Santamaría, V. Lousse, M. Xu, S. Fan, J. A. Lewis, and P. V. Braun, *Direct-Write Assembly of Three-Dimensional Photonic Crystals: Conversion of Polymer Scaffolds to Silicon Hollow-Woodpile Structures*, Adv. Mat. **18** (4), 461 (2006).

[103] H.-B. Sun, S. Matsuo, and H. Misawa, *Three-dimensional photonic crystal structures achieved with two-photon-absorption photopolymerization of resin*, Appl. Phys. Lett. **74** (6), 786 (1999).

[104] Y. Lin, P. R. Herman, and K. Darmawikarta, *Design and holographic fabrication of tetragonal and cubic photonic crystals with phase mask: toward the mass-production of three-dimensional photonic crystals*, Appl. Phys. Lett. **86** (7), 071117 (2005).

[105] Y. Lin, A. Harb, K. Lozano, D. Xu, and K. P. Chen, *Five beam holographic lithography for simultaneous fabrication of three dimensional photonic crystal templates and line defects using phase tunable diffractive optical element*, Opt. Express **17** (19), 16625 (2009).

[106] M. Deubel, *Three-Dimensional Photonic Crystals via Direct Laser Writing: Fabrication and Characterization*, Dissertation, Universität Karlsruhe (TH), Institut für Angewandte Physik (2006).

[107] V. Ramanan, E. Nelson, A. Brzezinski, P. V. Braun, and P. Wiltzius, *Three dimensional silicon-air photonic crystals with controlled defects using interference lithography*, Appl. Phys. Lett. **92** (17), 173304 (2008).

[108] W. Ehrfeld and A. Schmidt, *Recent developments in deep x-ray lithography*, J. Vac. Sci. Technol. B **16** (6), 3526 (1998).

[109] F. Romanato, R. Kumar, and E. Di Fabrizio, *Interface lithography: a hybrid lithographic approach for the fabrication of patterns embedded in three-dimensional structures*, Nanotechnology **16** (1), 40 (2005).

[110] A. P. Philipse, *Solid opaline packings of colloidal silica spheres*, J. Mat. Sci. Lett. **8** (12), 1371 (1989).

[111] O. D. Velev, T. A. Jede, R. F. Lobo, and A. M. Lenhoff, *Porous Silica via Colloidal Crystallization*, Nature **389** (6650), 447 (1997).

[112] R. D. Pradhan and I. Inanç, *Impurity modes in the optical stop bands of doped colloidal crystals*, Phys. Rev. B **54** (19), 13721 (1996).

[113] N. Tétreault, A. Mihi, H. Míguez, I. Rodríguez, G. A. Ozin, F. Meseguer, and V. Kitaev, *Dielectric Planar Defects in Colloidal Photonic Crystal Films*, Adv. Mat. **16** (4), 346 (2004).

[114] E. Vekris, V. Kitaev, G. von Freymann, D. D. Perovic, J. S. Aitchison, and G. A. Ozin, *Buried Linear Extrinsic Defects in Colloidal Photonic Crystals*, Adv. Mat. **17** (10), 1269 (2005).

[115] W. Lee, S. A. Pruzinsky, and P. V. Braun, *Multi-Photon Polymerization of Waveguide Structures Within Three-Dimensional Photonic Crystals*, Adv. Mat. **14** (4), 271 (2002).

[116] H. B. Sun, V. Mizeikis, Y. Yu, S. Juodkazis, J. Y. Ye, S. Matsuo, and H. Misawa, *Microcavities in polymeric photonic crystals*, Appl. Phys. Lett. **79** (1), 1 (2001).

[117] M. Deubel, M. Wegener, S. Linden, G. von Freymann, and S. John, *3D–2D–3D photonic crystal heterostructures fabricated by direct laser writing*, Opt. Lett. **31** (6), 805 (2006).

[118] M. Thiel, M. Decker, M. Deubel, M. Wegener, S. Linden, and G. von Freymann, *Polarization Stop Bands in Chiral Polymeric Three-Dimensional Photonic Crystals*, Adv. Mat. **19** (2), 207 (2007).

[119] A. Ledermann, L. Cademartiri, M. Hermatschweiler, C. Toninelli, G. A. Ozin, D. S. Wiersma, M. Wegener, and G. von Freymann, *Three-dimensional silicon inverse photonic quasicrystals for infrared wavelengths*, Nat. Mater. **5** (12), 942 (2006).

[120] M. S. Rill, C. Plet, M. Thiel, I. Staude, G. von Freymann, S. Linden, and M. Wegener, *Photonic metamaterials by direct laser writing and silver chemical vapour deposition*, Nat. Mater. **7** (7), 543 (2008).

[121] J. K. Gansel, M. Thiel, M. S. Rill, M. Decker, K. Bade, V. Saile, G. von Freymann, S. Linden, and M. Wegener, *Gold Helix Photonic Metamaterial as Broadband Circular Polarizer*, Science **325** (5947), 1513 (2009).

[122] T. Ergin, N. Stenger, P. Brenner, J. B. Pendry, and M. Wegener, *Three-Dimensional Invisibility Cloak at Optical Wavelengths*, Science **328** (5976), 337 (2010).

[123] G. von Freymann, A. Ledermann, M. Thiel, I. Staude, S. Essig, K. Busch, and M. Wegener, *Three-Dimensional Nanostructures for Photonics*, Adv. Funct. Mat. **20** (7), 1038 (2010).

[124] A. Ledermann, *Design, Fabrication, and Characterisation of Three-Dimensional Photonic Quasicrystals*, Dissertation, Karlsruher Institut für Technologie, Institut für Angewandte Physik (2010).

[125] M. Göppert-Mayer, *Über Elementarakte mit zwei Quantensprüngen*, Ann. Phys. **9** (2), 273 (1931).

[126] A. Ledermann, M. Wegener, and G. von Freymann, *Rhombicuboctahedral Three-Dimensional Photonic Quasicrystals*, Adv. Mat. **22** (21), 2363 (2010).

[127] M. C. Wanke, O. Lehmann, K. Müller, Q. Wen, and M. Stuke, *Laser Rapid Prototyping of Photonic Band-Gap Microstructures*, Science **275** (5304), 1284 (1997).

[128] S. Maruo and K. Ikuta, *Three-dimensional microfabrication by use of single-photon-absorbed polymerization*, Appl. Phys. Lett. **76** (19), 2656 (2000).

[129] K. Y. Lee, N. LaBianca, S. A. Rishton, S. Zolgharnain, J. D. Gelorme, J. Shaw, and T. H.-P. Chang, *Micromachining applications of a high resolution ultrathick photoresist*, J. Vac. Sci. Technol. B **13** (6), 3012 (1995).

[130] J. D. Gelorme, R. J. Cox, and S. A. R. Gutierrez, *US Patent 4,882,245: Photoresist composition and printed circuit boards and packages made therewith* (1989).

[131] U. Pietsch (Universität Giessen), *private communication*.

[132] M. Thiel, *Design, Fabrication, and Characterization of Three-Dimensional Chiral Photonic Crystals*, Dissertation, Karlsruher Institut für Technologie, Institut für Angewandte Physik (2010).

[133] Nanoscribe GmbH, *private communication*.

[134] I. Staude, M. Thiel, S. Essig, C. Wolff, K. Busch, G. von Freymann, and M. Wegener, *Fabrication and characterization of silicon woodpile photonic crystals with a complete bandgap at telecom wavelengths*, Opt. Lett. **35** (7), 1094 (2010).

[135] I. Staude, G. von Freymann, S. Essig, K. Busch, and M. Wegener, *Waveguides in three-dimensional photonic-band-gap materials by direct laser writing and silicon double inversion*, Opt. Lett. **36** (1), 67 (2011).

[136] S. Wong, M. Deubel, F. Pérez-Willard, S. John, G. A. Ozin, M. Wegener, and G. von Freymann, *Direct Laser Writing of Three-Dimensional Photonic Crystals with a Complete Photonic Bandgap in Chalcogenide Glasses*, Adv. Mat. **18** (3), 265 (2006).

[137] S. Wong, O. Kiowski, M. Kappes, J. K. N. Lindner, N. Mandal, Frank C. Peiris, G. A. Ozin, M. Thiel, M. Braun, M. Wegener, and G. von Freymann, *Spatially Localized Photoluminescence at 1.5 Micrometers Wavelength in Direct Laser Written Optical Nanostructures*, Adv. Mat. **20** (21), 4097 (2008).

[138] 2004 IC Technology: IC Knowledge LLC, *Technology Backgrounder: Atomic Layer Deposition*, www.icknowledge.com (2004).

[139] D. J. Ehrlich and J. Melngailis, *Fast room-temperature growth of SiO_2 films by molecular-layer dosing*, Appl. Phys. Lett. **58** (23), 2675 (1991).

[140] R. Visser, *Acoustic measurements on real and synthetic reservoir rock*, Dissertation, Delft University of Technology (1988).

[141] M. Gueye, E. Scheid, P. Taurines, P. Duverneuil, D. Bielle-Daspet, and J. P. Couderc, *Silicon Deposition from Disilane: Experimental Study and Modelling*, J. de Physique II **1** (C2), 63 (1991).

[142] K. L. Choy, *Chemical vapor deposition of coatings*, Progress in Mat. Sci. **48** (2), 57 (2003).

[143] A. Blanco and C. Lopéz, *Silicon onion-layer nanostructures arranged in three dimensions*, Adv. Mat. **18** (12), 1593 (2006).

[144] P. R. Griffiths and J. A. De Haseth, *Fourier Transform Infrared Spectrometry* (John Wiley & Sons, Inc., Hoboken, N.J., 2007).

[145] M. Thiel, M. S. Rill, G. von Freymann, and Martin Wegener, *Three-Dimensional Bi-chiral Photonic Crystals*, Adv. Mat. **21** (46), 4680 (2009).

[146] M. Thiel, H. Fischer, G. von Freymann, and M. Wegener, *Three-dimensional chiral photonic superlattices*, Opt. Lett. **35** (2), 166 (2010).

[147] M. Decker, R. Zhao, C. M. Soukoulis, S. Linden, and M. Wegener, *Twisted split-ring-resonator photonic metamaterial with huge optical activity*, Opt. Lett. **35** (10), 1593 (2010).

[148] S. G. Johnson and J. D. Joannopoulos, *Block-iterative frequency-domain methods for Maxwell's equations in a planewave basis*, Opt. Express **8** (3), 173 (2001).

[149] Z. Bai, J. W. Demmel, J. J. Dongarra, A. Ruhe, and H. A. Van der Vorst, *Templates for the Solution of Algebraic Eigenvalue Problems: A Practical Guide* (Society for Industrial Mathematics, Philadelphia, 2000).

[150] L. Li, *Formulation and comparison of two recursive matrix algorithms for modeling layered diffraction gratings*, J. Opt. Soc. Am. A **13** (5), 1024 (1996).

[151] D. M. Whittaker and I. S. Culshaw, *Scattering-matrix treatment of patterned multilayer photonic structures*, Phys. Rev. B **60** (4), 2610 (1999).

[152] S. G. Tikhodeev, A. L. Yablonskii, E. A. Muljarov, N. A. Gippius, and T. Ishihara, *Quasiguided modes and optical properties of photonic crystal slabs*, Phys. Rev. B **66** (4), 045102 (2002).

[153] J. B. Pendry and A. MacKinnon, *Calculation of photon dispersion relations*, Phys. Rev. Lett. **69** (19), 2772 (1992).

[154] D. Y. K. Ko and J. C. Inkson, *Matrix method for tunneling in heterostructures: Resonant tunneling in multilayer systems*, Phys. Rev. B **38** (14), 9945 (1988).

[155] L. Li and C. W. Haggans, *Convergence of the coupled-wave method for metallic lamellar diffraction gratings*, J. Opt. Soc. Am. A **10** (6), 1184 (1993).

[156] G. Granet and B. Guizal, *Efficient implementation of the coupled-wave method for metallic lamellar gratings in TM polarization*, J. Opt. Soc. Am. A **13** (5), 1019 (1996).

[157] P. Lalanne and G. M. Morris, *Highly improved convergence of the coupled-wave method for TM polarization*, J. Opt. Soc. Am. A **13** (4), 779 (1996).

[158] L. Li, *Use of Fourier Series in the analysis of discontinuous periodic structures*, J. Opt. Soc. Am. A **13** (9), 1870 (1996).

[159] L. Li, *New formulation of the Fourier modal method for crossed surface-relief gratings*, J. Opt. Soc. Am. A **14** (10), 2758 (1997).

[160] K. K. Seet, S. Juodkazis, V. Jarutis, and H. Misawa, *Feature-size reduction of photopolymerized structures by femtosecond optical curing of SU-8*, Appl. Phys. Lett. **89** (2), 024106 (2006).

[161] C. Becker, S. Linden, G. von Freymann, M. Wegener, N. Tétreault, E. Vekris, V. Kitaev, and G. A. Ozin, *Two-color pump–probe experiments on silicon inverse opals*, Appl. Phys. Lett. **87** (9), 091111 (2005).

[162] M. Thiel, J. Fischer, G. von Freymann, and M. Wegener, *Direct laser writing of three-dimensional submicron structures using a continuous-wave laser at 532 nm*, Appl. Phys. Lett. **97** (22), 221102 (2010).

[163] J. Fischer, G. von Freymann, and M. Wegener, *The Materials Challenge in Diffraction-Unlimited Direct-Laser-Writing Optical Lithography*, Adv. Mat. **22** (32), 3578 (2010).

[164] M. Ritala, M. Leskelä, L. Niinistö, and P. Haussalo, *Titanium Isopropoxide as a Precursor in Atomic Layer Epitaxy of Titanium Dioxide Thin Films*, Chem. Mater. **5** (8), 1174 (1993).

[165] V. Lousse, J. Shin, and S. Fan, *Conditions for designing single-mode air-core waveguides in three-dimensional photonic crystals*, Appl. Phys. Lett. **89** (16), 161103 (2006).

[166] H. Benisty, D. Labilloy, C. Weisbuch, C. J. M. Smith, T. F. Krauss, D. Cassagne, A. Béraud, and C. Jouanin, *Radiation losses of waveguide-based two-dimensional photonic crystals: Positive role of the substrate*, Appl. Phys. Lett. **76** (5), 532 (2000).

[167] *http://www.linearcollider.org/about/What-is-the-ILC/Facts-and-figures* (ILC Website).

[168] *http://www.desy.de/* (DESY, Hamburg, Photo Archive).

[169] W. P. Leemans, B. Nagler, A. J. Gonsalves, Cs. Tóth, K. Nakamura, C. G. R. Geddes, E. Esarey, C. B. Schroeder, and S. M. Hooker, *GeV electron beams from a centimetre-scale accelerator*, Nat. Phys. **2** (10), 696 (2006).

[170] X. E. Lin, *Photonic band gap fiber accelerator*, Phys. Rev. Spec. Top. Accel Beams **4** (5), 051301 (2001).

[171] T. Plettner, P. P. Lu, and R. L. Byer, *Proposed few-optical cycle laser-driven particle accelerator structure*, Phys. Rev. Spec. Top. Accel Beams **9** (11), 111301 (2006).

[172] B. M. Cowan, *Two-dimensional photonic crystal accelerator structures*, Phys. Rev. Spec. Top. Accel Beams **6** (10), 101301 (2003).

[173] Y. C. N. Na, R. H. Siemann, and R. L. Byer, *Energy efficiency of an intracavity coupled, laser-driven linear accelerator pumped by an external laser*, Phys. Rev. Spec. Top. Accel Beams **8** (3), 031301 (2005).

[174] J. D. Lawson, *Lasers and Accelerators*, IEEE Trans. Nucl. Sci. **NS-2** (3), 4217 (1979).

[175] C. M. S. Sears, E. Colby, R. Ischebeck, C. McGuinness, J. Nelson, R. Noble, R. H. Siemann, J. Spencer, D. Walz, T. Plettner, and R. L. Byer, *Production and characterization of attosecond electron bunch trains*, Phys. Rev. Spec. Top. Accel Beams **11** (6), 061301 (2008).

[176] B. Cowan, *Three-Dimensional Photonic Crystal Laser-Driven Accelerator Structures*, in *AIP Conf. Proc.*, volume 877 (2006).

[177] R. H. Siemann, *Energy efficiency of laser driven, structure based accelerators*, Phys. Rev. Spec. Top. Accel Beams **7** (6), 061303 (2004).

[178] B. M. Cowan, M.-C. Lin, B. T. Schwartz, E. R. Colby, R. J. England, R. J. Noble, J. E. Spencer, R. L. Byer, and C. M. McGuinness, *Compact couplers for photonic crystal laser-driven accelerator structures*, in *Proceedings of IPAC'10, Kyoto, Japan* (2010).

[179] C. D. Barnes, E. R. Colby, B. M. Cowan, R. J. Noble, D. T. Palmer, R. H. Siemann, J. E. Spencer, D. R. Walz, R. L. Byer, and T. Plettner, *Proposal E-163*, SLAC (2001).

[180] C. McGuinness, E. Colby, and R. L. Byer, *Accelerating electrons with lasers and photonic crystals*, J. Mod. Opt. **56** (18), 2142 (2009).

[181] S. Noda, *Recent Progresses and Future Prospects of Two- and Three-Dimensional Photonic Crystals*, J. Lightwave Technol. **24** (12), 4554 (2006).

[182] B. Cowan, *Optical Damage Threshold of Silicon for Ultrafast Infrared Pulses*, in *AIP Conf. Proc.*, volume 877 (2006).

[183] C. McGuinness (SLAC National Accelerator Laboratory), *private communication*.

[184] G. Winterling, *Amorphes Silizium (a-Si)*, Physik in unserer Zeit **16** (2), 50 (1985).

Acknowledgements

At this point it is my great pleasure to express my gratitude towards all the people who have contributed to the success of this thesis and supported me during the last three years.

First of all I want to thank Prof. Dr. Martin Wegener for giving me the opportunity to work in his group on the fascinating topic of functional elements in three-dimensional photonic bandgap materials. This work has highly benefited from his profound knowledge in the field of optics and photonics and from numerous stimulating discussions. Furthermore, the working conditions regarding experimental facilities and laboratory equipment leave nothing to be desired. Finally, I am grateful for having received the opportunity to present my results on several international conferences.

I would like to thank Prof. Dr. Kurt Busch, both for kindly agreeing to co-referee this thesis, as well as for the support he and his co-workers Sabine Essig and Christian Wolff granted me regarding the theoretical description of the experimentally fabricated structures. In particular, I am grateful to Sabine Essig for the continuous efforts she spent on performing scattering-matrix calculations of woodpile structures with and without embedded functional elements.

Next, my thanks goes to Prof. Dr. Georg von Freymann, not only for helping me to resolve all kinds of technical problems, especially when setting up the INT direct laser writing system, but also for mentoring and supporting me in many questions during my time as a PhD student.

Furthermore, I thank all the members of the Wegener group for the excellent team spirit and the creative atmosphere. In particular, my thanks goes to Dr. Michael Thiel for taking over the direct laser writing process during the INT laboratory relocation period and to Martin Hermatschweiler for setting up well-functioning ALD and CVD systems and passing them on to me. Moreover, I am indebted to Prof. Dr. Stefan Linden and Dr. Manuel Decker for fruitful discussions and to Joachim Fischer, Andreas Frölich, Justyna Gansel, Martin Husnik, Dr. Alexandra Ledermann, Nina Meinzer, Dr. Michael Rill, and Thomas Striebel for pleasant collaboration.

Next, I would like to thank Christopher McGuinness for initiating the photonic crystal particle accelerator project. I really enjoyed working on this exciting and new topic, which merges two fascinating fields in one small and astonishing device.

I would also like to thank Prof. Dr. Frank Peiris for the skillful ellipsometry measurements on silicon thin-films.

The work on 3D photonic nanostructures would not be possible without the opportunity to “have a look”, or even, “to have a look inside”. Therefore I want to thank Jacques Hawecker for brilliant scanning electron microscope images and Patrice Brenner as well as Dr. Erich Müller for their great job operating the focused ion beam system.

Moreover, I would like to thank those people within the Institute of Applied Physics and the Institute of Nanotechnology, who take care of a smooth flow of all administrative and technical processes. Renate Helfen, Christa Weisenburger (retd.), Gisela Habitzreither, Monika Brenkmann, and Erika Schütze have been a permanent and friendly support regarding all kinds of administrative issues. Likewise, my thanks goes to the group’s technicians Thorsten Kuhn (†) and Johann Westhauser, as well as to Heinz Hoffmann, Helmut Lay, and Werner Gilde from the electronics workshop, and to the members of the mechanics workshop for their reliable support. In addition, I thank the Karlsruhe School of Optics & Photonics (KSOP) and the DFG-Center for Functional Nanostructures (CFN) for their continuous support during my thesis and for the opportunity to enrich my PhD education by additional trainings.

A special “Thank you” goes to all critical readers of the manuscript, or parts of it, in particular to Dr. Manuel Decker, Prof. Dr. Georg von Freymann, Nina Meinzer, Christian Wolff, Christopher McGuinness, and Sabine Essig.

Last but not least, I want to thank my family, especially my parents, as well as my friends for their encouragement and continuous interest in my progress. My last huge “Thank you” goes to Dr. Manuel Decker for his enduring support and encouragement.